Virus-Enabled Synthesis and 2D/3D Assembly of Nanowire Networks

By Forrest W. Liau

B.S. Materials Science & Engineering
Massachusetts Institute of Technology, 2006

SUBMITTED TO THE DEPARTMENT OF
MATERIALS SCIENCE AND ENGINEERING
IN PARTIAL FULFILLMENT OF THE REQUIREMENTS FOR THE DEGREE OF

DOCTOR OF PHILOSOPHY

AT THE
MASSACHUSETTS INSTITUTE OF TECHNOLOGY

June 2013

Signature of Author _____
Department of Materials Science and Engineering
April 29, 2013

Certified by _____
Angela M. Belcher
W. M. Keck Professor of Energy in Materials Science & Engineering and Biological Engineering, Thesis Supervisor

Accepted by _____
Gerbrand Ceder
Chair, Departmental Committee on Graduate Students

Thesis Committee Members:

Prof. Yang Shao-Horn
Gail E. Kendall Associate Professor of Mechanical Engineering and Associate Professor of Materials Science and Engineering

Prof. Paula Hammond
David H. Koch Professor of Engineering in Chemical Engineering

Acknowledgments

I would like to thank Professor Angela Belcher for her mentorship and support during tough times. Her commitment to public educational outreach will forever inspire me to seek opportunities to encourage future generations of students to pursue or otherwise support science. Thanks also to my thesis committee members, Professor Paula Hammond and Professor Yang Shao-Horn, for graciously donating their time to meet with me to review this thesis as well as the accompanying thesis presentations.

Many thanks to my fellow Belcherites (lab members), especially Dr. John Burpo and Dr. Ki Tae Nam, for tirelessly driving our projects forward despite setbacks and providing opportunities for me to make significant contributions. Thank you, Department of Materials Science & Engineering (especially Angelita Mireles) and Microsystems Technology Laboratories (especially Kurt Broderick), for being supportive and lovely to work with. Finally, I would like to thank my wife Debbie and my family—Hermann, Marietta, and Winnie Liau—for always being there for me. I love you all very much.

Funding sources for research in this thesis may have included:

Eni S.p.A and MIT Energy Initiative

Institute for Soldier Nanotechnologies

U.S. Army Research Laboratory

Institute of Collaborative Biotechnologies

David and Lucille Packard Foundation.

National Science Foundation

Author's Note

This thesis describes a small selection of experiments from a wide range of highly interdisciplinary and collaborative research projects I pursued with others. The chapters were chosen to create a coherent narrative and represent a collection of success stories using the virus toolkit. Projects not incorporated in this thesis (but deserving mention) include virus microcapacitors with Dr. Ki Tae Nam, electrospun solar cell with Dr. Jung Ah Lee, virus nanowire weighing with Mr. David Gray, virus electrochromic device with Dr. Dong Soo Yun, anatase binding virus with Dr. Soo-Kwan Lee, oxide-coated gold virus nanowires with Dr. Youjin Lee, virus photocatalytic film with Dr. Yoon Sung Nam, and virus 3D microbattery and back-contact virus solar cell with Dr. John Burpo.

My purpose as a doctoral student was to learn as much as I could about nanomaterials fabrication and device integration while also furthering my lab group's research capabilities and helping my collaborators achieve their personal objectives. Perhaps the most rewarding aspect of my doctoral journey was helping fellow lab members meet their publication and graduation deadlines to move on to their next stage in life. I am happy that my experience in microfabrication, virus amplification, nanowire synthesis, microscopy, component sourcing, materials processing, prototyping, and writing have been useful for others. Likewise, I am highly appreciative of the selfless support I received from the MIT community in my own academic journey.

Post-graduation, I am pursuing advanced manufacturing to quickly scale-up new technologies for the high-end consumer electronics industry, which demands both high quality and very large production volumes. Future readers are invited to contact me for questions about technology commercialization and rapid scale-up.

Virus-Enabled Synthesis and 2D/3D Assembly of Nanowire Networks

By Forrest W. Liau

Submitted to the Department of Materials Science and Engineering on April 29, 2013 in Partial Fulfillment of the Requirements for the Degree of Doctor of Philosophy

Abstract

Dense networks of high aspect ratio nanowires can provide important functionality to electronic devices through a unique combination of electronic and structural properties including high conductivity, high surface area, and tunable porosity. In this thesis, we explore the virus-enabled synthesis and two/three-dimensional assembly of metallic and semiconducting nanowire networks for future applications including batteries and solar cells. In Chapter 2, we describe the virus-enabled synthesis of titanium oxide nanowires and their incorporation in layer-by-layer polyelectrolyte assemblies for use in dye sensitized solar cells. In Chapter 3, we describe a two-dimensional network of virus-templated cobalt oxide nanowires integrated into ultrathin microbatteries via soft lithography. In Chapter 4, we describe a three-dimensional porous virus-only aerogel network and demonstrate a virus-assembled metal nanowire network for use in batteries. Finally, in Chapter 5, the mechanical properties of various virus assembled three-dimensional structures are measured and compared. We hereby expand the virus assembly toolkit and demonstrate the versatility of bioengineered materials templates.

Thesis Supervisor: Angela M. Belcher
Title: W.M. Keck Professor of Energy in Materials Science & Engineering and Biological Engineering

TABLE OF CONTENTS

TABLE OF FIGURES

LIST OF ACRONYMS AND ABBREVIATIONS

2D = two dimensional

3D = three dimensional

AM0 = Air mass coefficient zero, simulating solar spectrum outside earth's atmosphere

AM1.5 = Air mass coefficient 1.4, simulating solar spectrum on earth at 48.2º incidence

ASTM = American Society for Testing and Masterials (standard)

CAS = Chemical Abstracts Service (chemical identification)

CNT = carbon nanotube

CuNW = copper nanowire

DMAB = dimethylamino borane

DNA = deoxyribonucleic acid

DNISP = diamond nanoindentation single probe

DSPH = M13 virus with p8 modification DSPHTELP for binding single wall CNTs

DSSC = dye sensitized solar cell

E3 = M13 virus displaying triglumatic acid (-EEE) on n-terminus of p8 protein

EDA = ethylenediamine

EDTA = ethylenediaminetetraacetic acid

EDX = energy dispersive x-ray

EGDMA = ethylene glycol dimethacrylate

ELD = electroless deposition

ER2738 = *e.coli* strain for phage (virus) display

FF = fill factor

FIB = focused ion beam

I_{sc} = short circuit current

JKR = Johnson-Kendall-Roberts model

LB = lysogeny broth

LbL = layer-by-layer polyelectrolyte multilayer assembly

LPD = liquid phase deposition

LPEI = linear poly(ethyleneimine)

MOPS = 3-(N-morpholino)propanesulfonic acid

NP = nanoparticle

NW = nanowire

O-P = Oliver-Pharr model

PAA = polyacrylic acid

PBS = phosphate buffered saline

PDMS = polydimethysiloxane

PEG = polyethylene glycol

PET = polyethylene terephthalate

PHEMA = polyhydroxyethylmethacrylate

pVIII = main coat protein of M13 virus

PVP = polyvinylpyrrolidone

RCA = Radio Corporation of America (wafer cleaning standard)

RF = radio frequency

SEM = scanning electron microscopy

SWCNT = single walled carbon nanotube

TBS = tris-buffered saline

TCO = transparent conducting oxide

TEM = transmission electron microscopy

UV = ultraviolet

UV/VIS = ultraviolet and visible spectrum

V_{oc} = open circuit voltage

XRD = x-ray diffraction

Y21M = virus with main coat protein mutation for increased persistence length

Chapter 1: Introduction

1. Introduction

1.1. Motivation & Background

Nature demonstrates the astonishing possibilities of biological self-assembly for creating intricate functional systems at room temperature in aqueous solution. As nanoscale materials become increasingly important for emerging technological applications, there is much incentive for us to look towards nature for inspiration.[1 2 3 4]

Already, biomolecules have been used to nucleate technologically important inorganic materials, such as semiconductor materials, magnetic materials, and metals.[5 6 7 8] More complex biological entities, including genetically engineered viruses and yeasts, have also been employed to nucleate and arrange quantum dots,[9] nucleate nanowires,[10 11] and form multidimensional liquid crystals and films.[12 13 14]

Expanding this biological toolkit will facilitate innovations in nanobiotechnology for a wide range of applications such as in computing, medicine, and energy. In this thesis, we investigate the use of engineered viruses to enable the fabrication of dense, spatially-constrained nanowire networks. These unique engineered microstructures are integrated into small batteries and solar cells to guide future development and inform suitable applications.

1.2. Engineered Bacteriophage

The M13 filamentous bacteriophage (genus *Inovirus*) contains a circular single-stranded DNA genome encased in a long, cylindrical, and flexible protein capsid.[15] This virus specifically infects *Escherichia coli* bacteria by attaching to the tip of the F conjugative pilus. After infection, the viral DNA is replicated by a mixture of both virus-

encoded and bacterial components, which results in a newly synthesized, single-stranded DNA bound to copies of virus-encoded DNA-binding protein. Concurrently, viral capsid proteins are synthesized and integrated into the bacteria membrane. During virus assembly, the new viral DNA is extruded through assembly sites of the bacteria membrane, at which the DNA-binding proteins are removed and the capsid proteins in the membrane are packaged in a helical, five-fold symmetry around the viral DNA. The resulting structure is approximately 7nm wide and 1μm long in unaltered wild-type form.

The M13 virus can serve as a genetically programmable universal template for the synthesis and assembly of materials. It is highly useful for its genetically modifiable major (gP8) and minor (gP3, gP6, gP7, gP9) coat proteins (Figure 1.1). M13 libraries have been used extensively for biomolecules selection in biotechnology and the M13 viruses have well established genetic modification protocols, and have had much of its structure[16] and biophysics revealed[17 18].

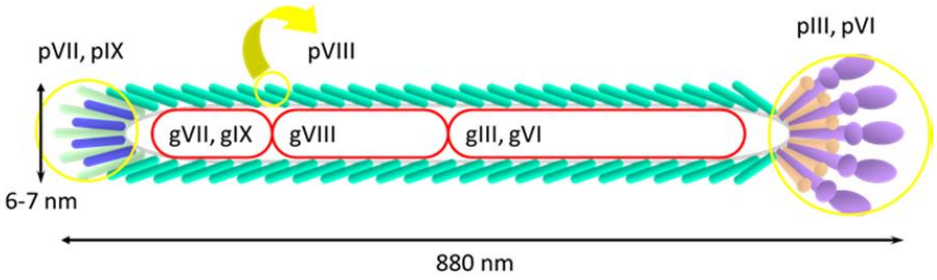

Figure 1.1. M13 virus representation with circular single-stranded DNA shown in red, surrounded by coat proteins gP7 and gP9 at the head, gP8 on the main body, and gP3 and gP6 at the tail. Note: This graphical representation is not to scale, as the filamentous M13 virus has a very high aspect ratio (well over 100:1).

By fusing peptide inserts into appropriate regions, the M13 virus can be engineered to nucleate materials and self-organize into useful structures. The capsid comprises approximately 2,700 copies of gP8 protein.[15] The functionality of these

proteins can be modified through additions in the viral genome. As such, genetic modification has been used to produce virus-based templates for synthesizing and arranging nanomaterials.[19] For example, nanorings have been made by genetically modifying the ends of a virus to bind to a linker molecule,[20] and nanowires[10 21] have been assembled into liquid crystal films.[9 22]

This thesis refers to the E3 clone of the M13 virus for all chapters unless otherwise specified (some sections also use the #9, Y21M, and DSPH clones). The E3 clone, produced through genetic modification and expression using a phagemid system, contains gP8 coat proteins with tri-glutamate (EEE-) peptides fused to the N termini. Tri-glutamate (EEE-) was fused to the N terminus of each copy of the major coat p8 protein with 100% expression. The E3 clone was chosen because it had been successfully used with charged polymers in electrostatic multilayer thin film assembly.[23 24]

This kind of templated materials production may lead to high performance electronic components in smaller, more flexible packaging. Furthermore, the knowledge derived from working with the M13 virus could be applied to other types of biological entities in the future to create an even greater variety of products. Further details about the M13 virus and the recommended amplification protocol can be found in the Appendix.

1.3. Relationship with Prior and Concurrent Work

An overview of virus assembly and energy related research at MIT by Dr. Angela Belcher's Biomolecular Materials Group (belcher10.mit.edu) is shown in Figure 1.2. Time flows from top to bottom in the figure, and related achievements are visually

grouped by common topic or technique used. Bolded names indicate research efforts described in this thesis.

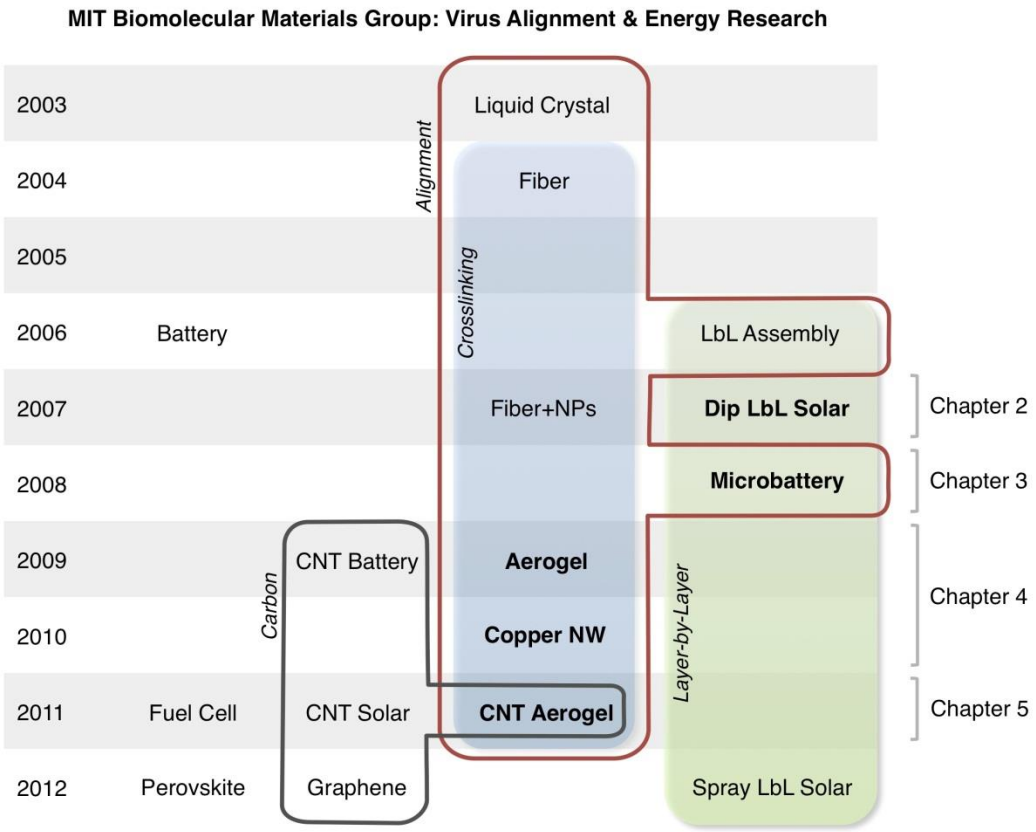

Figure 1.2. Overview of virus assembly and energy devices research by the MIT Biomolecular Materials Group. Research topics described in this thesis are denoted in bolded text. LbL = layer-by-layer assembly. NP = nanoparticle. CNT = carbon nanotube. Projects with common themes (carbon-based nanomaterials, virus alignment, crosslinking, and layer-by-layer assembly) are grouped by bubbles and colored backgrounds.

Viral peptide binding to electronic materials was first demonstrated in the lab in 2000,[25] followed by virus-enabled nanoparticle arrangement in 2002.[9] The first successful attempt to create dimensionally-constrained virus assemblies was published in 2003,[26] showing the liquid crystal-like self-organization of dense virus solutions. In 2004, viruses were aligned by electrospinning and crosslinked for the first time by glutaraldehyde.[27] In

2006, viruses were first incorporated into polyelectrolyte multilayer stacks by layer-by-layer (LbL) assembly.[28] The first battery using virus-templated nanowires was also demonstrated in 2006.[24]

This thesis begins its narrative in 2007, describing the first dye sensitized solar cell (DSSC) fabricated from virus LbL in Chapter 2. The virus LbL combination is further employed in Chapter 3 for the first microbattery fabricated from virus-templated nanowires, demonstrated in 2008.[17] Chapter 4 shows the first virus-only aerogel and virus-templated metal nanowire aerogel created in 2009 using an adaptation of the glutaraldehyde crosslinking technique from the virus fiber studies. The bulk mechanical properties of crosslinked virus hydrogels, virus nanowire aerogels, and the first virus-templated carbon nanotube (CNT) aerogel are discussed in Chapter 5, as measured in 2011.

Other important virus-assembly and energy related developments in the lab, which are not covered in this thesis, include the first demonstration of electronic material ordering on crosslinked electrospun virus bundles in 2007,[29] the first virus-CNT battery in 2009,[30] the first virus-CNT dye sensitized solar cell[31] and first virus-templated electrocatalytic nanowires for fuel cells[32] in 2011, the first virus-templated perovskite photocatalytic nanowires[33] and first virus-stabilized graphene complex for batteries[34] in 2012, and the first spray-assisted virus LbL dye sensitized solar cell published in 2013.[35] We anticipate exciting further developments with the M13 virus toolkit as new talent in the lab continue to push the boundaries of the biotemplate approach and creatively combine new techniques in emerging interdisciplinary applications.

1.4. References

[1] Mann, S. (1996). *Biomimetic Materials Chemistry*. VCH Press.

[2] Ball, P. (2001). It all falls into place... *Nature*, *413*(6857), 667-668.

[3] Flynn, C. E., Lee, S. W., Peelle, B. R., & Belcher, A. M. (2003). Viruses as vehicles for growth, organization and assembly of materials. *Acta Materialia*, *51*(19), 5867-5880.

[4] Niemeyer, C. M. (2001). Nanoparticles, proteins, and nucleic acids: biotechnology meets materials science. *Angewandte Chemie International Edition*, *40*(22), 4128-4158.

[5] Brown, S. (1997). Metal-recognition by repeating polypeptides. *Nature biotechnology*, *15*(3), 269-272.

[6] Whaley, S. R., English, D. S., Hu, E. L., Barbara, P. F., & Belcher, A. M. (2000). Selection of peptides with semiconductor binding specificity for directed nanocrystal assembly. *Nature*, *405*(6787), 665-668.

[7] Mann, S., Shenton, W., Li, M., Connolly, S., & Fitzmaurice, D. (1999). Biologically programmed nanoparticle assembly. *Advanced Materials*, *12*(2), 147-150.

[8] Nygaard, S., Wendelbo, R., & Brown, S. (2002). Surface-Specific Zeolite-Binding Proteins. *Advanced Materials*, *14*(24), 1853-1856.

[9] Lee, S. W., Mao, C., Flynn, C. E., & Belcher, A. M. (2002). Ordering of quantum dots using genetically engineered viruses. *Science*, *296*(5569), 892-895.

[10] Mao, C., Flynn, C. E., Hayhurst, A., Sweeney, R., Qi, J., Georgiou, G., ... & Belcher, A. M. (2003). Viral assembly of oriented quantum dot nanowires. *Proceedings of the National Academy of Sciences*, *100*(12), 6946-6951.

[11] Flynn, C. E., Lee, S. W., Peelle, B. R., & Belcher, A. M. (2003). Viruses as vehicles for growth, organization and assembly of materials. *Acta Materialia*,*51*(19), 5867-5880.

[12] Lee, S. W., Wood, B. M., & Belcher, A. M. (2003). Chiral smectic C structures of virus-based films. *Langmuir*, *19*(5), 1592-1598.

[13] Lee, S. W., Lee, S. K., & Belcher, A. M. (2003). Virus-Based Alignment of Inorganic, Organic, and Biological Nanosized Materials. *Advanced Materials*,*15*(9), 689-692.

[14] Dujardin, E., Peet, C., Stubbs, G., Culver, J. N., & Mann, S. (2003). Organization of metallic nanoparticles using tobacco mosaic virus templates.*Nano Letters*, *3*(3), 413-417.

[15] Barbas III, C. F., Barbas, C. F., Burton, D. R., Scott, J. K., & Silverman, G. J. (2004). *Phage display*. CSHL Press.

[16] Marvin, D. A., Welsh, L. C., Symmons, M. F., Scott, W. R. P., & Straus, S. K. (2006). Molecular structure of fd (f1, M13) filamentous bacteriophage refined with respect to X-ray fibre diffraction and solid-state NMR data supports specific models of phage assembly at the bacterial membrane. *Journal of molecular biology*, *355*(2), 294-309.

[17] Nam, K. T., Wartena, R., Yoo, P. J., Liau, F. W., Lee, Y. J., Chiang, Y. M., ... & Belcher, A. M. (2008). Stamped microbattery electrodes based on self-assembled M13 viruses. *Proceedings of the National Academy of Sciences*,*105*(45), 17227-17231.

[18] Dogic, Z., & Fraden, S. (2006). Ordered phases of filamentous viruses. *Current opinion in colloid & interface science*, *11*(1), 47-55.

[19] Huang, Y., Chiang, C. Y., Lee, S. K., Gao, Y., Hu, E. L., De Yoreo, J., & Belcher, A. M. (2005). Programmable assembly of nanoarchitectures using genetically engineered viruses. *Nano letters*, *5*(7), 1429-1434.

[20] Nam, K. T., Peelle, B. R., Lee, S. W., & Belcher, A. M. (2004). Genetically driven assembly of nanorings based on the M13 virus. *Nano letters*, *4*(1), 23-27.

[21] Mao, C., Solis, D. J., Reiss, B. D., Kottmann, S. T., Sweeney, R. Y., Hayhurst, A., ... & Belcher, A. M. (2004). Virus-based toolkit for the directed synthesis of magnetic and semiconducting nanowires. *Science*, *303*(5655), 213-217.

[22] Dogic, Z., & Fraden, S. (1997). Smectic phase in a colloidal suspension of semiflexible virus particles. *Physical review letters*, *78*(12), 2417-2420.

[23] Yoo, P. J., Nam, K. T., Qi, J., Lee, S. K., Park, J., Belcher, A. M., & Hammond, P. T. (2006). Spontaneous assembly of viruses on multilayered polymer surfaces. *Nature materials*, *5*(3), 234-240.

[24] Nam, K. T., Kim, D. W., Yoo, P. J., Chiang, C. Y., Meethong, N., Hammond, P. T., ... & Belcher, A. M. (2006). Virus-enabled synthesis and assembly of nanowires for lithium ion battery electrodes. *science*, *312*(5775), 885-888.

[25] Whaley, S. R., English, D. S., Hu, E. L., Barbara, P. F., & Belcher, A. M. (2000). Selection of peptides with semiconductor binding specificity for directed nanocrystal assembly. *Nature*, *405*(6787), 665-668.

[26] Lee, S. W., Lee, S. K., & Belcher, A. M. (2003). Virus-Based Alignment of Inorganic, Organic, and Biological Nanosized Materials. *Advanced Materials*,*15*(9), 689-692.

[27] Lee, S. W., & Belcher, A. M. (2004). Virus-based fabrication of micro-and nanofibers using electrospinning. *Nano letters*, *4*(3), 387-390.

[28] Yoo, P. J., Nam, K. T., Qi, J., Lee, S. K., Park, J., Belcher, A. M., & Hammond, P. T. (2006). Spontaneous assembly of viruses on multilayered polymer surfaces. *Nature materials*, *5*(3), 234-240.

[29] Chiang, C. Y., Mello, C. M., Gu, J., Silva, E. C., Van Vliet, K. J., & Belcher, A. M. (2007). Weaving genetically engineered functionality into mechanically robust virus fibers. *Advanced Materials*, *19*(6), 826-832.

[30] Lee, Y. J., Yi, H., Kim, W. J., Kang, K., Yun, D. S., Strano, M. S., ... & Belcher, A. M. (2009). Fabricating genetically engineered high-power lithium-ion batteries using multiple virus genes. *Science*, *324*(5930), 1051-1055.

[31] Dang, X., Yi, H., Ham, M. H., Qi, J., Yun, D. S., Ladewski, R., ... & Belcher, A. M. (2011). Virus-templated self-assembled single-walled carbon nanotubes for highly efficient electron collection in photovoltaic devices. *Nature nanotechnology*, *6*(6), 377-384.

[32] Lee, Y., Kim, J., Yun, D. S., Nam, Y. S., Shao-Horn, Y., & Belcher, A. (2012). Virus-templated Au and Au/Pt Core/Shell Nanowires and Their Electrocatalytic Activities for Fuel Cell Applications. *Energy & Environmental Science*.

[33] Nuraje, N., Dang, X., Qi, J., Allen, M. A., Lei, Y., & Belcher, A. M. (2012). Biotemplated Synthesis of Perovskite Nanomaterials for Solar Energy Conversion. *Advanced Materials*.

[34] Oh, D., Dang, X., Yi, H., Allen, M. A., Xu, K., Lee, Y. J., & Belcher, A. M. (2012). Graphene Sheets Stabilized on Genetically Engineered M13 Viral Templates as Conducting Frameworks for Hybrid Energy-Storage Materials.*Small*.

[35] Chen, P. Y., Ladewski, R., Miller, R., Dang, X., Qi, J., Liau, F. W, Belcher, A. M., & Hammond, P. T. (2013). Layer-by-layer assembled porous photoanodes for efficient electron collection in dye-sensitized solar cells. *Journal of Materials Chemistry A*, *6*(1), 2217-2224.

Chapter 2: Metal Oxide 3D Nanowire Network in Dye Sensitized Solar Cell

2. Metal Oxide 3D Nanowire Network in Dye Sensitized Solar Cell

2.1. Introduction

The growing demand for solar power generation has motivated a tremendous amount of research & development towards improving the performance and solar devices and decreasing their cost. A particularly promising type of potentially low-cost solar device, the dye sensitized solar cell (DSSC), was first report by O'Regan and Grätzel in 1991 and has been a popular topic since.[1] The basic theory of operation for a dye sensitized solar cell is shown in Figure 2.1. Photons enter the cell through the transparent conducting glass and reach the dye on the surface of the anode structure. Photons with enough energy to be absorbed by the dye create an excited state in the dye, resulting in an electron being injected into the conduction band of the anode within picoseconds.[2 3] Once inside the anode, the electron diffuses to the transparent TiO_2 current collector. The dye molecule, having lost an electron, strips an electron from the iodide in the electrolyte, oxidizing it into triiodide before the injected electron has a chance to recombine with the oxidized dye molecule. The triiodide then recovers its missing electron at the cathode, where the injected electron re-enters the device after performing work through an external circuit.

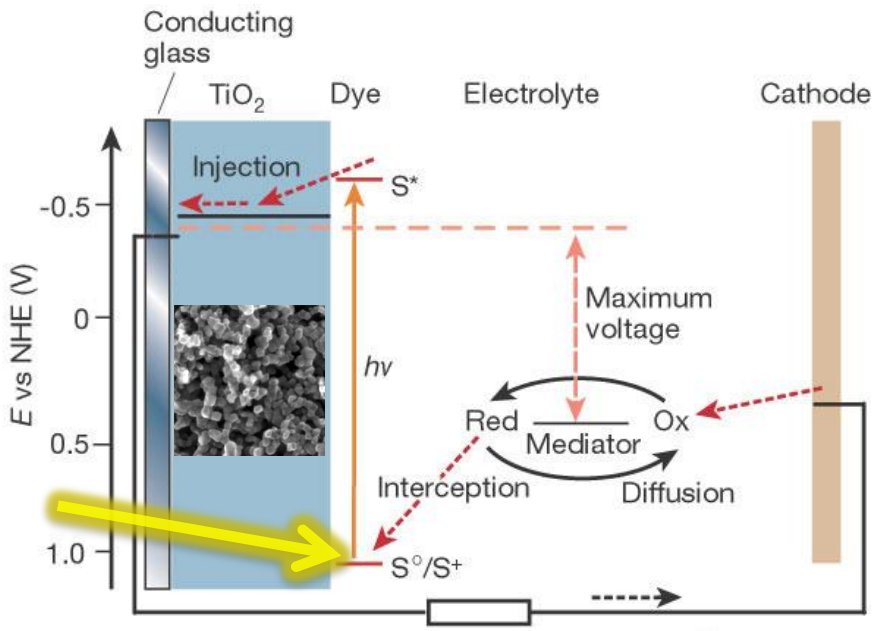

Figure 2.1. Principle of operation for a dye sensitized solar cell (diagram modified from Grätzel publication[3]). When an incident photon (yellow arrow) is absorbed by the dye, a photoexcited electron enters the conduction band of the TiO_2 (scanning electron microscopy image shown) and transported to the anode, passed through a resistive load, and shuttled back by the redox couple to its ground state in the dye. Reprinted with permission from Nature Publishing Group.

DSSCs are a popular emerging solar technology because of their ease of fabrication and relatively high power conversion efficiency in low diffuse light conditions.[4] Without substituting materials, the performance of a conventional DSSC can be increased by improving:

- Quantity of chemisorbed sensitizers per unit volume.
- Photon absorption by sensitizer.
- Electron transfer from dye to anode.
- Electron transport within anode (reduce recapture by electrolyte).
- Electron transfer from anode to anodic current collector.
- Pore filling of anode by electrolyte.
- Transport in electrolyte.

This chapter primarily concerns improving the electron transport and pore-filling by having the photoanode comprise a network of electron transporting nanowire bundles instead of nanoparticles. The nanowires, which are essentially long clusters of well-connected nanoparticles, serve as electron transport paths and enable a high amount of pore filling via large void spaces. Similar strategies have been developed to create oriented nanostructures, such as nanotubes,[5] nanorods,[6] and nanofibers,[7] and process them into photoanodes to form directional electron pathways to improve electron collection. However, while these methods improve the electron collection of DSSCs, complex processes limit their application in mass production.

Layer-by-layer (LbL) assembly is a widely-used thin film deposition method that offers several advantages: It is a simple and cheap process with strong potential for scalability and control over thickness, morphology, and chemical composition of films.[8] [9] [10] In LbL, different charged species including polymeric and biological particles can be deposited on a substrate in sequences of alternating charge or other complementary interactions such as hydrogen bonding.[11] [12] This chapter describes the combination of LbL assembly with virus-templated nanowire synthesis to create high surface area electron transporting anode structures for DSSCs with tunable thickness and porosity.

While previous research on virus and nanowire assemblies has involved dense liquid crystal films of viruses,[13] virus fibers,[14] and virus monolayers,[15] this chapter involves relatively thick films of "fuzzy sponge" networks of virus-templated nanowires. A key difference between the virus LbL structures in this chapter from the ones in Chapter 3 is that the LbL structures described in this chapter encourage the viruses to

form a 3D interdiffused network, whereas the LbL goal in Chapter 3 is to float the viruses to form a thin and compact surface film.

The presence of high aspect ratio viruses within an LbL polymer network enables the formation of interconnected TiO_2 crystallites that increase efficiency through improved electron collection (enhanced diffusion length). A graphical comparison between traditional TiO_2 nanoparticle paste structures and the high aspect ratio virus LbL structures is shown in Figure 2.2. In this Chapter, we demonstrate that the unique microstructure created by the virus LbL approach can produce functional DSSCs. Collaborators in this chapter include Dr. Friederike Fleischhaker and Dr. Rebecca Ladewski.

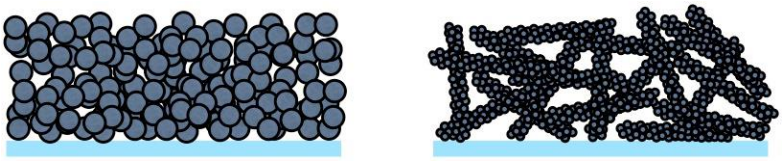

Figure 2.2. Comparison between nanoparticle and nanowires based TiO_2 structures for dye sensitized solar cells. A nanowire photoanode assembly (right) may have better pore filling, electrolyte contact, and electron diffusion compared to a nanoparticle assembly (left).

2.2. Experimental

2.2.1. TiO_2 Deposition Chemistry

Titanium oxide is a technologically important material due to its unique electronic and photoelectrochemical properties. It is a promising material for self-cleaning, photocatalytic surfaces,[16 17] high lifetime batteries,[18] rugged gas sensors,[19] and dye-sensitized solar cells.[20] Virus-enabled synthesis and assembly methods have the potential to improve titanium oxide based devices by producing novel titanium oxide

microstructures and enabling advantageous product form factors, e.g., thin films and fibers.

Deposition of titanium oxide involves reacting titanium as part of a negative ion complex with fluorine ($[TiF_6]^{2-}$). As current virus-enabled methods employ either the molecular recognition of specific crystallographic faces of materials or the negative charge attraction to positive metal ions, a new method for interacting with negative species was necessary. Accordingly, one of our objectives was to find a method to attach negative ions and ion complexes to engineered viruses for greater flexibility in virus-enabled materials synthesis. In particular, we investigated the nucleation of an inorganic material (titanium oxide) through the use of the amine functionality of an engineered virus.

Liquid phase deposition (LPD) is a wet process for depositing metal oxide or hydroxide thin films homogeneously on various types of surfaces.[21] The relatively simple process involves immersing a substrate in an aqueous solution of the reactant, which allows a metal oxide thin film to form through a ligand exchange (hydrolysis) equilibrium reaction. In the reaction, a metal-fluoro complex species reacts with water to produce metal oxide, and a fluorine consumption reaction with boric acid or aluminum metal acting as the fluorine scavenger accelerates the ligand-exchange reaction by shifting the equilibrium reaction to the right-hand side. For example:

$$MF_x^{(x-2n)-} + nH_2O = MO_n + xF^- + 2nH^+$$

$$H_3BO_3 + 4HF = BF_4^- + H_3O^+ + 2H_2O$$

This technique has been used to fabricate various titanium oxide conformal structures, including macroporous films using a colloidal template,[22] and gold-dispersed thin films.[23] To utilize this titanium oxide synthesis technique on an E3 virus template, we needed to activate the virus' amine functionality. The zeta potential (overall surface charge) of the virus changes from negative to positive as the pH of the surrounding solution is lowered to less than approximately 4.3.[24] At or above neutral pH, the virus can serve as a template for nucleating positive ions or ion complexes. Yet, at a low pH, the positive amine functionality can provide sites for preferential nucleation of the $[TiF_6]^{2-}$ negative ion complex for targeted liquid phase deposition.

2.2.2. TiO_2 Growth on Viruses and Virus Networks

Virus-templated titanium oxide nanowires suitable for transmission electron microscopy (TEM) imaging, as shown in Figure 3.3(a) and Figure 3.3(b), were created by first incubating 250µL of 3×10^7 viruses/mL in 5mL of 5mM ammonium hexafluorotitanate ($(NH4)_2TiF_6$) for 30min at pH 2 (adjusted via hydrochloric acid) to allow the $[TiF_6]^{2-}$ ion complexes to attach to the virus' positive amine sites. Subsequently, 5mL of 50mM boric acid (H_3BO_3), also at pH 2, was added to drive the ligand exchange reaction for 10min. The resulting virus-templated TiO_2 nanowires were partially amorphous with anatase crystalline domains scattered throughout, as seen in Figure 2.3(c).

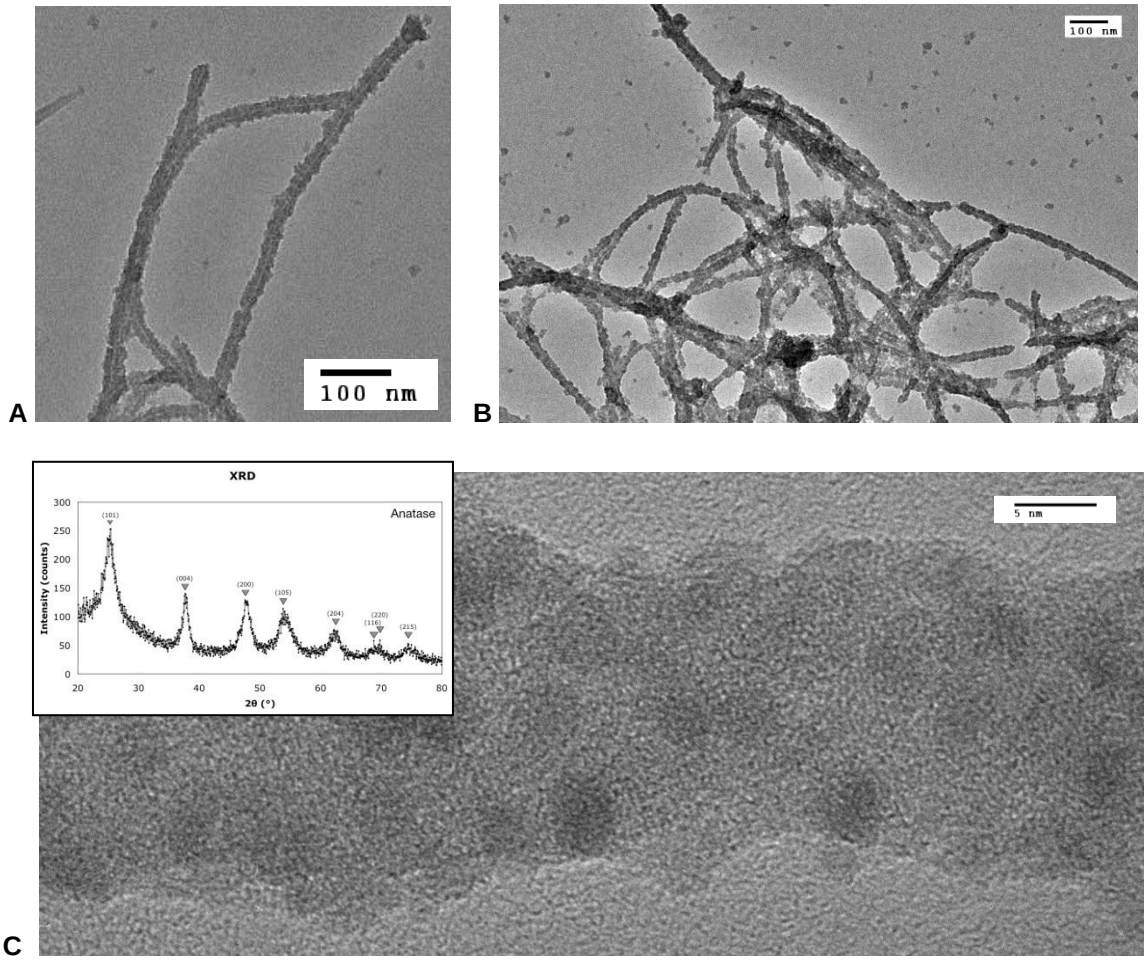

Figure 2.3. Transmission electron microscopy (TEM) images of virus-templated TiO_2 nanowires. A) and B) Virus core is visible through nanowires as light lines. Scale bar is 100nm for both images. C) Small crystalline domains (~3nm diameter) in nanowires are visible via high resolution TEM, and x-ray diffraction (XRD) determined the TiO_2 crystalline domains to be anatase phase. Scale bar is 5nm.

It is important to note that the appropriate concentrations and ratios of virus and reactants do not scale linearly with total reaction volume. Changing the total reaction volume requires new reaction optimization, possibly due to differences in vessel surface area. The quality of nanowires is highly influenced by the precise ratio of viruses and reactants, and the ideal ratio varies with different reaction volumes.

This nanowire synthesis method can be modified to produce different variations of TiO_2 nanowires. For example, sonicating the virus reactant mixture during synthesis

produces nanowires with a rougher, more crystalline morphology as shown in Figure 2.4(a). Additional factors such as solution temperature and reactant ratios and pH can be used to alter the synthesis. Nanoparticles can also be incorporated, as shown in Figure 2.4(b) with 5nm gold nanoparticles attached to a gold-binding virus ("#9" virus clone) prior to liquid phase deposition.

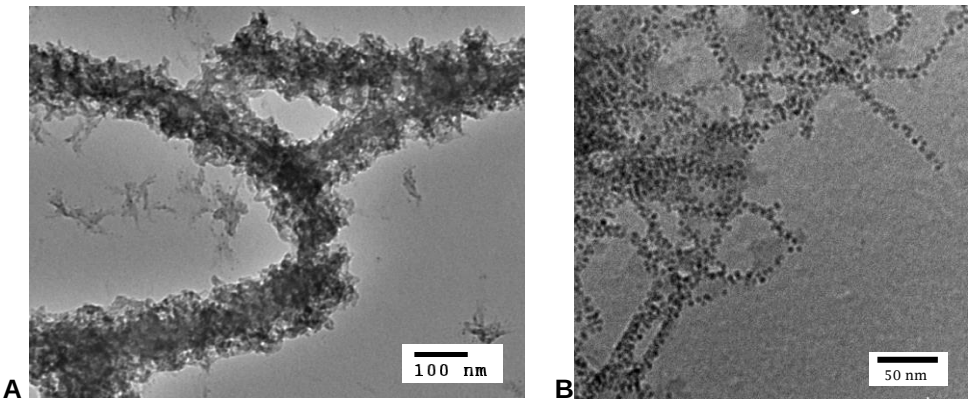

Figure 2.4. Virus-templated TiO_2 nanowires with different morphologies. A) Rough surface texture resulting from sonication during synthesis. B) Hybrid nanowires created by attaching 5nm gold nanoparticles to viruses with engineered gold-binding motif prior to TiO_2 liquid phase deposition. Scale bar is 50nm.

To test virus-assembled nanowire stability as a film, the TiO_2 nanowires were deposited on filter paper via vacuum filtration and then contact-printed onto a glass slide. This printing technique is similar to the one used in Chapter 3, except that filter paper is used as the transferring substrate instead of polydimethylsiloxane. Figure 2.5(a) and Figure 2.5(b) show the resulting nanowire film. The primary limitation of this method is its maximum achievable film thickness (< 3μm) and the resulting lateral orientation preference, as very few viruses would be oriented perpendicularly to the membrane. The filtration process halts when the nanowires begin clogging the membrane due to their relatively short length (~1μm) and high flexibility; therefore the current approach cannot

produce a 10-15μm film typically needed for high efficiency DSSCs. It was possible to stamp multiple films onto one another to increase the overall thickness, but the resulting film delaminated easily.

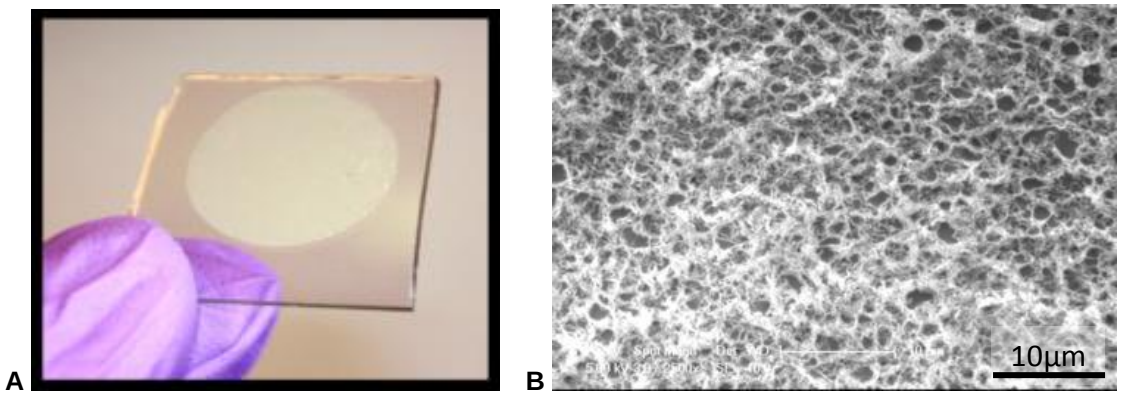

Figure 2.5. Contact printing of virus-templated TiO_2 nanowires. A) Nanowires were captured on filter paper via vacuum filtration and stamped onto a glass slide. B) Scanning electron microscopy image of nanowire film showing nanowire network. Scale bar (white) is 10μm.

Liquid phase deposition with $(NH_4)_2TiF_6$ or titanium chloride ($TiCl_4$) can be used to deposit TiO_2 not only on individual viruses in aqueous solution, but also on crosslinked virus networks, as shown in Figure 3.6. Virus crosslinking via glutaraldehyde is described in detail in Chapter 4. To test virus-assembled nanowire networks in DSSCs, we chose to utilize layer-by-layer assembly (LbL, also used in Chapter 3) instead of crosslinking to have greater flexibility with the thickness and porosity of the resulting TiO_2 films, described in the next section.

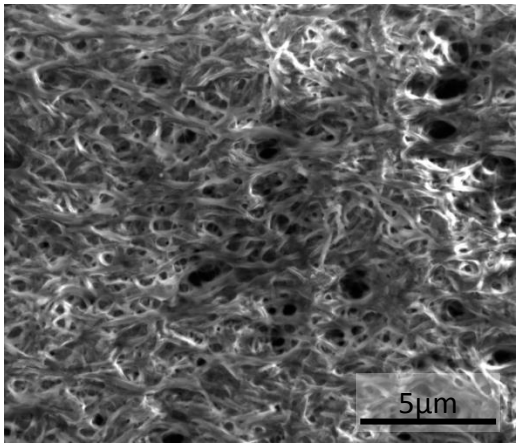

Figure 2.6. TiO_2 grown on virus-assembled crosslinked networks. The degree of rope-like bundling can be controlled through the addition of viruses engineered to be relatively stiff (Y21M virus clone). Scale bar is 5µm.

2.2.3. Virus Dispersion in Polyelectrolyte Multilayers

Negatively charged E3 viruses were embedded in polymer multilayer assemblies comprising the weak polyelectrolytes linear polyethyleneimine (LPEI, positively charged) and polyacrylic acid (PAA, negatively charged) built on a conductive glass substrate. The multilayer assemblies incorporating viruses were converted into a TiO_2 nanowire network by liquid phase deposition. Following the synthesis step, the polymer/protein organic framework was removed by 450ºC calcination, and the resulting TiO_2 nanowire network was immersed in a solution of a sensitizing dye. The complete DSSC was constructed by infiltrating the nanowire network with a viscous electrolyte and attaching a platinum-coated conductive glass counter electrode.

A schematic illustration of the preparation steps is shown in Figure 2.7. We decided to work with tetra-layers of the composition (E3, LPEI, PAA, LPEI) as smallest subunit in the multilayer for the following reason: The amount of incorporated virus (resulting in TiO_2 surface area for sensitizer adsorption) is kept as high as possible while

the structural benefits of the weak polyelectrolyte pair LPEI and PAA are maintained. A transparent conducting oxide (TCO) with TiO_2 separation layer was chosen as the substrate for photovoltaic application.

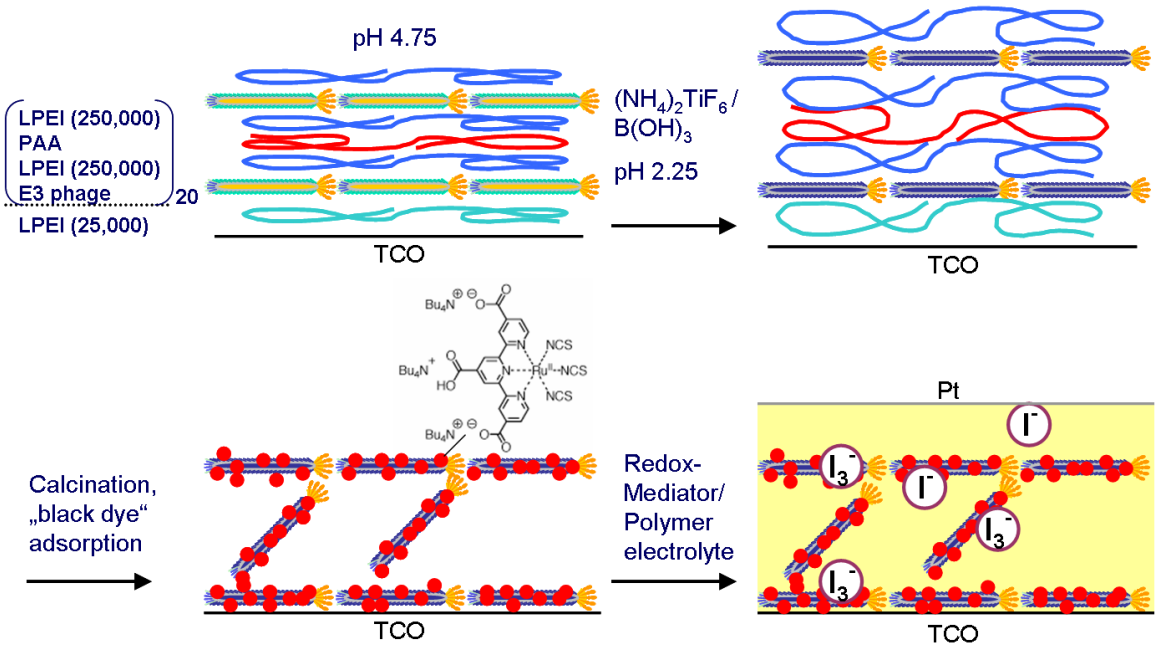

Figure 2.7. Schematic illustration of the preparation of virus/ LbL-templated porous TiO_2 nanowire network solid-state dye sensitized solar cells (DSSCs). Light enters the device via the transparent conducting oxide (TCO) side.

In order to form a patchy bottom-layer facilitating contact between the first bacteriophage layer and the substrate, LPEI (25,000 Mw) was used first and once only in the layering process. We replaced LPEI (25,000 Mw) with LPEI (250,000 Mw) in the following tetra-layers to prevent floating of the bacteriophage to the surface of the multilayer-assembly. LbL assembly conditions were adjusted to pH 4.75 (with immersion and rinsing bathes) to prevent bacteriophage aggregation or repulsion and to provide suitable binding conditions for the weak polyelectrolytes.[25] Note that the LbL assembly scheme in Figure 2.7 is highly simplified: Microscopy images have shown

interpenetrations between single layers of the LbL-multilayer stack[8] and the virus and polymer layers are likely interconnected.

In the next step, the bacteriophage templates within the multilayer were converted to TiO_2 nanowires via liquid phase deposition by immersing the LbL-assembled film into aqueous TiO_2 precursor solutions at pH 2.25. The LbL film was first exposed to $(NH_4)_2TiF_6$ and then an equivalent volume of H_3BO_3 was added. The TiO_2 conversion took place completely within the film in the solid-state, and no further work-up steps were performed. In addition, pH 2.25 conditions introduced nano- and microporosity by electrostatic repulsion into LPEI/PAA LbL-films as previously reported.[26]

The LPEI/PAA polymer framework was then removed by calcination, and the resulting TiO_2 nanowire network is immersed into a solution of the sensitizing dye: Tris(isothiocyanato)-ruthenium(II)-2,2':6',2''-terpyridine-4,4',4''- tricarboxylic acid, tris-tertrabutylammonium salt ("black dye"). Potential carbon residues from the bacteriophage scaffold—coaxially trapped within the TiO_2-nanowires—have the welcome potential side-effect of exhibiting similarities to TiO_2/carbon nanotube coaxial composites. These materials have been shown to possess good photocurrent and photoinduced electron-transfer properties.[27] The complete solid-state DSSC was constructed by infiltrating the nanowire network with the necessary redox-mediator as well as a solid ionically conducting polymer and by applying a platinum-coated TCO counter-electrode. For the infiltration, a formulation consisting of poly(ethylene oxide-co-epychlorohydrin), ethylenecarbonate, propylenecarbonate and NaI, I_2, reported in literature, was used.[28]

Figure 2.8(a) shows the surface of an LbL assembly at different deposition stages to confirm the build-up. Figure 2.8(a:a) shows a corresponding assembly with viruses as the top layer, and Figure 2.8(a:b) depicts the surface again after deposition of a polymer stack on top of the virus layer. Cross-sectional transmission electron microscopy (TEM) images of a free-standing multilayer assembly (embedded in epoxy resin and cut by microtome) after TiO_2 synthesis and calcination are shown in Figure 2.8(b). The sample was cut perpendicular and parallel to the film surface by microtome in Figure 2.8(b:a) and Figure 2.8(b:b), respectively. Both images show a porous structure as well as high-contrast inorganic material. In Figure 2.8(b:a), the contrasted features are predominantly circular, whereas a mesh of longitudinal wire-like features can be seen in Figure 2.8(b:b). These observations suggest the *in situ* formation of an inorganic, anisotropic nanowire network. X-ray diffraction (XRD) measurements performed on a free-standing, pH-treated, TiO_2-converted and calcined (E3, LPEI, PAA, LPEI) stacks confirmed the material to be anatase phase with an average crystal size of 10nm. Further details of the experimental methods can be found in the Appendix.

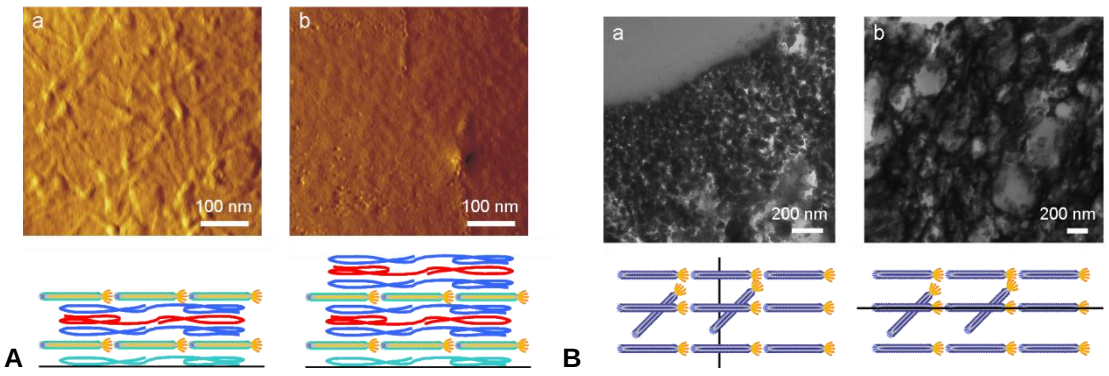

Figure 2.8. Polymer multilayer assemblies incorporating viruses. A) Atomic force microscopy (AFM) images of layer-by-layer virus/polymer assemblies with a) E3 as top layer and b) polymer stack as top layer. B) Transmission electron microscopy (TEM) images of the TiO_2 nanowire network following calcination showing cross-sectional and planar cuts.

2.2.4. Solar Cell Fabrication & Characterization

The resulting virus LbL templated TiO_2 nanowire DSSCs, infiltrated with previously mentioned solid electrolyte[28], were tested under 30mW/cm^2, AM1.5 illumination for simulated current-voltage data. The air mass (AM) 1.5 standard simulates the solar spectrum on earth at 48.2º incidence, e.g., in the morning and afternoon. For comparison, equivalently constructed DSSCs in which the virus LbL TiO_2 nanowire network is replaced by a spin-coated commercially available nanoparticle film are tested under identical conditions. The TiO_2 nanoparticle film thickness of the control samples was adjusted to that of the virus LbL TiO_2-nanowire network (750nm). Note that typical laboratory DSSCs designed for highest efficiency use a high vapor pressure liquid electrolyte and have TiO_2 thicknesses between 10-20μm for complete light capture. A higher efficiency setup was implemented with virus LbL DSSCs in a later study also involving spray-assisted LbL.[29]

To take into account the light scattering effects of the TiO_2 nanowire network, a TiO_2-nanoparticle formulation with mixed-in light scattering particles was chosen (13/400nm TiO_2 particles in Ti-Nanoxide D/SC paste by Solaronix). The average short-circuit current (I_{sc}), the open-circuit voltage (V_{oc}), the maximum output power (P_{max}), conversion efficiency ($\eta = P_{max}/P_{input}$) and the fill factor ($FF = P_{max}/(I_{sc} \cdot V_{oc})$) of the first tested devices are listed in Table 2.1. Representative current-voltage curves of a virus LbL TiO_2 nanowire solid-state DSSC and a TiO_2 nanoparticle solid-state DSSC control (both with 750nm photoanode thickness) are plotted in Figure 2.9.

Table 2.1. Photovoltaic performance of a virus LbL TiO_2 nanowire solid-state DSSC and a TiO_2 nanoparticle solid-state DSSC. TiO_2 anode thickness: 750 nm, P_{input}: 30mW/cm^2.

Dye Sensitized Solar Cell	I_{sc} (mA/cm^2)	V_{oc} (mV)	P_{max} (μW/cm^2)	Efficiency η (%)	FF (%)
Virus LbL Nanowire	2.10	612	704.8	2.35 ± 0.2	55
Nanoparticle	1.87	611	587.9	1.96 ± 0.1	51

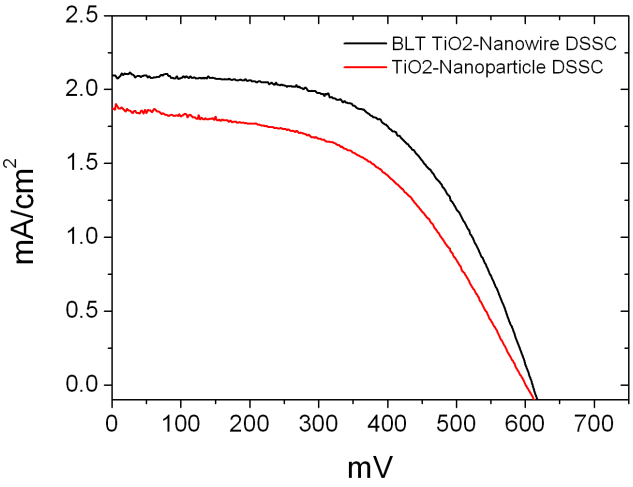

Figure 2.9. Current-voltage curves of a virus LbL TiO_2 nanowire DSSC (labeled BLT) and a TiO_2 nanoparticle DSSC. Both devices have 750nm photoanode thickness and use a solid-state electrolyte. Test data shown in Table 2.1.

The measurements show that the newly developed virus LbL TiO_2 nanowire DSSCs have 20% higher conversion efficiency arising from higher I_{sc} with similar V_{oc} and FF. This relative performance improvement of the virus LbL TiO_2 nanowire DSSCs at comparable TiO_2 film thickness can be attributed to the open, porous network structure that improves the interfacial contact of the solid-state DSSC components. Carbon/TiO_2 coaxial structures may have an additional impact. In addition, absolute conversion efficiencies are expected to significantly increase with increasing TiO_2 electrode thickness—which results in an increased amount of adsorbed sensitizer—up to a maximum efficiency that is limited by the electron diffusion length and photon penetration. If we assume a higher electron diffusion length in the virus LbL TiO_2

nanowire network compared to the TiO_2 nanoparticle control (analogous to comparisons between TiO_2 nanowires synthesized by traditional methods and nanoparticle controls), the relative efficiency improvement of the virus TiO_2 nanowire DSSCs will likely increase even at TiO_2 electrode thicknesses exceeding the efficiency maximum of TiO_2-nanoparticle controls.[30] [31]

2.3. Conclusion

In summary, we have developed a facile method to convert a genetically engineered virus and weak polyelectrolyte LbL assembly into a porous TiO_2 nanowire network. The conversion into the TiO_2 nanowire network was performed within the film by exposure to aqueous precursor solutions and subsequent sintering. Film porosity was controlled by pH-treatment of the weak polyelectrolytes in the assembly. The resulting virus LbL porous TiO_2 nanowire architecture was used as photoanode in a solid-state DSSC, showing better performance compared to a conventional TiO_2 nanoparticle solid-state DSSC under comparable assembly and testing conditions.

Further studies we conducted with 6%+ efficient virus LbL DSSCs (10μm+ thick photoanodes) have shown that virus LbL increases I_{sc} by 9% and increases electron diffusion length (normalized by respective photoanode thickness) by over 300%.[29] This chapter illustrates a simple, readily scalable approach to complex thin film manufacture that can be adapted to many types of substrates, and which may ultimately be designed to replace more traditional nanoparticle technologies.

2.4. References

[1] O'Regan, B., & Grätzel, M. (1991). A low-cost, high-efficiency solar cell based on dye-sensitized colloidal TiO_2 films. *Nature*, *353*, 737-740.

[2] Grätzel, M. (2004). Conversion of sunlight to electric power by nanocrystalline dye-sensitized solar cells. *Journal of Photochemistry and Photobiology A: Chemistry*, *164*(1), 3-14.

[3] Grätzel, M. (2001). Photoelectrochemical cells. *Nature*, *414* (6861), 338-344.

[4] Hardin, B. E., Snaith, H. J., & McGehee, M. D. (2012). The renaissance of dye-sensitized solar cells. *Nature Photonics*, *6*(3), 162-169.

[5] Yip, C. T., Huang, H., Zhou, L., Xie, K., Wang, Y., Feng, T., ... & Tam, W. Y. (2011). Photovoltaic Devices: Direct and Seamless Coupling of TiO2 Nanotube Photonic Crystal to Dye-Sensitized Solar Cell: A Single-Step Approach (Adv. Mater. 47/2011). *Advanced Materials*, *23*(47), 5623-5624.

[6] Kang, S. H., Choi, S. H., Kang, M. S., Kim, J. Y., Kim, H. S., Hyeon, T., & Sung, Y. E. (2007). Nanorod-Based Dye-Sensitized Solar Cells with Improved Charge Collection Efficiency. *Advanced Materials*, *20*(1), 54-58.

[7] Song, M. Y., Ihn, K. J., Jo, S. M., & Kim, D. Y. (2004). Electrospun TiO2 electrodes for dye-sensitized solar cells. *Nanotechnology*, *15*(12), 1861.

[8] Decher, G. (1997). Fuzzy nanoassemblies: toward layered polymeric multicomposites. *Science*, *277*(5330), 1232-1237.

[9] Hammond, P. T. (2004). Form and function in multilayer assembly: New applications at the nanoscale. *Advanced Materials*, *16*(15), 1271-1293.

[10] Hammond, P. T. (2011). Engineering materials layer-by-layer: Challenges and opportunities in multilayer assembly. *AIChE Journal*.

[11] Decher, G., Eckle, M., Schmitt, J., & Struth, B. (1998). Layer-by-layer assembled multicomposite films. *Current opinion in colloid & interface science*,*3*(1), 32-39.

[12] Hammond, P. T. (2012). Building biomedical materials layer-by-layer. *Materials Today*, *15*(5), 196-206.

[13] Lee, S. W., Wood, B. M., & Belcher, A. M. (2003). Chiral smectic C structures of virus-based films. *Langmuir*, *19*(5), 1592-1598.

[14] Lee, S. W., & Belcher, A. M. (2004). Virus-based fabrication of micro-and nanofibers using electrospinning. *Nano letters*, *4*(3), 387-390.

[15] Yoo, P. J., Nam, K. T., Qi, J., Lee, S. K., Park, J., Belcher, A. M., & Hammond, P. T. (2006). Spontaneous assembly of viruses on multilayered polymer surfaces. *Nature materials*, *5*(3), 234-240.,

[16] Bard, A. J. (1979). Photoelectrochemistry and heterogeneous photo-catalysis at semiconductors. *Journal of Photochemistry*, *10*(1), 59-75.

[17] Fox, M. Y. A. (1992). Photocatalysis: Decontamination with sunlight.*Chemtech*, *22*(11), 680-685.

[18] Natarajan, C., Setoguchi, K., & Nogami, G. (1998). Preparation of a nanocrystalline titanium dioxide negative electrode for the rechargeable lithium ion battery. *Electrochimica acta*, *43*(21), 3371-3374.

[19] Birkefeld, L. D., Azad, A. M., & Akbar, S. A. (2005). Carbon monoxide and hydrogen detection by anatase modification of titanium dioxide. *Journal of the American Ceramic Society*, *75*(11), 2964-2968.

[20] Barbe, C. J., Arendse, F., Comte, P., Jirousek, M., Lenzmann, F., Shklover, V., & Grätzel, M. (1997). Nanocrystalline titanium oxide electrodes for photovoltaic applications. *Journal of the American Ceramic Society*, *80*(12), 3157-3171.

[21] Deki, S., Aoi, Y., Hiroi, O., & Kajinami, A. (1996). Titanium (IV) oxide thin films prepared from aqueous solution. *Chemistry Letters*, (6), 433-434.

[22] Aoi, Y., Kobayashi, S., Kamijo, E., & Deki, S. (2005). Fabrication of three-dimensional ordered macroporous titanium oxide by the liquid-phase deposition method using colloidal template. *Journal of materials science*, *40*(20), 5561-5563.

[23] Deki, S., Aoi, Y., Yanagimoto, H., Ishii, K., Akamatsu, K., Mizuhata, M., & Kajinami, A. (1996). Preparation and characterization of Au-dispersed TiO2 thin films by a liquid-phase deposition method. *Journal of Materials Chemistry*,*6*(12), 1879-1882.

[24] Yoo, P. J., Nam, K. T., Qi, J., Lee, S. K., Park, J., Belcher, A. M., & Hammond, P. T. (2006). Spontaneous assembly of viruses on multilayered polymer surfaces. *Nature materials*, *5*(3), 234-240.

[25] DeLongchamp, D. M., Kastantin, M., & Hammond, P. T. (2003). High-contrast electrochromism from layer-by-layer polymer films. *Chemistry of materials*,*15*(8), 1575-1586.

[26] Lutkenhaus, J. L., McEnnis, K., & Hammond, P. T. (2008). Structure and Ionic Conductivity of Microporous Poly(ethylene imine)/Poly(acrylic acid) Layer-by-Layer Assemblies. *Macromolecules*, *41*(16), 6047-6054.

[27] Yang, Y., Qu, L., Dai, L., Kang, T. S., & Durstock, M. (2007). Electrophoresis coating of titanium dioxide on aligned carbon nanotubes for controlled syntheses of photoelectronic nanomaterials. *Advanced Materials*, *19*(9), 1239-1243.

[28] Haque, S. A., Palomares, E., Upadhyaya, H. M., Otley, L., Potter, R. J., Holmes, A. B., & Durrant, J. R. (2003). Flexible dye sensitised nanocrystalline semiconductor solar cells. *Chemical Communications*, (24), 3008-3009.

[29] Chen, P. Y., Ladewski, R., Miller, R., Dang, X., Qi, J., Liau, F. W, Belcher, A. M., & Hammond, P. T. (2013). Layer-by-layer assembled porous photoanodes for efficient electron collection in dye-sensitized solar cells. *Journal of Materials Chemistry A*, *6*(1), 2217-2224.

[30] Law, M., Greene, L. E., Johnson, J. C., Saykally, R., & Yang, P. (2005). Nanowire dye-sensitized solar cells. *Nature materials*, *4*(6), 455-459.

[31] Enache-Pommer, E., Boercker, J. E., & Aydil, E. S. (2007). Electron transport and recombination in polycrystalline TiO nanowire dye-sensitized solar cells.*Applied Physics Letters*, *91*, 123116.

Chapter 2: Metal Oxide 2D Nanowire Network in Lithium Microbattery

3. Metal Oxide 2D Nanowire Network in Lithium Microbattery

3.1. Introduction

As electronics are becoming increasingly ubiquitous in new form factors ranging from flexible cards to miniaturized implantable devices, there is a growing yet unmet demand for high-performance batteries in matching form factors. The M13 virus has a unique ability to float and self-assemble on top of polyelectrolyte multilayers via competitive charge interactions, thermodynamic ordering, and enhanced polyelectrolyte chain mobility.[1] By combining genetically engineered virus templates for biomineralization, layer-by-layer (LbL) assembly methods, and photolithography, we realized the assembly and characterization of a stamped virus LbL microbattery. This method of fabricating and positioning small battery components may enable future high performance microbatteries with complex architectures on flexible substrates. Collaborators in this chapter include Dr. Ki Tae Nam, Dr. Ryan Wartena, and Dr. Pil J. Yoo. Figure 3.2, Figure 3.4, and Figure 3.5 are reprinted and modified from our published report with permission from PNAS.[2]

3.2. Experimental

3.2.1. Cobalt Oxide Nanowire Synthesis

Cobalt oxide nanowires suitable for imaging were created by incubating 100µL E3 virus (~10^{12} viruses/mL) in 1mL of 1mM cobalt chloride aqueous solution ($CoC1_2 \cdot 6H_20$) at room temperature for 30min to promote binding of cobalt ions to the engineered major coat protein, then mixing with 1mL of 5mM sodium borohydride ($NaBH_4$) at room temperature to accelerate the oxidation of nanowires. Cobalt oxide nanowires form

rapidly, reaching 20nm diameter after several minutes, and up to 100nm diameter after several days (Figure 3.1). It is important to note that the appropriate concentrations and ratios of virus and reactants do not scale linearly with total reaction volume. Changing the total reaction volume requires new reaction optimization, similar to (but not as sensitize as) the TiO_2 reaction in Chapter 2.

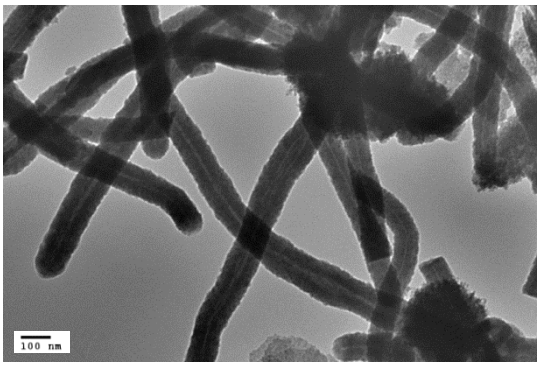

Figure 3.1. Transmission electron microscopy image of virus-templated cobalt oxide nanowires after two days reaction. The virus core is clearly visible as a light line through the nanowire centers. Scale bar is 100nm.

3.2.2. Lithographic Stamp Mold Fabrication

Our procedure for constructing the microbattery electrode is shown in Figure 3.2. A polydimethylsiloxane (PDMS) stamp of embossed microcylindrical patterns was fabricated by thermal-curing the prepolymer over a master silicon mold comprising 8μm-diameter circular wells with 20μm spacing.

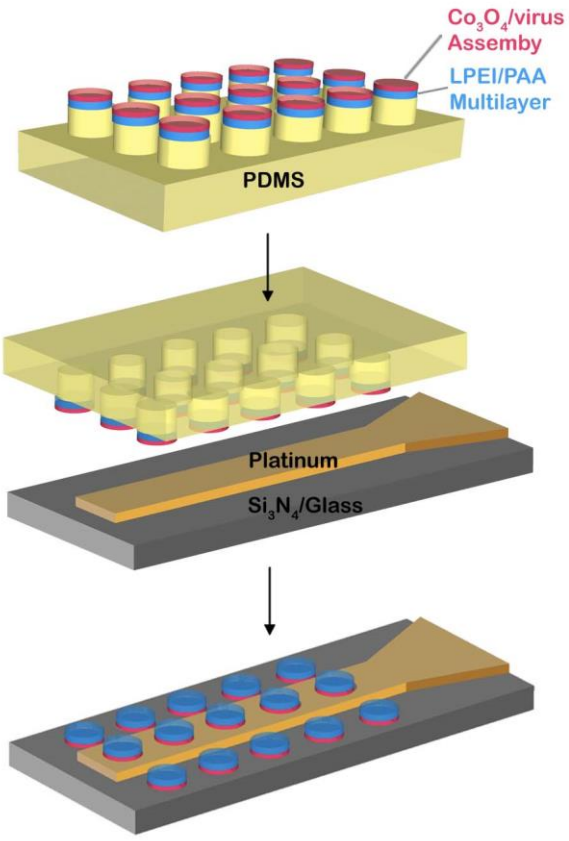

Figure 3.2. Schematic procedure for constructing virus based microbattery electrodes. The virus based cobalt oxide nanowires assembled on the polyelectrolyte multilayer were together stamped as thin 8μm diameter cylinders onto platinum microband current collectors. Copyright 2008 National Academy of Sciences, U.S.A.

Silicon master molds were fabricated via photolithography as outlined in Table 3.1. First, a custom lithography mask was created via computer-aided design (Figure 3.3(a)); second, a top layer of silicon oxide was grown; third, the silicon oxide was patterned with photoresist, exposed to ultraviolet light, and etched to replicate the mask design on the silicon oxide; forth, deep pits were etched to form the master mold with undesirable textured side wall artifacts (Figure 3.3(b)); lastly, the master mold was further processed to smoothen the rough side walls and remove the oxide top cap for facile PDMS insertion and removal (Figure 3.3(c) and Figure 3.3(d)).

Table 3.1. Process for creating silicon master molds for PDMS stamp formation.

Process Stage	Process Step	Description
1. Fabricate mask	Chrome patterning	Chemically etch anti-reflective coating plus chrome layer on soda lime plate according to digitized design pattern.
2. Grow mask oxide	RCA cleaning	Three-step cleaning process: 1) immerse in 1:1:5 solution of NH_4OH:H_2O_2:H_2O at 80°C for 10min then transfer to DI water bath, 2) brief immersion in 1:50 solution of HF:H_2O at 25°C, 3) brief immersion in 1:1:6 solution of HCl:H_2O_2:H_2O at 80°C.
	Oxide growth	Grow 1.1µm thermal field oxide in atmospheric furnace (3h 20min).
3. Pattern oxide	Photoresist coating	Spin-coat 1µm T1HMDS photoresist.
	Masked UV exposure	Mask alignment (35µm mask separation) followed by 3 second exposure to 365-405nm light from high pressure mercury lamp.
	Photoresist development	Automated exposure to photoresist developer solution followed by dump-rinsing and hot plate drying.
	Oxide etching	RF magnetically coupled etching system (~40Å/s) using O_2, CHF_3, and CF_4 gases with helium backside cooling.
	Photoresist strip	O_2 plasma cleaning with 300W RF power for 3min to remove photoresist.
4. Etch silicon	Deep reactive ion etch	Bosch process of time multiplexed deep etching via switching repeatedly between SF_6 etch cycle and C_4F_8 sidewall passivation cycle followed by ion bombardment to remove passivation film from bottom of etched trenches. Uses two independent 13.56MHz RF power supplies: a 1000W supply for a single-turn coil around the etch chamber and a 300W supply connected to the wafer electrode to vary the RF bias potential of the wafer with respect to plasma. ~3:30min for 5µm.
	Polymer strip	O_2 plasma clean with 300W RF power for 3min to remove polymer residue from deep reactive ion etch process.
	Piranha cleaning	10min cleaning in 3:1 mixture of H_2SO_4 : H_2O_2.
	Inspection	Etch verification via SEM imaging.
5. Sculpt sidewalls	RCA cleaning	(same as above)

(repeatable)		
	Thin oxide growth	Grow 0.5µm wet thermal oxide in furnace (90min at 1000ºC, 1h at 600ºC) with N_2, O_2, and H_2 gas.
	Thin oxide strip	Selectively remove oxide sidewalls via buffered oxide etch (5:33 for 0.5µm), a mixture of NH_4F, HF, and H_2O.
6. Remove top oxide caps	Oxide etching	(same as above)
7. Create thin oxide coating	RCA cleaning	(same as above)
	Thin oxide growth	Wet thermal oxide, 25min at 1000µC for 200nm.

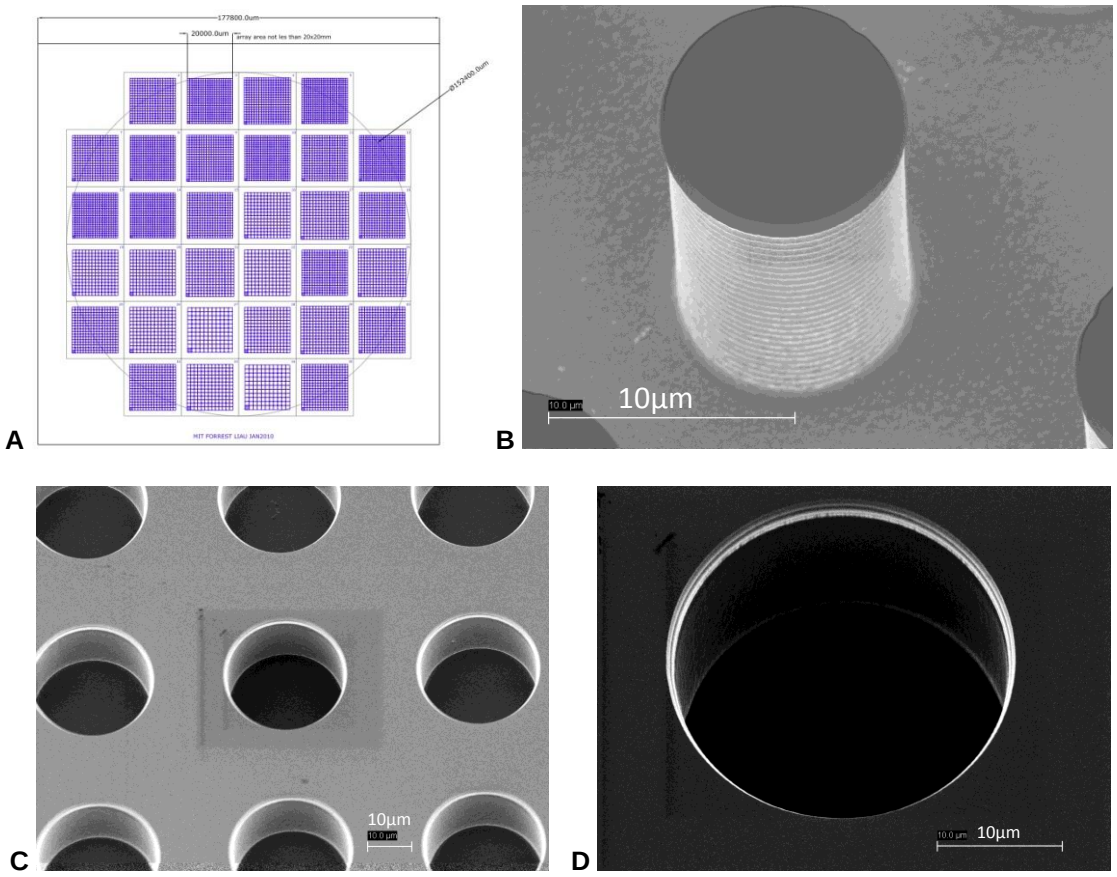

Figure 3.3. Silicon master mold fabrication images. A) Photolithography mask digital design with varying arrays of squares and circles on 150mm silicon wafer. B) Textured side walls and oxide top cap artifacts after deep reactive ion etching of silicon pillar array, shown on silicon pillar. Scale bar is

10µm. C) and D) Final silicon mold (deep wells to form PDMS pillars) after sidewall smoothing and top cap removal. Scale bar is 10µm for both images.

PDMS molds were created by curing prepolymer against the microfabricated silicon master. A 1:10 ratio of curing agent and PDMS prepolymer (Sygard 184, Dow Coming) was mixed and incubated at 70ºC for 3h. PDMS mold stiffness increases with incubation temperature and incubation time. Cured PDMS molds were then peeled from the master and cut into desired sizes.

3.2.3. Virus Floating on Polyelectrolyte Multilayers

Polyelectrolyte multilayers were deposited on the silicon mold patterned PDMS stamp by an electrostatic layer-by-layer assembly technique[3 4] using a programmable slide stainer, similar to Chapter 2. Linear polyethylenimine (LPEI, 25,000 M_r, 0.02M solution) was used as the polycationic building block and anionic polyacrylic acid (PAA, 90,000 M_r, 0.02M, 25% aqueous solution) was used as a counter charged polymer. The LPEI used in this chapter are of much lower molecular weight than the LPEI in Chapter 2 to allow for greater polymer mobility and relatively quick virus floating and dense alignment.[1] Twelve bilayers of both LPEI and PAA were alternately deposited at pH 5. The height of the electrostatically deposited polymeric separator was 150nm, as determined by ellipsometry.

After polymer deposition, 1mL of M13 virus solution (10^{10} viruses/mL, pH 5.0) was dropcast onto the $(LPEI/PAA)_{12.5}$/PDMS, incubated for 30 min above room temperature to allow the viruses to float to the top surface, rinsed with water, dried with nitrogen, then immersed in 15mL cobalt chloride aqueous solution (1mM). After 15min, 15mL of sodium borohydride (5mM) was added to nucleate cobalt oxide on the virus

templates. The polyelectrolyte multilayers served as a solid electrolyte and separator for lithium ion transport.[5]

3.2.4. PDMS Stamping

The microbattery electrodes comprising the virus-templated cobalt oxide anodes and solid polymeric electrolyte were transferred onto four lines of platinum microband current collectors. 8μm diameter cylinders were transferred onto four microbands of 10μm width, 20μm pitch, and 3mm length. During the pattern transfer, a slight pressure was applied to ensure conformal contact between the PDMS mold and the line-patterned platinum electrode.

3.2.5. Inspection of Nanowire Film

The anode and solid electrolyte cylinders assembled on the PDMS stamp were inspected prior to microcontact printing. The stacking order from top to bottom was Co_3O_4/virus/$(LPEI/PAA)_{12.5}$/PDMS. The virus floating is a result of a combination of repulsive interactions between the viruses and interdiffusion between LPEI and PAA.[1] Figure 3.4(a) shows the surface morphology of the 2D virus-only network, and Figure 3.4(b) shows the surface morphology after cobalt oxide synthesis.

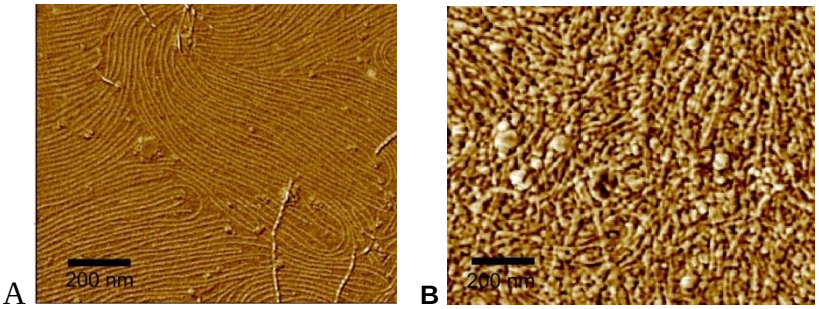

Figure 3.4. AFM images of virus based microbattery electrode on PDMS stamp prior to printing to current collectors. Z range is 2μm. A) Phase mode AFM image of virus assembly before cobalt oxide

growth. B) AFM image of virus based microelectrode after cobalt oxide growth. Scale bars are 200nm. Copyright 2008 National Academy of Sciences, U.S.A.

3.2.6. Electrode Transfer

For electrochemical characterization, the stamped cylinders of electrochemically active anode material and polymer solid electrolyte were transferred to a platinum line pattern. The current collector comprised microbands that broadened at one end to accommodate external electrical contact. On average, one column of microelectrodes was placed across one platinum line. The regions outside the exposed active areas were passivated by a deposition of insulating silicon oxide.

3.2.7. Battery Fabrication

Electrochemical analysis was conducted on the 8μm diameter composite anodes and polyelectrolyte cylinders printed onto platinum microband current collectors jointed to a single external copper contact. The assembled sample was tested against a counterelectrode made of $1cm^2$ lithium foil mounted on copper foil (20μm thick). The test cell was assembled with a porous polymer separator (20μm thick polyethylene-polypropylene) separating the two electrodes. The stacked cell was heat-sealed in a metallized polymer bag, filled with liquid electrolyte (battery-grade electrolyte, 1.3M $LiPF_6$ in propylene carbonate/ethylene carbonate/dimethylene carbonate) and allowed to reach equilibrium before electrochemical testing was initiated.

3.2.8. Electrochemical Evaluation

The assembled cell was cycled between 3.0-0.1V from 255-26nA to examine the microelectrode's charge storage capacity and rate performance, as shown in Figure

3.5(a). At the highest charging rate of 255nA (Figure 3.5(b)), the cell was allowed to rest for 2h (denoted by blue lines) following charging and discharging (denoted by red lines) to observe the polarization relaxation and allow equilibration at a stable open-circuit voltage. Stable cycling is observed, with a broad range of voltage change during charging/discharging and an evolving capacity profile similar to that of Co_3O_4 nanoparticles produced by other methods.[6 7 8] The relatively low rate capability at high charge/discharge rates is typical of transition metal oxides,[9] and could be mitigated by addition of conductive components and optimization of the nanowire/electrolyte interface.

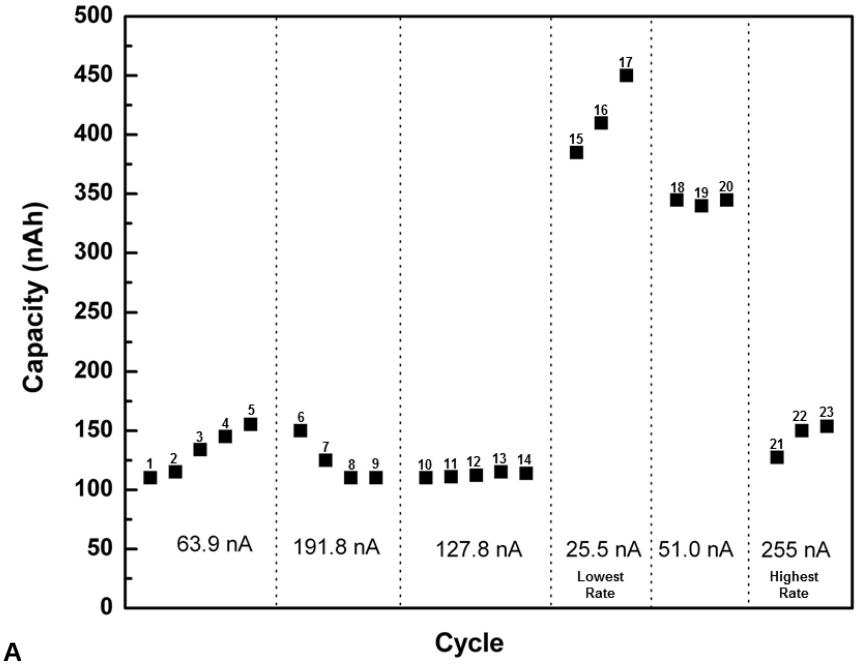

A

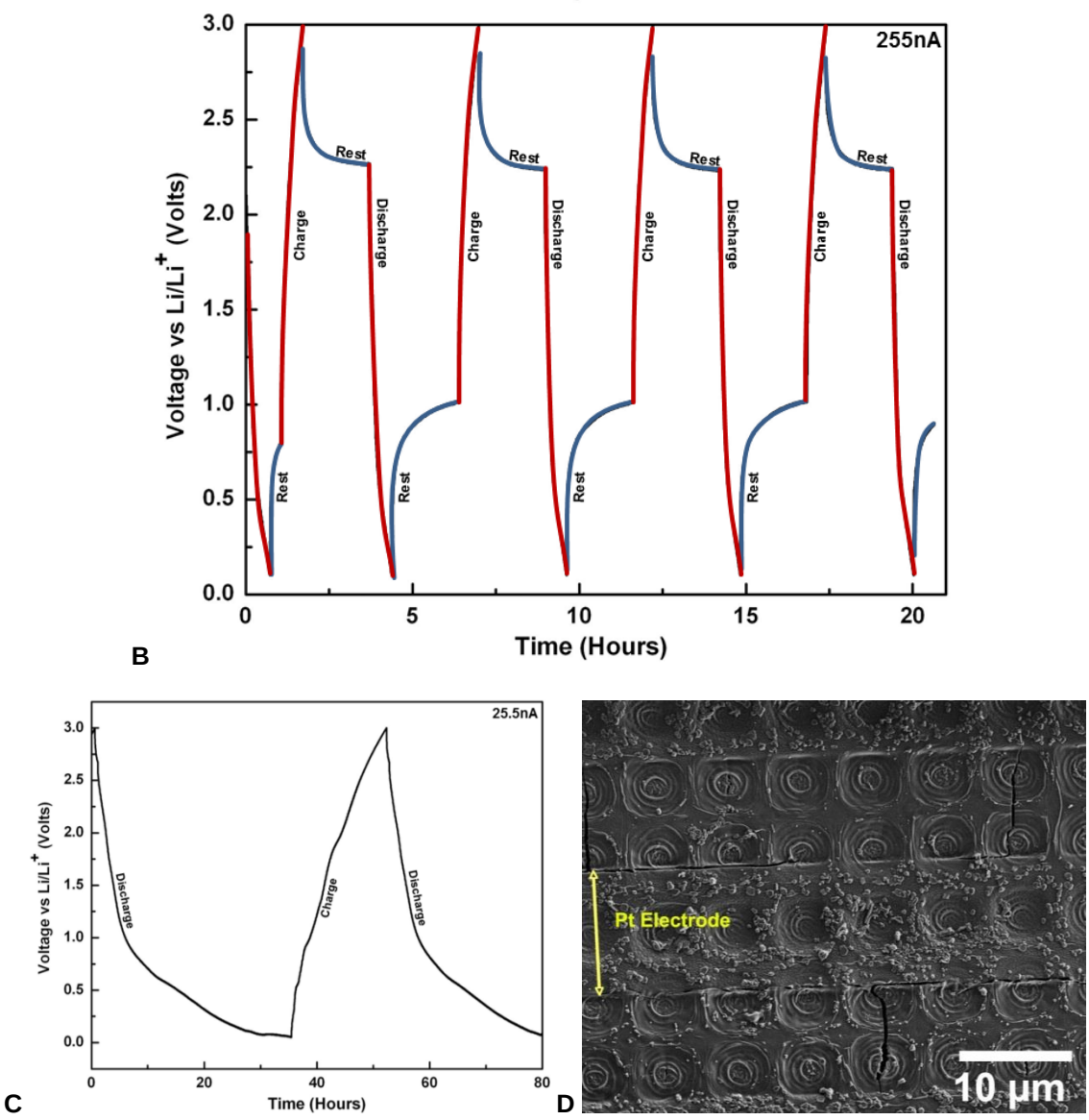

Figure 3.5. Electrochemical testing of stamped microbatteries with virus-templated cobalt oxide electrodes vs. Li /Li$^+$ cell. A) Capacity vs. cycle number for the same cell at different charging currents. B) Charge-discharge curve (3V to 0.1V) at the highest rate of 255nA with 2h rests for cell equilibration. C) Charge-discharge (3V to 0.1V) at the lowest rate of 25.5nA without rest. D) Scanning electron microscopy (SEM) image of disassembled electrode after cycling at various rates. Copyright 2008 National Academy of Sciences, U.S.A.

At the slowest charging rate of 25.5nA (Figure 3.5(c)), the microelectrode array showed discharge capacity ranging from 375 to 460nAh (Figure 3.5(a)). In previous work with platinum current collectors, we found that the platinum itself can contribute a

limited amount of lithium storage capacity via formation of intermetallic compounds at slow charging rates. In the current geometry, the four platinum microbands are expected to contribute approximately 4nAh capacity or 10% of the total capacity measured with the slow charging rate. Figure 3.5(d) shows that the microbattery electrodes are structurally stable and do not fall apart from the platinum electrodes after 25 cycles. Some circular wrinkling was observed, possibly driven by the swelling and evaporation of solvent in the polyelectrolyte multilayers as they were also present prior to battery testing.

The gravimetric specific capacity ($mAh/g_{electrode}$) was not calculated because the exact mass of cobalt oxide in the microelectrode could not be determined. However, we assume that the specific capacity of the virus-based cobalt oxide nanowires should be similar to previous data[10] (but on a 2D planar assembly) because these nanowires were synthesized using a similar method. Since there are 150 microelectrodes on each platinum microband, we estimate that each microelectrode had a storage capacity between 625-767pAh/microelectrode. Direct comparison to other microbattery assembly approaches, such as thin-film vapor deposition[11], laser direct-write printing[12], and sol gel printing[13], cannot be made easily due to large differences in the electrode materials tested and the electrode geometries.

3.3. Conclusion

The approach we presented in this chapter for combining polymer electrostatic assembly techniques with nanowire self-assembly, biotemplated synthesis, and soft lithography may be used to construct small-scale power sources embedded in various electronic system structures. Microelectrodes can be easily stamped on a variety of rigid

or flexible substrates to construct microbatteries with stable, reliable performance. This versatile approach incorporating both biological and non-biological assembly techniques may provide greater flexibility for implementing advanced battery designs such as those with interdigitated microelectrodes or 3D architectures, and may enable new designs for other device types such as various sensors and solar cells.

3.4. References

[1] Yoo, P. J., Nam, K. T., Qi, J., Lee, S. K., Park, J., Belcher, A. M., & Hammond, P. T. (2006). Spontaneous assembly of viruses on multilayered polymer surfaces. *Nature materials*, *5*(3), 234-240.

[2] Nam, K. T., Wartena, R., Yoo, P. J., Liau, F. W., Lee, Y. J., Chiang, Y. M., ... & Belcher, A. M. (2008). Stamped microbattery electrodes based on self-assembled M13 viruses. *Proceedings of the National Academy of Sciences*,*105*(45), 17227-17231.

[3] Hammond, P. T. (2004). Form and function in multilayer assembly: New applications at the nanoscale. *Advanced Materials*, *16*(15), 1271-1293.

[4] Park, J., & Hammond, P. T. (2004). Multilayer Transfer Printing for Polyelectrolyte Multilayer Patterning: Direct Transfer of Layer-by-Layer Assembled Micropatterned Thin Films. *Advanced Materials*, *16*(6), 520-525.

[5] Lutkenhaus, J. L., & Hammond, P. T. (2007). Electrochemically enabled polyelectrolyte multilayer devices: from fuel cells to sensors. *Soft Matter*, *3*(7), 804-816.

[6] Poizot, P., Laruelle, S., Grugeon, S., Dupont, L., & Tarascon, J. M. (2000). Nano-sized transition-metal oxides as negative-electrode materials for lithium-ion batteries. *Nature*, *407*(6803), 496-499.

[7] Larcher, D., Sudant, G., Leriche, J. B., Chabre, Y., & Tarascon, J. M. (2002). The Electrochemical Reduction of Co_3O_4 in a Lithium Cell. *Journal of The Electrochemical Society*, *149*(3), A234-A241.

[8] Grugeon, S., Laruelle, S., Dupont, L., & Tarascon, J. M. (2003). An update on the reactivity of nanoparticles Co-based compounds towards Li. *Solid state sciences*, *5*(6), 895-904.

[9] Taberna, P. L., Mitra, S., Poizot, P., Simon, P., & Tarascon, J. M. (2006). High rate capabilities Fe3O4-based Cu nano-architectured electrodes for lithium-ion battery applications. *Nature materials*, *5*(7), 567-573.

[10] Nam, K. T., Kim, D. W., Yoo, P. J., Chiang, C. Y., Meethong, N., Hammond, P. T., ... & Belcher, A. M. (2006). Virus-enabled synthesis and assembly of nanowires for lithium ion battery electrodes. *science*, *312*(5775), 885-888.

[11] Bates, J. B., Dudney, N. J., Neudecker, B., Ueda, A., & Evans, C. D. (2000). Thin-film lithium and lithium-ion batteries. *Solid State Ionics*, *135*(1), 33-45.

[12] Wartena, R., Curtright, A. E., Arnold, C. B., Piqué, A., & Swider-Lyons, K. E. (2004). Li-ion microbatteries generated by a laser direct-write method. *Journal of power sources*, *126*(1), 193-202.

[13] Dokko, K., Sugaya, J. I., Nakano, H., Yasukawa, T., Matsue, T., & Kanamura, K. (2007). Sol–gel fabrication of lithium-ion microarray battery. *Electrochemistry communications*, *9*(5), 857-862.

Chapter 4: Metal 3D Nanowire Network for Lithium Battery

4. Metal 3D Nanowire Network for Lithium Battery

4.1. Introduction

The growing demand for more advanced batteries is multi-faceted, with different priorities for different emerging applications. For example, disposable mass consumer batteries demand lower cost and greater environmental sustainability, while batteries in commercial aircraft demand high energy density and greater stability. While Chapter 3 describes the need for smaller, more flexible batteries for electronic device miniaturization, this chapter is set in context of the need for lighter weight batteries, e.g. for use in micro aerial vehicles,[1] comprising electrodes that can provide some structural support for the vehicle system to reduce the need for redundant packaging.

In this chapter, we demonstrate covalent crosslinking of the M13 virus into a three-dimensional biotemplate in the form of hydrogels. The resulting hydrogels are mineralized to 3D metallic nanowire scaffolds using electroless deposition with control of nanowire diameter, scaffold porosity, and film thickness. While the 3D nanowire networks in Chapter 2 were built layer-by-layer, whole nanowire networks in this chapter were fabricated at once. The nanowire networks were further functionalized via galvanic displacement to tin for use as lithium rechargeable battery anodes. We envision that these 3D nanowire networks could serve as a tunable, scalable design element across non-battery devices as well, e.g., provide a 3D conductive network for nanoporous materials in photovoltaics, catalytic systems, filters, and sensors.

Numerous energy related fields have developed nanostructured materials to improve objective device performance. Photovoltaics, fuel cells, electro-optical, and lithium rechargeable batteries are just a few examples.[2 3 4 5] There have been numerous

efforts to create 3D porous nano-architectures to improve the performance of these devices.[6 7 8 9 10 11] While many novel structures have been synthesized, in some cases scale-up of the materials would be prohibitively expensive. Further, assembling nanomaterials into practical devices can pose challenges in terms of packaging and integration. For some applications such as lithium rechargeable batteries, nano-structured materials require additional conductive additives and organic binders.

For energy storage applications, there is an increasing demand for lightweight power sources and electrode architectures that eliminate the need for conductive and organic additives. Reducing supporting electrode mass would increase specific energy and power density, and a dual-functional electromechanical material that functions as both an energy source and structural material would improve a miniaturized system's range and mission longevity. Here we outline a general approach to assemble M13 viruses into a 3D biotemplate, convert the template to a 3D conductive scaffold, and then further functionalize the conductive scaffold for particular applications, in this case, lithium batteries. Mechanical characterization of virus-templated 3D metal nanowire networks is described in Chapter 5. Collaborators in this chapter include Dr. Fred John Burpo, Brandon Lew, and Jacqueline Ohmura. Portions of this chapter are reprinted from our research reports.[12]

4.2. Experimental

4.2.1. Virus Crosslinking

Three different virus clones are used in this chapter: The first is named E3 and consists of three consecutive glutamate residues and an aspartate at the solvent exposed N-terminus of the p8 proteins providing pH controllable charge, as described in the thesis

introduction and used in Chapters 2 and 3. The second clone is identical to E3 on the outside of the capsid, but a mutation of tyrosine to methionine at the 21st residue on the p8 protein results in a nearly 10-fold increase in persistence length. This clone is named Y21M, also called "stiff virus." The third is a single-walled carbon nanotube binding clone named DSPH.

To synthesize 3D metal nanowire scaffolds, the M13 virus was crosslinked into a hydrogel to serve as a 3D biotemplate. Previous work using the M13 virus to assemble fibers employed glutaraldehyde as the crosslinking agent.[17 13 14] Glutaraldehyde is a bifunctional aldehyde on a five carbon chain and is a commonly used molecule to crosslink proteins. The bifunctional character of the glutaraldehyde molecule facilitates the covalent linkage between two virus particles.

To investigate the crosslinking approach, a highly concentrated virus solution was crosslinked with glutaraldehyde to form a gel. To prevent the structure from collapsing by capillary action, the gel was soaked in ethanol to displace water and then supercritically dried with CO_2. Figure 4.1(a) shows a supercritically dried sample of 0.1mL virus gel (left) in comparison to an ambient-dried, collapsed one (right). Both samples had approximately the same initial volume, indicating that significant capillary shrinking occurred with the ambient-dried sample. Freeze drying is an alternative technique to critical point drying, involving the simple freezing and sublimation of water. Details of these drying methods can be found in the Appendix.

It has been shown that freeze drying can maintain the structural integrity of nanostructured peptide networks.[15] SEM images of ambient dried, supercritically dried, and freeze dried virus gels are shown in Figure 4.1(b), (c), and (d), respectively. Ambient

air drying produces high density, low porosity structures with no visible separation between viruses; supercritical drying produces high density structures with visible separation between viruses; and freeze drying produces highly porous structures with visible separation between rope-like bundles of viruses.

A

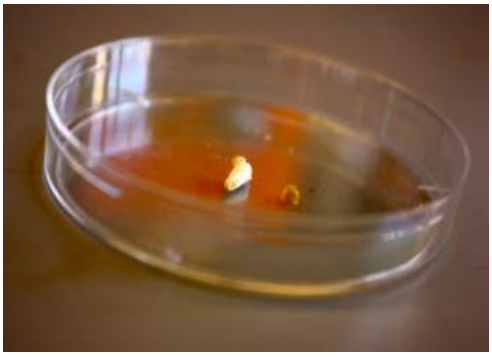

B

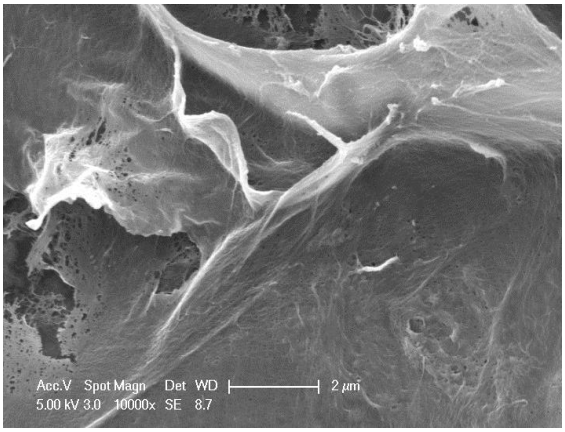

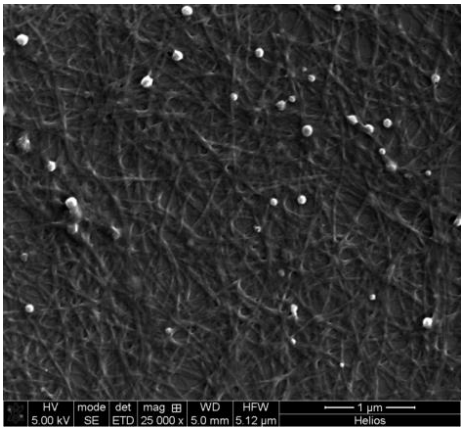

C

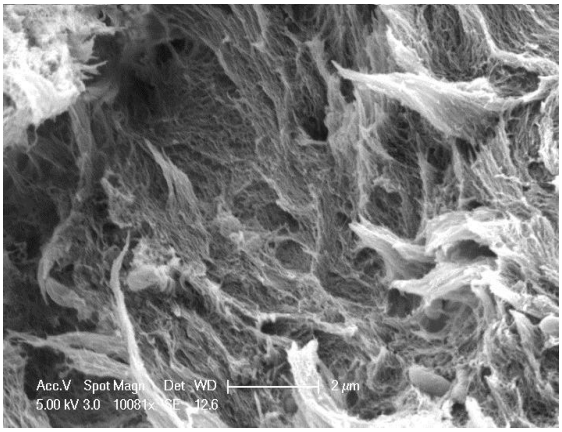

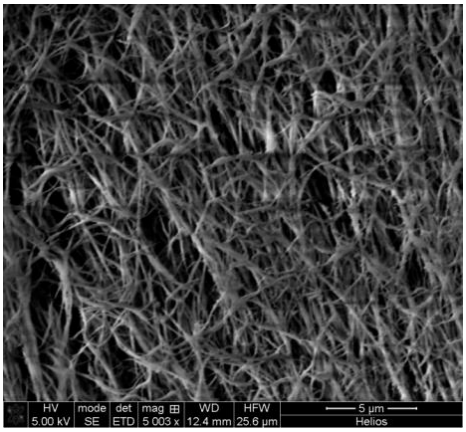

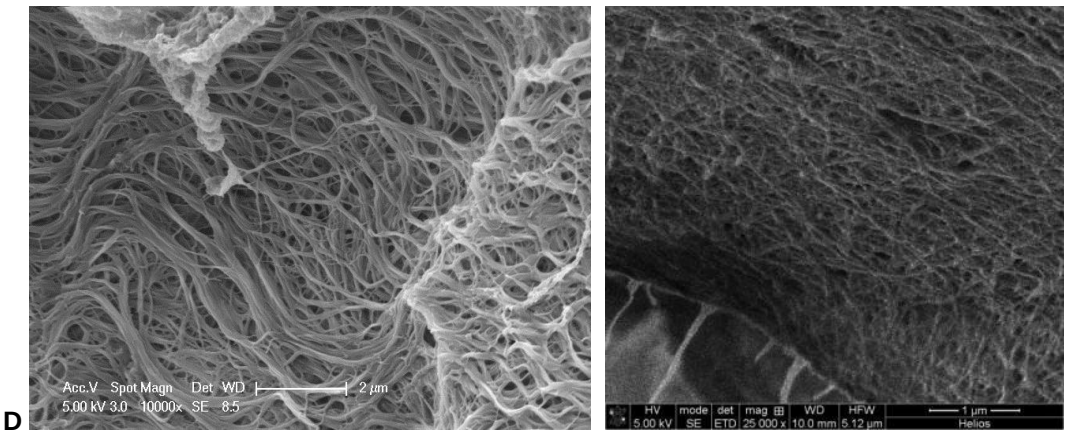

Figure 4.1. Drying method comparison with virus gels. A) Size comparison of 0.1mL virus gel pellets after supercritical drying (left) and ambient air drying (right). Scanning electron microscopy (SEM) images: B) Virus gel dried in ambient air. Scale bars are 2µm left and 1µm right. C) Virus gel dried via supercritical CO_2. Scale bars are 2µm left and 5µm right. D) Virus gel freeze dried in water. Scale bars are 2µm left and 1µm right.

To create films of virus gels with controlled thickness, we utilize the difference in glutaraldehyde specific gravity compared to water. The specific gravity of 50% glutaraldehyde solution is 1.106, which sinks in water. Virus solution is dropcast onto a silicon substrate, inverted and then placed in contact with a reservoir of 50% glutaraldehyde solution creating a one-dimensional diffusion profile of glutaraldehyde into the virus solution.

The virus solution and glutaraldehyde form a distinct liquid-liquid interface due to the difference in specific gravities. In addition to dropcasting the virus on a substrate to develop a hydrogel film, we observed that virus solutions crosslink into the geometry of the solution. E.g., a microfuge tube partially filled with 0.5ml glutaraldehyde solution and 100µl of E3 virus at concentration of 1×10^{14} viruses/mL results in a hydrogel pellet shown in Figure 4.2(a). Similarly, 8mm diameter wells were created using 1mm thick rubber on a silicon substrate.

The rubber wells were filled with virus solution, inverted, and cross-linked on glutaraldehyde shown in Figure 4.2(b). This technique allows for control over the hydrogel thickness by controlling the geometry of the virus solution during crosslinking. Control over gel density is achieved by controlling the initial virus concentration.

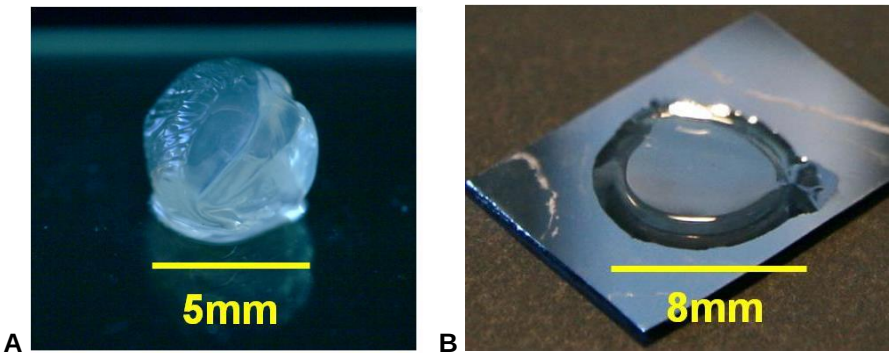

Figure 4.2. Three-dimensional virus template synthesis. A) Hydrogel pellet. B) Hydrogel film.

4.2.2. Metal Deposition Chemistry

In order to use the hydrogels to mineralize copper and nickel nanowires from electroless deposition (ELD) solutions, the virus particles needed to be sensitized with a catalyst to mediate the reduction of cation precursors that are otherwise stable in the presence of reducing agent within the ELD solutions. Using $Na_2Pd(NH_3)_4$ salt, the predominant ionic species in solution is expected to be the $[(NH_3)_4Pd]^{2+}$ complex.[16] With four carboxylate amino acids at the N-terminus of the p8 protein, at neutral pH values, the positively charged palladium complex is expected to electrostatically bind the virus. Virus hydrogels were exposed to 10mM $(NH_3)_4PdCl_2$ for 6h to allow for diffusion and ion binding. After palladium exposure, the gels were rinsed in 3-(N-morpholino) propanesulfonic acid (MOPS) buffer for 12h to remove excess palladium ions.

The palladium sensitized gels were then immersed in a copper ELD solution. In general, electroless deposition solutions consist of a precursor metal ion to be reduced, a reducing agent, a complexing agent to stabilize the metal ion in the presence of the reducing agent, and a buffer to prevent pH variation and ensure that the desired product is plated.[17] The copper electroless deposition used in this chapter was modified from the formulation used by Balci *et al*. to synthesize copper nanoparticles within the core of the tobacco mosaic virus.[18] Figure 4.3 shows the copper nanowire networks at multiple length scales. Energy dispersive x-ray (EDX) analysis indicated high purity nanowires with a copper and nickel compositions consistently above 98%. X-ray diffraction (XRD) analysis confirmed the copper crystal structure as face centered cubic and reveals a minor oxide peak. The copper 3D films were measured via 4-point probe to have resistivity only 60 times their bulk metal counterparts without any purification treatments (Table 4.1).

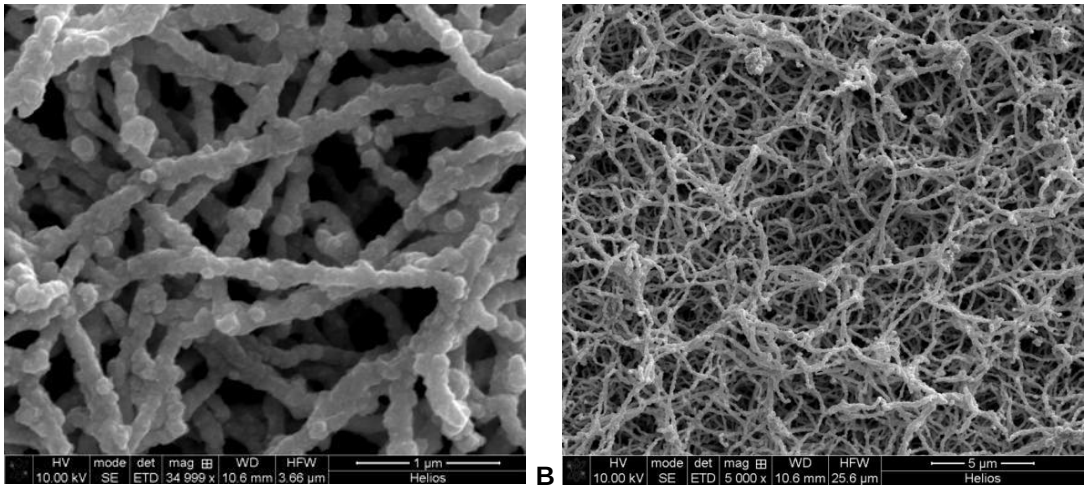

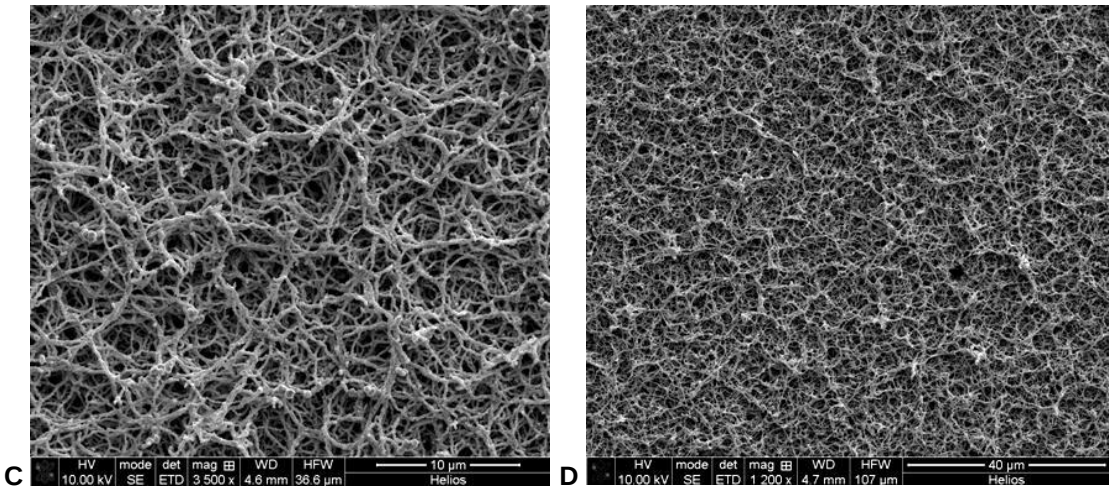

Figure 4.3. Copper nanowire networks at various scanning electron microscopy (SEM) magnifications. Scale bars are (a) 1µm, (b) 5µm, (c) 10µm, and (d) 40µm.

Table 4.1. Electrical resistivity of virus-templated copper nanowire 3D networks.

Nanowire Diameter (nm)	Film Thickness (µm)	Resistance (Ω)	Ω/square	Measured ρ (Ω·m)	Bulk ρ (Ω·m)	$\rho_{measured}$ / ρ_{bulk}
115	10.3	0.02359	0.11	1.10×10^{-6}	1.70×10^{-8}	64.96
139	11.8	0.01999	0.09	1.07×10^{-6}	1.70×10^{-8}	62.74
188	20.9	0.01137	0.05	1.07×10^{-6}	1.70×10^{-8}	63.23

4.2.3. Nanowire Network Formation on Structured Substrate

Nanowire network film thickness and nanowire orientation can be controlled by use of structured substrates such as the well/pillar arrays used in Chapter 3, and fiber mats or other textured surfaces. Figure 4.4 shows oriented copper nanowire networks created by wetting a 30µm-thick glass fiber mesh cloth with virus solution and then proceeding with glutaraldehyde crosslinking and copper ELD. Figure 4.5(a) shows a single layer of copper nanowires wrapped tightly around the glass fibers, demonstrating the potential of using anisotropic substrate features to directionally align viruses and virus-templated nanowires. Figure 4.5(b) shows copper ELD particles on glass fibers without virus, for comparison.

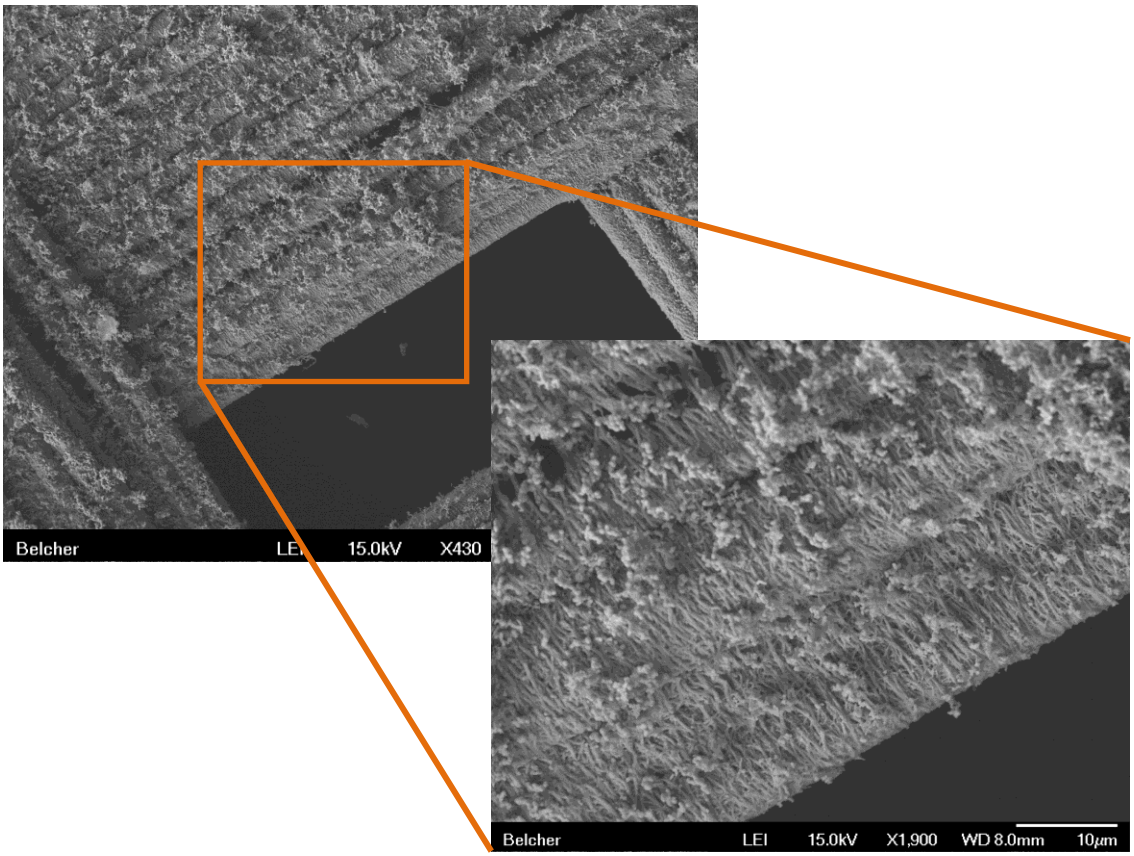

Figure 4.4. SEM image of copper nanowire network on woven glass fiber substrate. Overall nanowire network thickness is determined by the thickness of the glass fiber fabric. Nanowires show preferred orientation perpendicular to the underlying glass fibers. Scale bar is 10µm on insert.

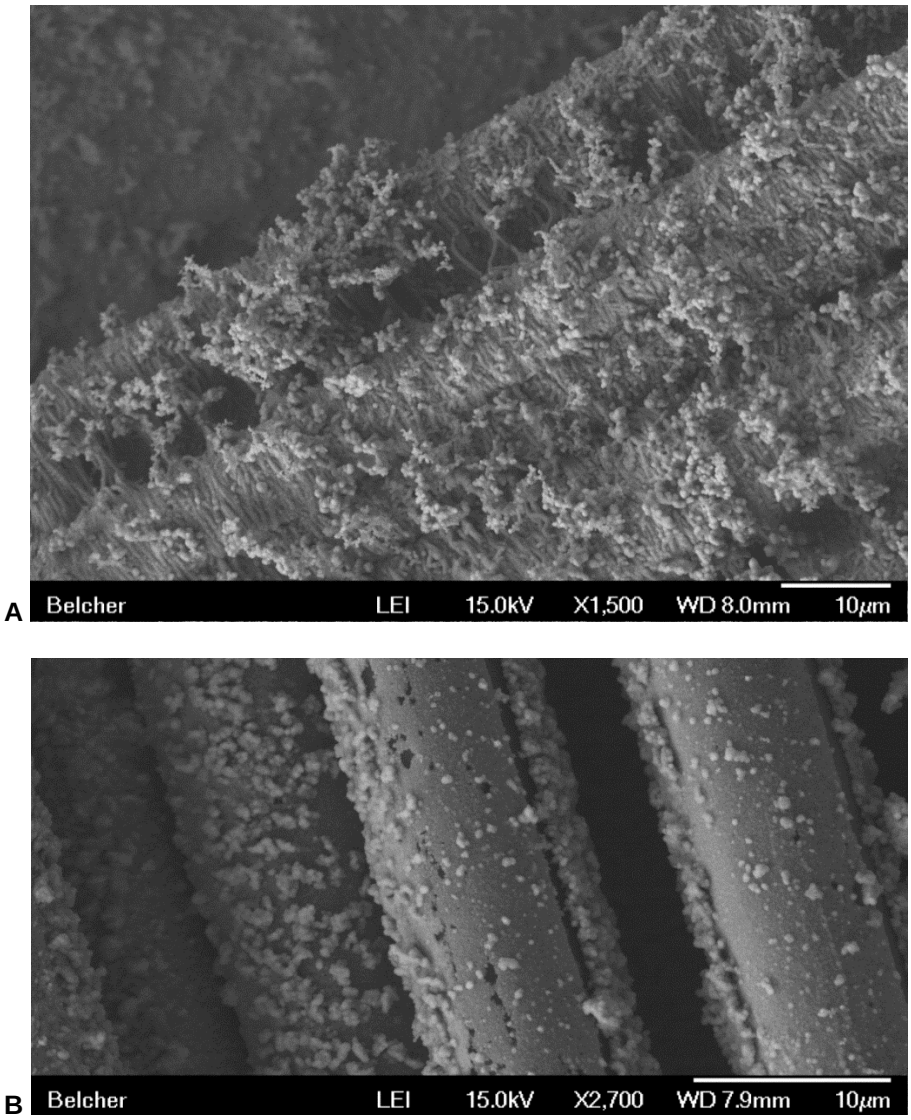

Figure 4.5. Copper deposited on glass fibers with and without virus. A) Copper nanowires wrapping around glass fibers with some nanowires crossing between fibers, created by first distributing viruses on the glass fiber mesh via capillary action followed by crosslinking and electroless deposition. B) Glass fibers with electroless deposited copper, displaying no oriented structures.

4.2.4. Film Porosity Characterization

The nanowire network film porosity is influenced by a variety of experimental factors, including initial virus concentration, virus clone choice, hydrogel crosslinking time, nanowire diameter, and drying method. Two parameters were analyzed as possible

methods to control scaffold porosity, the first of which was the virus clone. Of the two virus clones used for comparison, E3 and Y21M, both have identical solvent exposed proteins on the viral capsid. The Y21M clone, however, has a mutation from tyrosine to methionine at the 21st residue on the p8 coat protein. This site specific mutation gives the Y21M clone a persistence length of $9.9 \pm 0.7\mu m$ compared to $2.8 \pm 0.7\mu m$ for unaltered wild-type M13.[19] The longer persistence length of the Y21M is expected to create longer element lengths in hydrogel formation, and consequently result in increased inorganic scaffold porosity when compared to the E3 biotemplate.

The second method used to control porosity was freeze drying. Once the metal nanowire films were synthesized and rinsed, the still hydrated films were subject to freeze drying. The expectation was that the capillary forces created during film drying could be decreased, preserving a higher porosity in the film, since freeze drying was used previously on a crosslinked virus pellet to preserve post-dehydration porosity (Figure 4.1(d)).

A virus concentration of 7×10^{13} viruses/mL was used for both E3 and Y21M clones in the copper ELD bath. Nanowire film porosities were determined both gravimetrically and with image analysis of focused ion beam (FIB) cross-sections. Copper nanowire films were ion etched using a dual beam SEM/FIB to image the cross-sectional film thickness. The average of the two methods indicates a higher porosity for Y21M films compared to E3. For copper films, the porosities were 54.6% for E3 and 64.8% for Y21M. The freeze dried E3 copper film had 75.7% porosity. The results for each method are listed in Table 4.2 and FIB cross-section images used for porosity analysis are shown in Figure 4.6, Figure 4.7, and Figure 4.8. Virus clone selection

provides a roughly 10% change in porosity while freeze drying increases porosity slightly over 20%.

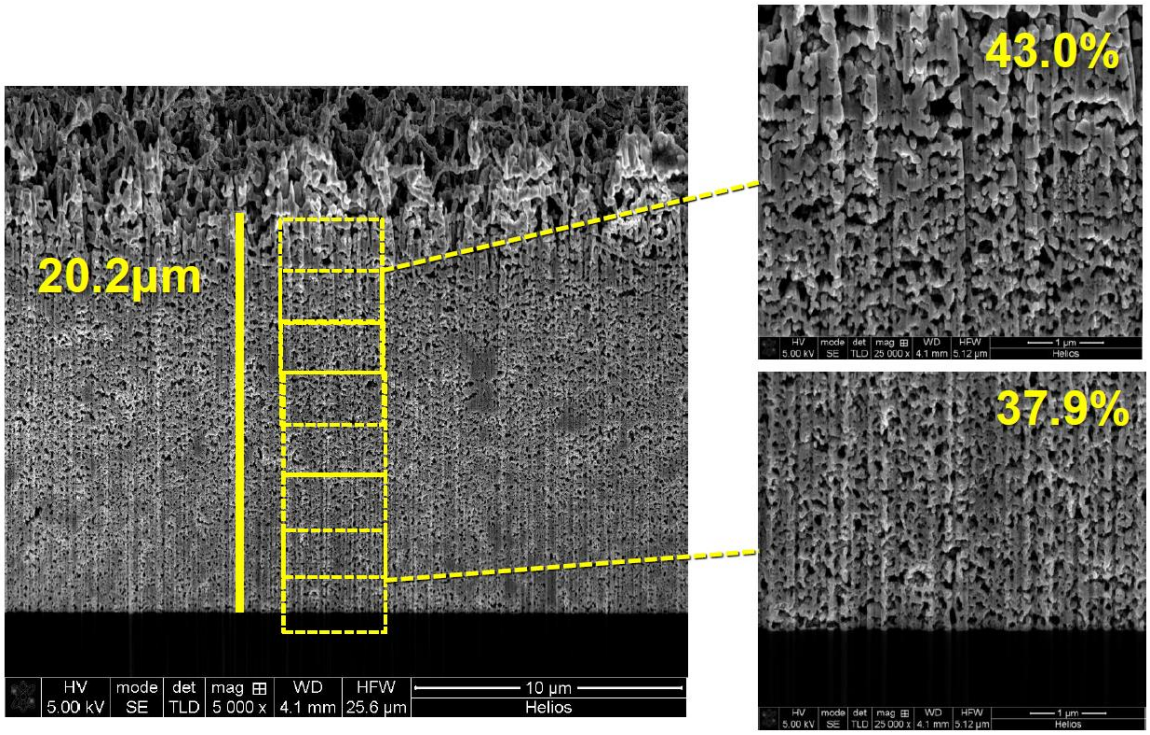

Figure 4.6. Porosity analysis of copper nanowires synthesized on E3 virus. Scanning electron microscopy (SEM) images obtained using a focused ion beam (FIB) etch to determine film thickness. ImageJ software was used to determine porosity for each section bounded by dashed yellow boxes. Porosity decreased from 54.3% to 39.0% from the top to the bottom of the film with overall average porosity of 48.6%.

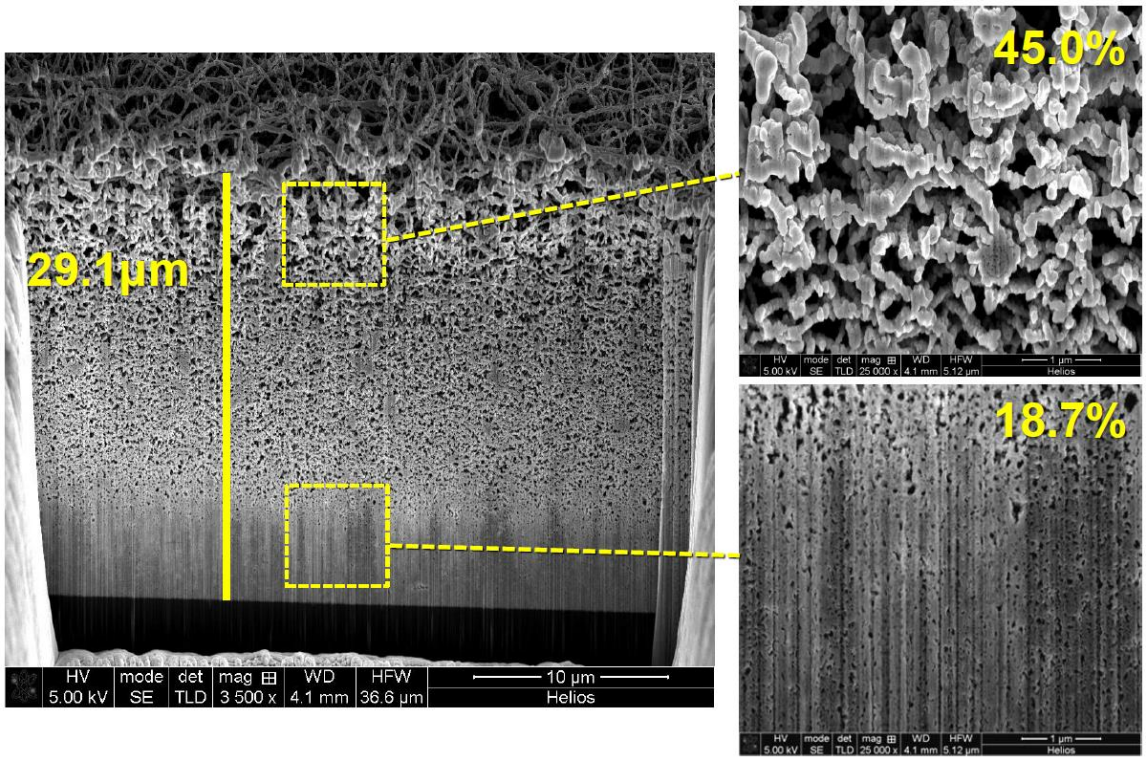

Figure 4.7. Porosity analysis of copper nanowires synthesized on Y21M virus. Scanning electron microscopy (SEM) images obtained using a focused ion beam (FIB) etch to determine film thickness. ImageJ software was used to determine porosity for each section bounded by dashed yellow boxes. Porosity decreased from 61.4% to 54.4% from the top to the bottom of the film with overall average porosity of 56.3%.

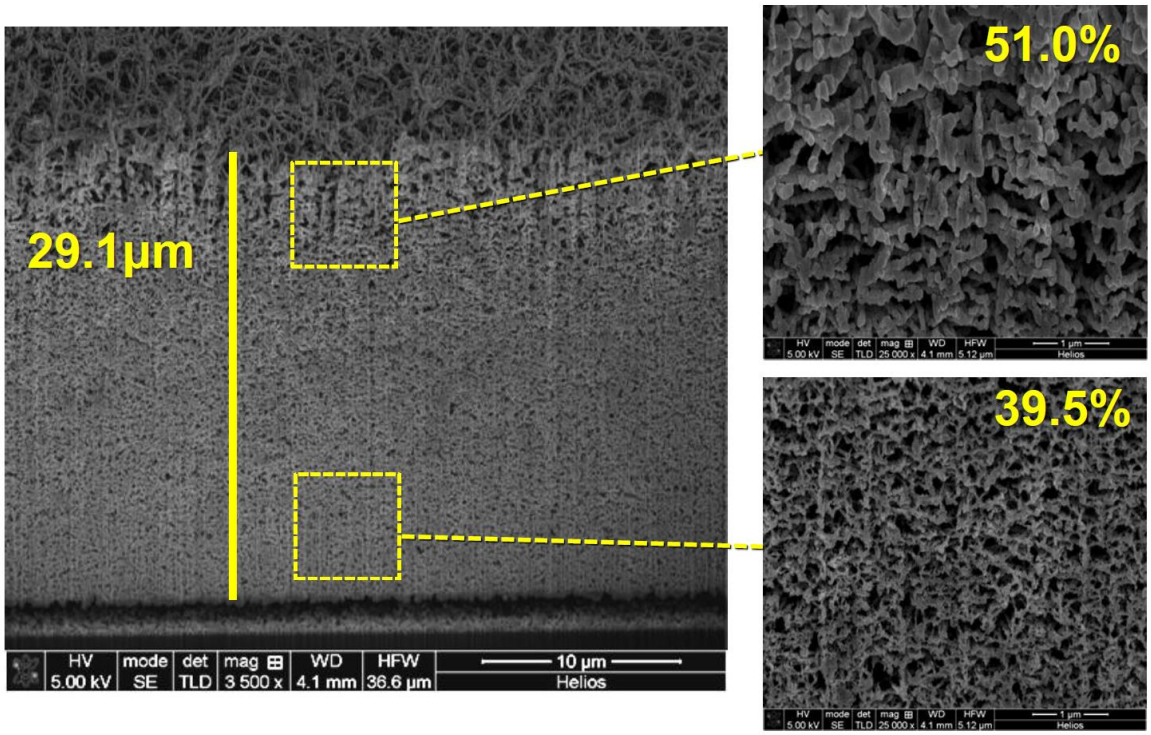

Figure 4.8. Porosity analysis of copper nanowires synthesized on E3 virus and freeze dried. Scanning electron microscopy (SEM) images obtained using a focused ion beam (FIB) etch to determine film thickness. ImageJ software was used to determine porosity for each section bounded by dashed yellow boxes. Porosity decreased from 70.5% to 55.4% from the top to the bottom of the film with overall average porosity of 62.1%.

Table 4.2. Nanowire network porosity comparison. Y21M stiff virus templates produce more porous structures than their E3 virus counterparts. Freeze drying significantly increases film porosity and pore uniformity.

Method	Cu on E3	Cu on Y21M	Cu on E3 freeze-dried
Gravimetric	60.6±1.7	73.2±9.3	89.3
Image Analysis	48.6	56.3	62.1
Average	54.6	64.8	75.7

4.2.5. Non-Porous Layer Removal

A non-porous copper film can form on the substrate side of thick copper nanowire network films as a result of substrate contact during synthesis and subsequent heat treatment for film delamination, as shown in Figure 4.9(a) and (b). These non-porous

films can be removed through contact with nitric acid. Figure 4.9(c) and (d) show complete through-film porosity achieved by lightly brushing the non-porous bottom with a cotton swap soaked with nitric acid. The image sample is a virus-templated copper nanowire film that has been folded over, allowing separate SEM focusing on the bottom and top sides for direct microstructure comparison.

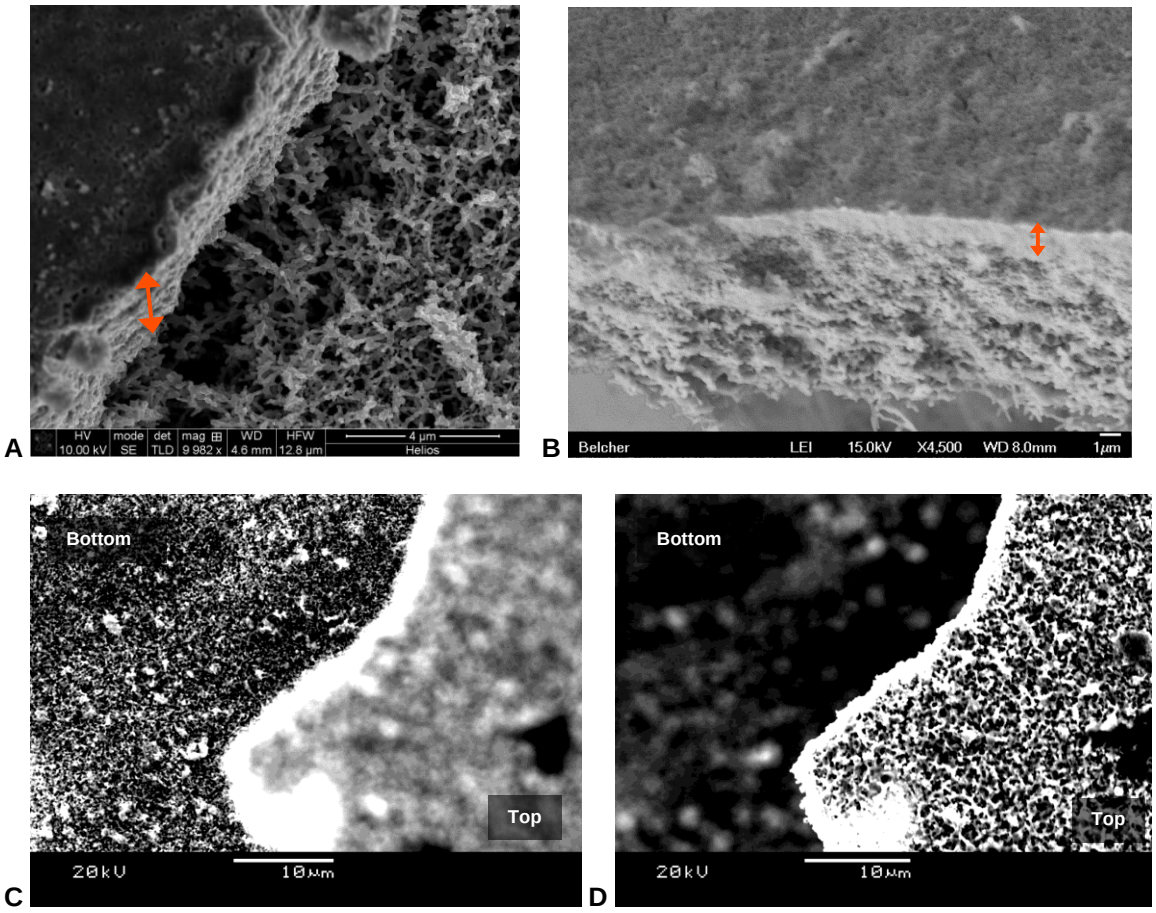

Figure 4.9. Acid treatment for non-porous film removal on top of nanowire network films. A) and B) Scanning electron microscopy (SEM) images of non-porous film artifact to be removed via nitric acid contact. C) SEM image of folded copper nanowire network film (showing both top and bottom sides) after nitric acid treatment, with focus on bottom side to show surface porosity. D) SEM image of same folded copper nanowire network film after nitric acid treatment, with focus on top side to show likewise surface porosity. Complete through-film porosity was achieved.

4.2.6. High Temperature Stability

Morphological stability of the virus-templated copper nanowire networks at elevated temperatures was evaluated in ambient air as well as in a forming gas environment (4% hydrogen, 96% argon) to prevent oxidation. Figure 4.10 shows SEM images of the copper nanowire networks after heat treatment in forming gas and air. At 450˚C in forming gas, the nanowires fuse with one another but retain high aspect ratio and porosity. However, at 450˚C in air and 600˚C in forming gas, significant coalescence is observed.

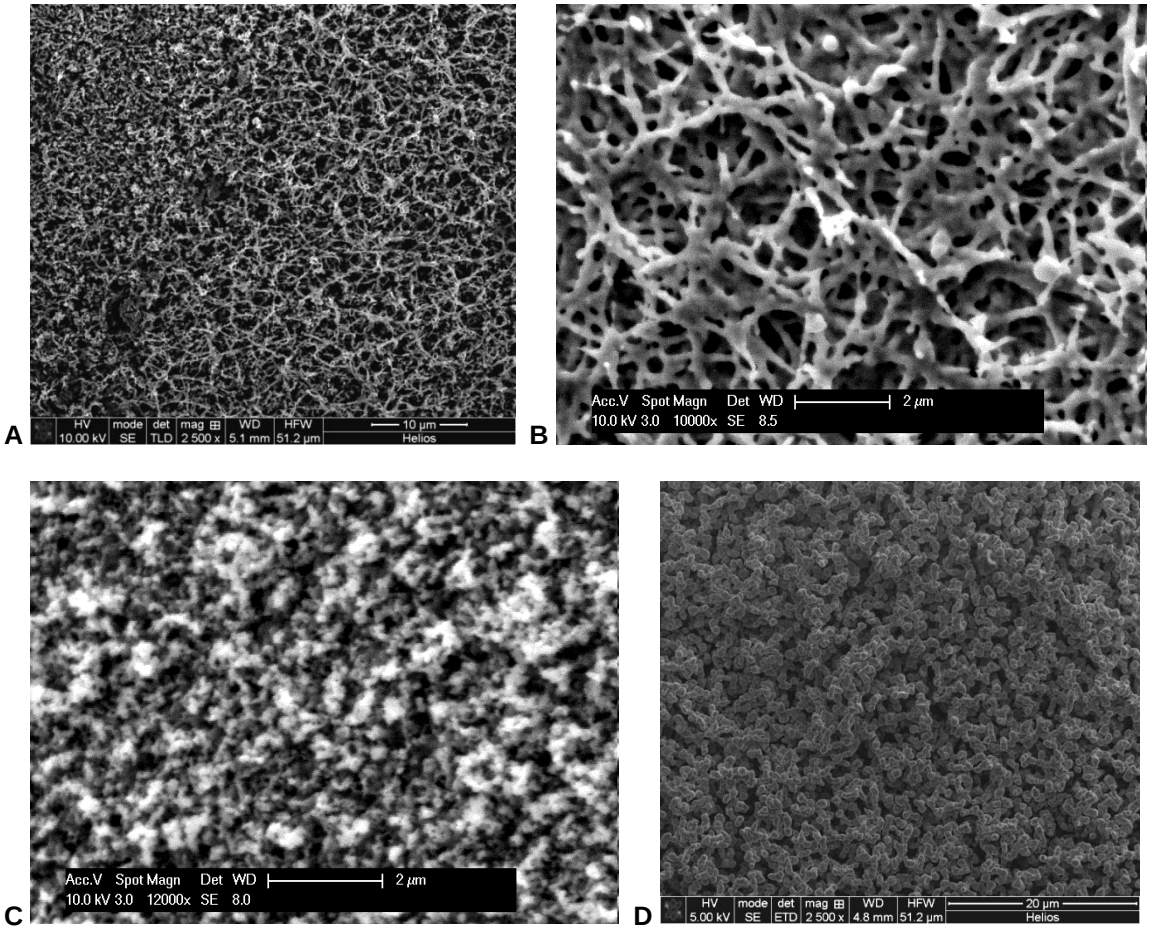

Figure 4.10. Scanning electron microscopy (SEM) images of copper nanowire networks after heat treatment. A) No heat treatment. B) 450˚C anneal for 30min in forming gas (4% hydrogen, bal. argon). C) 450˚C anneal for 30min in air. D) 600˚C anneal for 30min in forming gas.

4.2.7. Copper Mesh Integration

The finest commercially available metal mesh comprise interwoven metal fibers of 50µm diameter forming a grid with fiber-to-fiber spacing of 100µm. Virus-templated copper nanowire network films can be bonded to existing copper fiber mesh to form a hierarchically organized copper mesh that is nanoporous yet highly conductive and flexible. Mesh integration can be achieved by crosslinking viruses directly on copper mesh prior to ELD reaction, as shown in Figure 4.11(a); or by fabricating a nanowire film separately and then fusing the nanowire network with a flat, cold-rolled copper mesh via a 15min 400˚C anneal in forming gas, as shown in Figure 4.11(b).

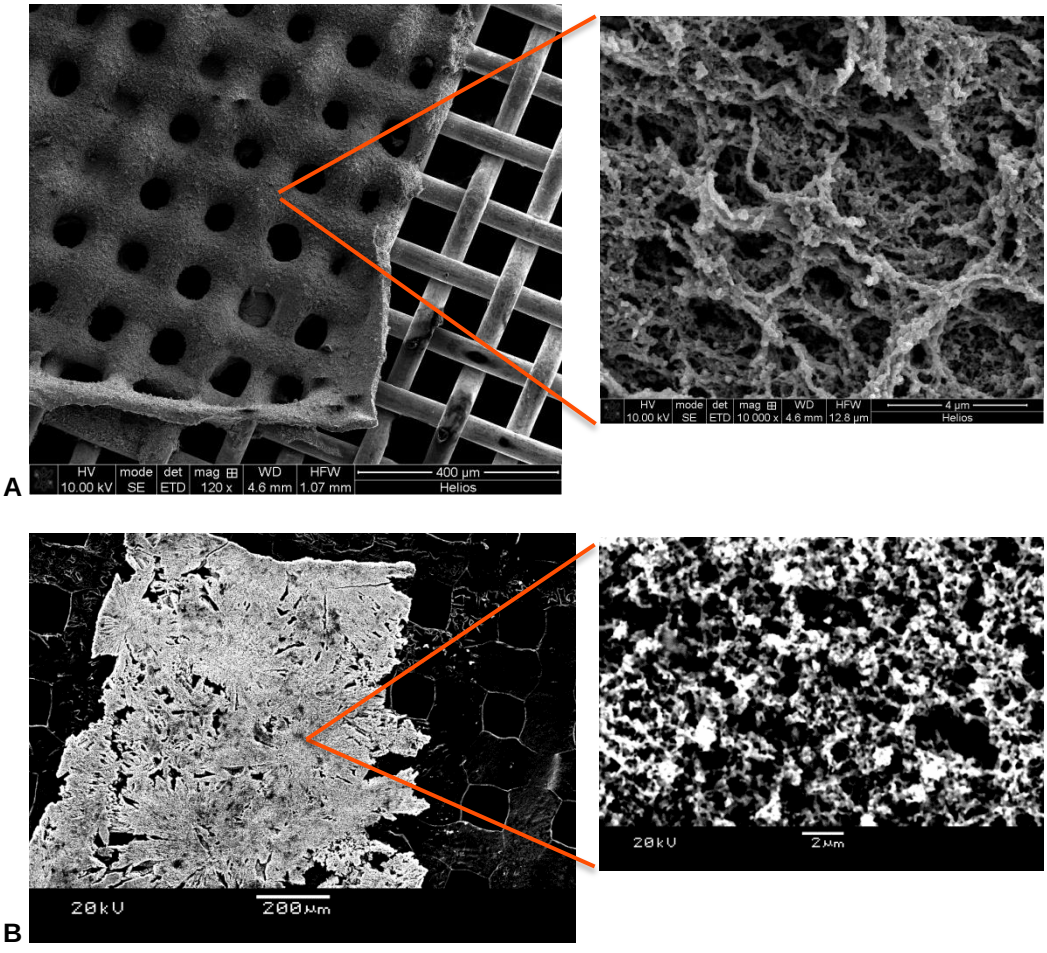

Figure 4.11. Virus-templated copper nanowire network integrated with woven copper mesh. A) Copper nanowires grown directly on commercially available copper mesh. B) Copper nanowire film heat-fused to flattened copper mesh.

4.2.8. Nanostructure Processing

Virus-assembled nanowire networks can be further processed to yield interesting nanostructures. Figure 4.12 shows a copper nanowire network after 5.5h immersion in 0.2M titanium(IV) chloride ($TiCl_4$) at 50ºC. TiO_2 crystallized on the nanowire network while maintaining high network porosity and structural integrity of the underlying metal framework. Additionally, the formation of copper nanocubes along the nanowires was observed. We expect that virus-assembled metallic nanowires can be processed and coated with a variety of other materials to create a conductive network with high surface functionality.

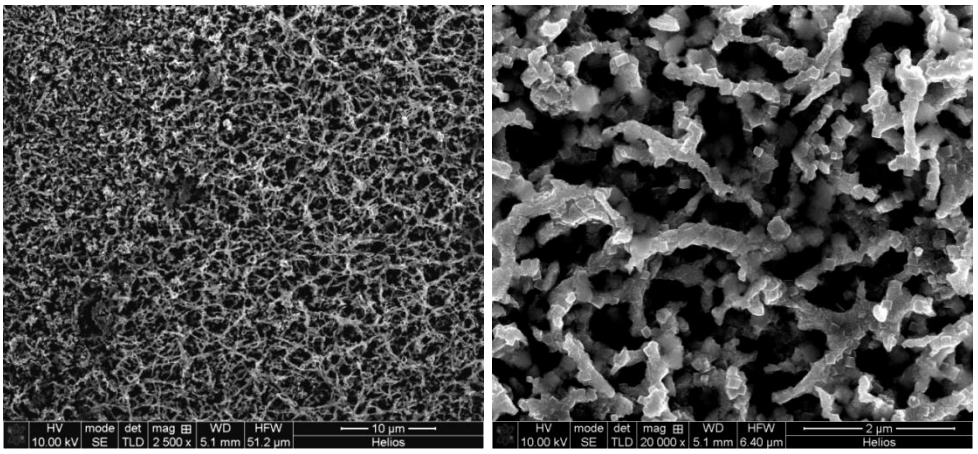

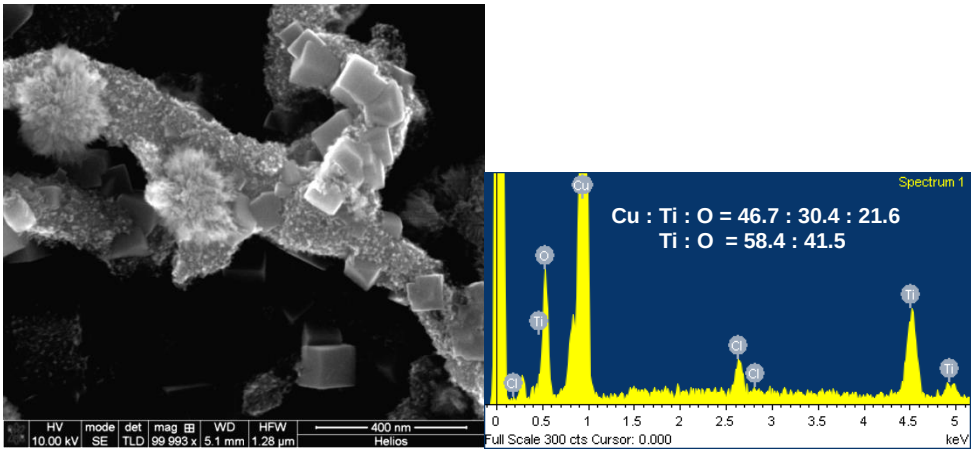

Figure 4.12. Scanning electron microscopy (SEM) images and energy dispersive x-ray (EDX) spectrum of virus-assembled copper nanowire network after 5.5h in 0.2M $TiCl_4$ at 50ºC.

4.2.9. Battery Electrode Fabrication and Characterization

Copper nanowire films were galvanically converted to tin to create lithium rechargeable battery anodes. A low pH tin immersion solution was modified from work by Zhao *et al.*,[20] consisting of 0.129M tin (II) methansulfonate, 0.756M sodium hypophosphite monohydrate, 1.05M thiourea (Tu), and 0.789M methane sulfonic acid. Copper nanowire films were immersed for 5, 10, 15, 30, and 45min and rinsed for 30min distilled water then dried with nitrogen gas.

While tin possesses a lower reduction potential than copper and should not facilitate a galvanic displacement, low pH solutions with complexants to stabilize copper ions have been demonstrated to plate tin on copper substrates.[21 22 23] The complexation of the resulting copper ions with thiourea (Tu) to form $[CuTu_4]^+$ makes the displacement reaction thermodynamically favorable. Tin electrodeposition and immersion coatings can result not only in a surface layer of tin, but also intermetallic compounds such as Cu_6Sn_5 at the copper-tin interface.[24]

To determine the effect of material composition and nanowire morphology on electrode performance, copper nanowire films exposed to the tin immersion solution for 10, 15, and 30min were assembled into coin cells. Copper-tin electrodes were dried in a vacuum chamber for 6h before test cell assembly in an argon glove box. Lithium foil was used as the counter electrode in the coin cell. The electrolyte comprised 1M $LiPF_6$ in ethylene carbonate and dimethyl carbonate in a 1:1 ratio with the electrolyte with polypropylene separators. A rate of C/10 (discharging the theoretical capacity per gram of electrode active material in 10h) was used with a theoretical capacity of 800mAh/g. The mass of active material was determined from averaged compositional energy dispersive X-ray analysis. Resulting cell capacities were normalized to the electrode area with units of $mAh/cm^2_{electrode}$. Electrode area was estimated from microscope images.

The capacity is plotted versus cycle number in Figure 4.13. The 10min sample is observed to have a stable capacity of $0.36mAh/cm^2_{electrode}$ through 65 cycles. The 15min sample maintains a higher capacity than the other samples to 20 cycles and then rapidly degrades with further cycling. The 30min sample shows a steady capacity fade until battery failure at the 23^{rd} cycle. A 5min sample (not shown) also exhibited capacity fade from over $1mAh/cm^2_{electrode}$ to under $0.5mAh/cm^2_{electrode}$ after 50 cycles. These results suggest that electrode cycle life is dependent on the nanowire material phase composition and morphology with a smaller degree of displacement favoring longer cycle life.

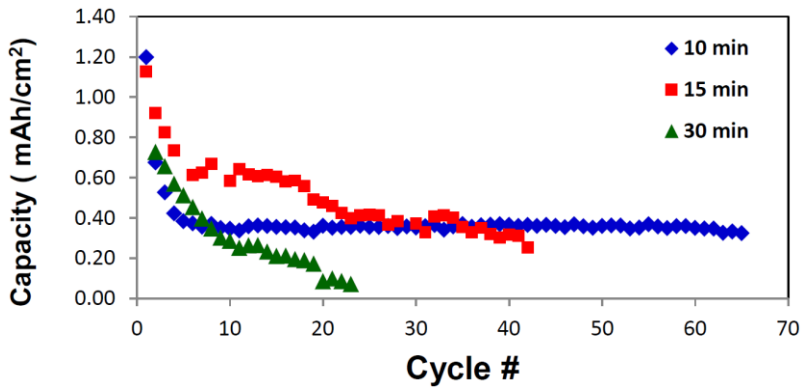

Figure 4.13. Galvanostatic testing of copper-tin electrodes. Capacity (mAh/cm^2) vs. cycle # at a rate of C/10 for a copper nanowire film exposed to tin immersion solution for 10, 15, and 30min.

4.3. Conclusion

Crosslinking viruses in solution into robust porous networks represents a promising flexible and scalable method to assemble 3D structures from genetically tunable 1D particles without the addition of polymers or other binders. We demonstrated the potential of this approach by creating virus aerogels of various microstructures via controlled drying, depositing copper and titanium oxide to functionalize the 3D biotemplate, and testing a copper-tin functionalized 3D virus nanowire network as a battery electrode.

The 3D virus nanowire network exhibited stable capacity performance using only solution-based chemistry to synthesize redox active material. No additional processing steps such a thermal annealing was performed, making this synthesis route a potentially inexpensive means to achieve a high capacity anode materials. Furthermore, no additional conductive materials or organic binders were used to assemble the electrodes. The copper-tin electrodes can be made as free standing films and represent a significant advance in the direction of lightweight electrode materials. Performance improvements are likely by coating 3D nanowire networks with high capacity materials such as silicon.

4.4. References

[1] Kumar, V., & Michael, N. (2012). Opportunities and challenges with autonomous micro aerial vehicles. *The International Journal of Robotics Research*, *31*(11), 1279-1291.

[2] Mor, G. K., Varghese, O. K., Paulose, M., Shankar, K., & Grimes, C. A. (2006). A review on highly ordered, vertically oriented TiO< sub> 2</sub> nanotube arrays: Fabrication, material properties, and solar energy applications. *Solar Energy Materials and Solar Cells*, *90*(14), 2011-2075.

[3] Liu, H., Song, C., Zhang, L., Zhang, J., Wang, H., & Wilkinson, D. P. (2006). A review of anode catalysis in the direct methanol fuel cell. *Journal of Power Sources*, *155*(2), 95-110.

[4] Vidotti, M., & Torresi, S. I. (2008). Nanochromics: old materials, new structures and architectures for high performance devices. *J. Braz. Chem. Soc*, *19*(7), 1248-1257.

[5] Arico, A. S., Bruce, P., Scrosati, B., Tarascon, J. M., & Van Schalkwijk, W. (2005). Nanostructured materials for advanced energy conversion and storage devices. *Nature materials*, *4*(5), 366-377.

[6] Seker, E., Berdichevsky, Y., Begley, M. R., Reed, M. L., Staley, K. J., & Yarmush, M. L. (2010). The fabrication of low-impedance nanoporous gold multiple-electrode arrays for neural electrophysiology studies. *Nanotechnology*,*21*(12), 125504.

[7] Li, H., & Misra, A. (2010). A dramatic increase in the strength of a nanoporous Pt–Ni alloy induced by annealing. *Scripta Materialia*, *63*(12), 1169-1172.

[8] Gu, Z., Ye, H., Bernfeld, A., Livi, K. J., & Gracias, D. H. (2007). Three-dimensional electrically interconnected nanowire networks formed by diffusion bonding. *Langmuir*, *23*(3), 979-982.

[9] Yuan, M., Lu, Y., Tian, B., Yang, H., Tu, B., Kong, J., & Zhao, D. (2004). Preparation and enhanced electrochromic property of three-dimensional ordered mesostructured mixed tungsten-titanium oxides. *Chemistry Letters*, *33*(10), 1396-1397.

[10] Hong, B. H., Bae, S. C., Lee, C. W., Jeong, S., & Kim, K. S. (2001). Ultrathin single-crystalline silver nanowire arrays formed in an ambient solution phase.*Science*, *294*(5541), 348-351.

[11] Romo-Herrera, J. M., Terrones, M., Terrones, H., Dag, S., & Meunier, V. (2007). Covalent 2D and 3D networks from 1D nanostructures: designing new materials. *Nano letters*, *7*(3), 570-576.

[12] Burpo, F. J., Lew, B., Liau, F. W., & Belcher, A. M. (2012). 3-Dimensional Phage-Templated Nanowire Networks for Lithium Rechargeable Batteries. *Submitted to Nature Materials.*

[13] Mao, J. Y., Belcher, A. M., & Van Vliet, K. J. (2009). Genetically engineered phage fibers and coatings for antibacterial applications. *Advanced Functional Materials, 20*(2), 209-214.

[14] Lee, S. W., & Belcher, A. M. (2004). Virus-based fabrication of micro-and nanofibers using electrospinning. *Nano letters*, *4*(3), 387-390.

[15] Scanlon, S., Aggeli, A., Boden, N., Koopmans, R., Brydson, R., & Rayner, C. M. (2007). Peptide aerogels comprising self-assembling nanofibrils. *Micro & Nano Letters, IET*, *2*(2), 24-29.

[16] Lee, I., Hammond, P. T., & Rubner, M. F. (2003). Selective electroless nickel plating of particle arrays on polyelectrolyte multilayers. *Chemistry of materials,15*(24), 4583-4589.

[17] Barker, B. D. (1981). Electroless deposition of metals. *Surface Technology,12*(1), 77-88.

[18] Balci, S., Bittner, A. M., Hahn, K., Scheu, C., Knez, M., Kadri, A., ... & Kern, K. (2006). Copper nanowires within the central channel of tobacco mosaic virus particles. *Electrochimica acta*, *51*(28), 6251-6257.

[19] Blanco, P., Kriegs, H., Lettinga, M. P., Holmqvist, P., & Wiegand, S. (2011). Thermal diffusion of a stiff rod-like mutant y21m fd-virus. *Biomacromolecules,12*(5), 1602-1609.

[20] Zhao, J., Li, N., Cui, G., & Zhao, J. (2006). Study on immersion tin process by electrochemical methods and molecular orbital theory. *Journal of The Electrochemical Society*, *153*(12), C848-C853.

[21] Huttunen-Saarivirta, E. (2002). Observations on the uniformity of immersion tin coatings on copper. *Surface and Coatings Technology*, *160*(2), 288-294.

[22] Molenaar, A., & Coumans, J. J. C. (1982). Autocatalytic tin deposition. *Surface Technology*, *16*(3), 265-275.

[23] Zhao, J., Li, N., Cui, G., & Zhao, J. (2006). Study on immersion tin process by electrochemical methods and molecular orbital theory. *Journal of The Electrochemical Society*, *153*(12), C848-C853.

[24] Tamura, N., Ohshita, R., Fujimoto, M., Fujitani, S., Kamino, M., & Yonezu, I. (2002). Study on the anode behavior of Sn and Sn–Cu alloy thin-film electrodes.*Journal of power sources*, *107*(1), 48-55. Tamura, N. et al. Study on the anode behavior of Sn and Sn-Cu alloy thin-film electrodes. Journal of Power Sources 107, 48-55 (2002).

Chapter 5: Mechanical Characterization of Virus 3D Networks

5. Mechanical Characterization of Virus 3D Networks

5.1. Introduction

To investigate virus-assembled nanowire networks for lightweight batteries with minimal packaging (i.e. having the active battery materials provide structural support), we evaluated the mechanical properties of virus-assembled metallic nanowire networks in comparison with common structural materials as well as other 3D virus networks. Arrangement of viruses via covalent crosslinking into stable hydrogels was described in Chapter 4. The hydrogels can subsequently be controllably dried into aerogels or mineralized into metal porous nanowire networks. Furthermore, genetically modified M13 virus can bind single wall carbon nanotubes (CNT) before gelation to create a composite CNT-biotemplate. Given the novel series of related materials, the purpose of this chapter is to determine 1) the optimal nanoindentation conditions and analysis model for each sample type, and 2) the elastic modulus of virus-based hydrogels, aerogels and metal nanowire networks to initially characterize the mechanical robustness of these materials for processability and device integration. Abundant theory and methodology is described in this chapter because the interpretation of nanomechanical testing results is dependent on the choice of testing conditions, mechanical models, and assumptions. Collaborators in this chapter include Dr. John Burpo, Ling Li, and Derek Smith. Portions of this chapter are reprinted from our research report.[1]

5.1.1. Nanoindentation Models

Mechanical testing was performed in two ways: Atomic force microscope force spectroscopy and instrumented nanoindentation. An Asylum Research MFP 3D was used

to perform force spectroscopy on all samples other than the nickel nanowire thin film networks. A silicon nitride cantilever with a Novascan 20μm borosilicate glass sphere (k_{nom}= 0.03N/m) was used to indent hydrogel samples. An Asylum AC160TS cantilever, k_{nom}= 42N/m, tip radius = 9nm, was used to indent the virus-SWCNT aerogel. A Veeco/Bruker DNISP diamond probe, k = 314N/m, tip radius = 40nm, was used to indent copper and thick nickel samples.

Instrumented nanoindentation was conducted on nickel nanowire thin film networks in ambient conditions using a Hysitron Triboindenter. Load-controlled nanoindentations were performed using a 10μm diamond conical indenter. The maximum loads were set to be 50 and 100μN and the loading and unloading rate was kept constant at 10μN/s. To investigate the time-independent mechanical properties, the unloading rate was varied using 5, 10, and 20μN/s. Twenty five experiments per setting were performed in a square grid arrangement with each indent spaced 60μm apart. The probe tip area function, $A_c(h_c)$, was fitted with a sixth order polynomial using the known properties of fused silica. The frame compliance of the instrument was calibrated separately using the indentation data of fused silica with a Berkovich indentation probe.

The Oliver-Pharr (O-P) method was first used to approximate the mechanical properties from nanoindentation data.[2] In this methodology, the contact stiffness *S* is first obtained from the elastic unloading curve: $S = dP/dh$. Then the contact depth h_c was determined by: $h_c = h_{max} - h_{sink\text{-}in}$. Where $h_{sink\text{-}in}$ is the amount of sink-in depth, as shown in Figure 5.1. By using Sneddon's force-displacement relationship, we have $h_{sink\text{-}in} = \varepsilon \cdot P_{max}/S$, where the geometrical constant ε is 0.75 for the paraboloid of revolution used in this work. The projected contact area is then calculated using h_c and the pre-calibrated

area function, $A_c(h_c)$. Finally, the hardness *H* and indentation modulus E_r can be calculated using the following equations:

Equation 1

$$H = \frac{P_{max}}{A_c h_c}$$

Equation 2

$$E_r = \frac{1}{\beta}\frac{\sqrt{\pi}}{2\sqrt{A_c h_c}}S$$

where β is a correction factor that depends on indenter shape (1 for axisymmetric indenters).

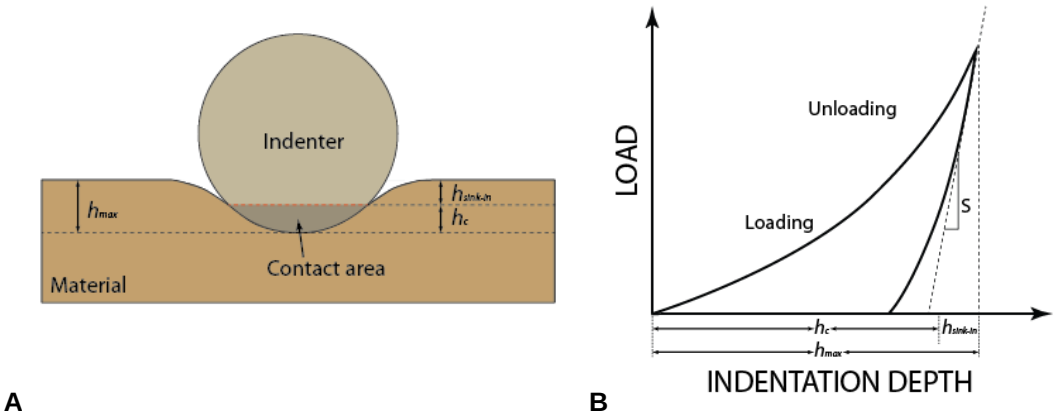

Figure 5.1. Nanoindentation concepts. A) Geometric approximation used to estimate contact area. B) Generalized indentation curve for indentation experiments.

Several variations of the John-Kendall-Roberts (JKR) method were used to determine the modulus for the aerogel and hydrogel samples. This model generally modifies the Hertz model with the addition of prefactors that take into account the adhesion between the tip and sample surface. The model relies on the assumption that the probe radius is large compared to the indentation depth, and that the adhesion is sufficiently high between the probe and sample surface.

Two similar models for the elastic modulus of adhesive samples were developed by Carillo and Gupta. In these, *S* (contact stiffness) is determined in the same manner as the Oliver-Pharr method described above. *R* is the radius of the probe used, *P* is the maximum load applied to the sample, ν_s is Poisson's ratio, and F_{po} is the force required to pull the tip off of the sample surface. The equations for the reduced elastic modulus for Carillo[3] (Equation 3) and Gupta[4] (Equation 4) are shown here.

Equation 3

$$E_S^{JKR} = \sqrt{\frac{S^3(1-\nu_S^2)^2}{6R}\frac{1}{\left(P + 2F_{po}^{JKR} + 2F_{po}^{JKR}\sqrt{(\frac{P}{F_{po}^{JKR}}+1)}\right)}}$$

Equation 4

$$E_{JKR} = \sqrt{\frac{S^3(1-\nu_S^2)^2}{6R}\left(\frac{2}{3\sqrt{1+\frac{P}{F_{po}}}}+1\right)^3\frac{1}{P + 2F_{po} + 2F_{po}\sqrt{(1+\frac{P}{F_{po}})}}}$$

Ebenstein compared various fitting models to account for adhesion.[5] The first model is a two point fit using δ_o and δ_{adh} determined from the force-indentation plot, where δ_o is the displacement at zero applied load and δ_{adh} is the displacement at the point of maximum adhesive force at pull-off. Using these two values in Equation 5 below for the Ebenstein 2-point model, the reduced modulus is determined. This less rigorous approach was then compared with an adhesion curve fit that involves determining the pull-off force, P_{adh}, and then fitting the range of data from P_{adh} to $-P_{adh}$ to Equation 6, the Ebenstein mid-fit model, for the reduced modulus. The fitted values are $\delta_{contact}$, a_o, and

P_{adh} allowing the calculation of the reduced modulus as $E_r = -3RP_{adh}/a_o^3$. Results with polydimethylsiloxane indicate that the 2-point and mid-fit models do not statistically differ in the determination of the reduced modulus.[5] JKR based calculations in this chapter will compare the Carillo, Gupta, Ebenstein 2-point, and Ebenstein mid-fit models.

Equation 5

$$E_r = \frac{-3P_{adh}}{\sqrt{R}}\left(\frac{3(\delta_0 - \delta_{adh})}{1 + 4^{-2/3}}\right)^{-3/2}$$

Equation 6

$$\delta - \delta_{contact} = \frac{a_0^2}{R}\left(\frac{1+\sqrt{1 - P/P_{adh}}}{2}\right)^{4/3} - \frac{2}{3}\frac{a_0^2}{R}\left(\frac{1+\sqrt{1 - P/P_{adh}}}{2}\right)^{1/3}$$

5.2. Experimental

5.2.1. Virus-Only and Virus Carbon Nanotube Hydrogels

Characteristic indentations for the E3 and DSPH-CNT hydrogels are shown in Figure 5.2 below. The DSPH-CNT hydrogels were prepared by incubating DSPH viruses with 20-fold stoichiometric excess of single-walled carbon nanotubes approximately 500nm in length and 0.8nm in diameter (see Appendix), and then crosslinking with glutaraldehyde. The saw tooth pattern seen in the retraction curve for E3 hydrogels is similar in form to the unfolding of proteins in single molecule tension tests. This saw tooth pattern was observed in all E3 hydrogel force-indentation curves and suggests that the hydrogel adhered to the 20μm borosilicate glass sphere successively detached gel domain regions of various sizes and adhesive forces. The DSPH-CNT gel characteristic

force-indentation plot, on the other hand, depicts a more distinct pull-off force compared to the E3 hydrogels. This pull-off force of the DSPH-CNT sample increased with successive indentations on the same location as seen in Figure 5.3. This increase in pull-off force may be due to increasing CNT and virus debris adhesion onto the borosilicate spherical probe.

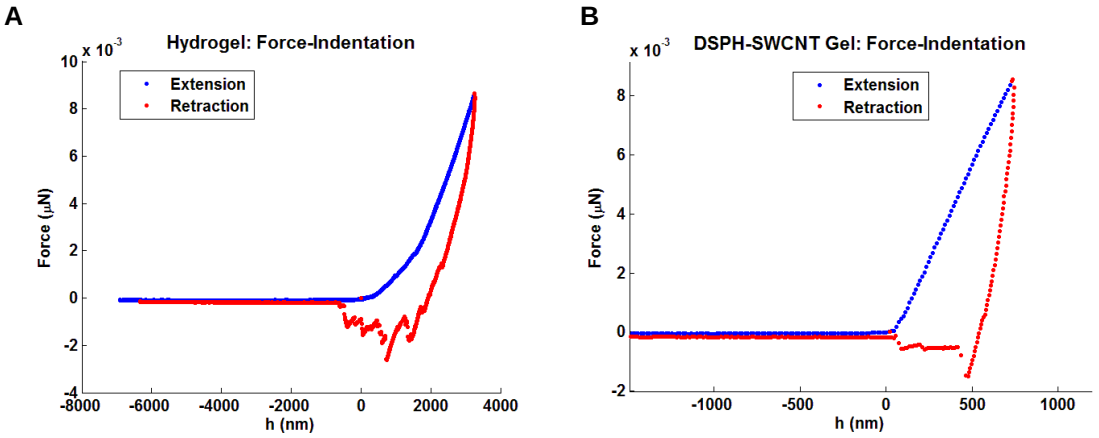

Figure 5.2. Representative hydrogel indentation curves. A) Representative E3 virus hydrogel force-indentation curve. B) Representative DSPH virus single-walled carbon nanotube (SWCNT) hydrogel force-indentation curve.

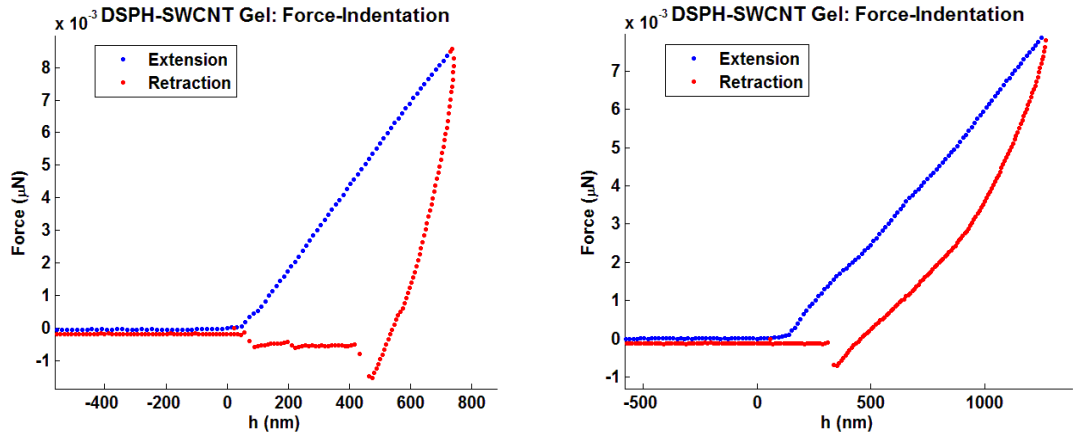

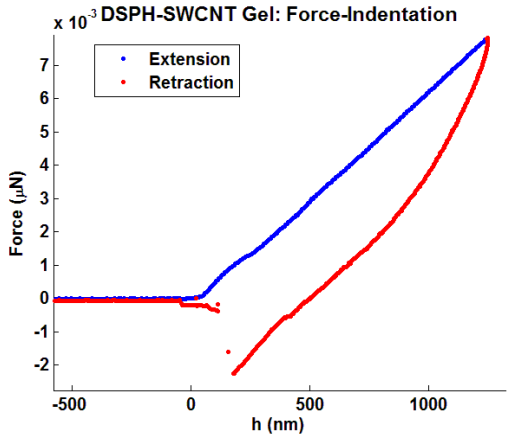

Figure 5.3. Sequential indentations on the DSPH virus single-walled carbon nanotube (SWCNT) hydrogel at the same location. From left to right and bottom: the first, second, and tenth sequential indentations. The pull-off force nearly doubles over the course of indentations.

The indentation modulus was calculated for all of the hydrogel experiments using the JKR method previously described. This model was chosen due to the high adhesion seen in the samples upon retraction of the tip, and the fact that the indentations were less than the radius of the chosen tip. Different variations of the basic JKR model were used to compare results between models to include the Ebenstein 2-point, Ebenstein mid-fit, Gupta and Carillo models. Figure 5.4 shows the results of the indentations for sequential indentations. As evident from the graph, there was little variation in the modulus with subsequent measurements for the E3 hydrogel film. However, there was noticeable variation in the modulus estimates between models, although all models yield values on the same order of magnitude. The Gupta model appears to give the highest estimate on average, while the mid-fit model gives the lowest estimate.

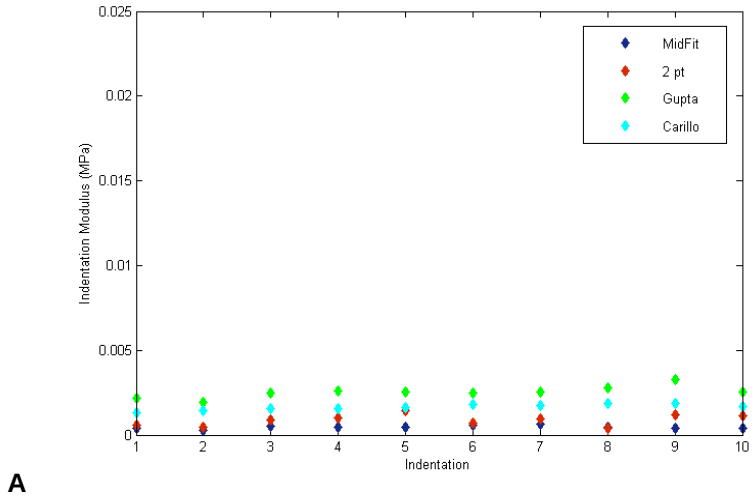

A

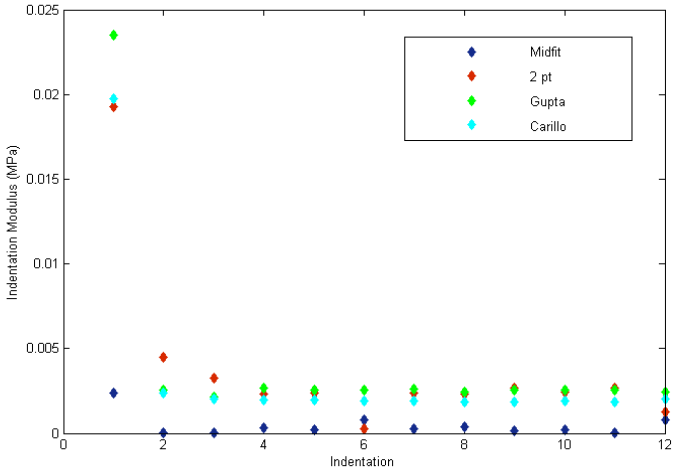

B

Figure 5.4. Hydrogel indentation modulus vs. indentation number. A) E3 virus hydrogel. B) DSPH virus single-walled carbon nanotube (SWCNT) hydrogel. Legend colors: Dark blue – Ebenstein Midfit. Red – Ebenstein 2-point. Green – Gupta. Light blue – Carillo.

Figure 5.4 indicates that there was no statistically significant variation between the E3 hydrogel samples and the latter indentations of the DSPH samples functionalized with carbon nanotubes in any of the models. This is contrary to our original hypothesis that the nanotubes would serve to create a stiffer hydrogel. While the initial modulus of the CNT functionalized hydrogels is quite a bit higher, this rapidly decreases after a single indentation. The reasons for this are not immediately apparent, and additional

investigation is needed to determine if the CNTs are being disrupted or moved within the sample. The reason for the similar values between the two might be justified based on the size difference between the virus used in the synthesis of the hydrogel, and the bound carbon nanotubes. The CNT's are roughly half the axial length of the virus. It may be that the CNT's are predominantly bound to the virus between junctions, meaning that there is little bridging of the crosslinks with the stiffer CNTs. Thus, the junction points likely have the same degrees of freedom in both samples. Another possible explanation is that the stiffening effect of the CNTs is balanced by a lower glutaraldehyde mediated crosslink density in the DSPH film. Further studies on the variation of crosslink density of these films are required to determine whether this is the case.

Table 5.1 shows the results of hydrogel moduli variation with sequential indentations and across the surface of the sample using the four JKR based models. The standard deviations are quite high, leading to the conclusion that the hydrogel stiffness varies across the film. This may result from film heterogeneities that resulted from jellification and subsequent sample handling. Although this particular hydrogel has not previously appeared in the literature, the modulus is within the 0.1-100kPa range given by Kloxin *et al.* for covalently linked hydrogels,[6] and only about an order of magnitude lower than the low end values found for gelatin, 20kPa.[7]

Table 5.1. Hydrogel moduli based on four JKR models

Sample		Model Modulus (kPa)			
		Mid Fit	**2-pt**	**Gupta**	**Carillo**
Sequential Indents					
	Hydrogel film	0.45 ± 0.10	0.87 ± 0.33	2.53 ± 0.3	1.64 ± 0.19
	DSPH-CNT Hydrogel	0.46 ± 0.67	3.81 ± 4.98	4.27 ± 6.06	3.45 ± 5.13
Variation Across Surface					
	Hydrogel film	0.29 ± 0.20	0.54 ± 0.50	1.43 ± 0.75	0.51 ± 0.33

These results provide an initial starting point in characterizing virus based hydrogels. The gels used in this study were formed from a single virus concentration of 1×10^{14} viruses/mL. The variation of mechanical properties of hydrogels formed from different starting concentrations would be of interest, particularly in determining how robust hydrogels are to scaled-up processing steps. Furthermore, different mechanical properties of the DSPH-CNT hydrogels may manifest with differing virus concentrations and virus-CNT ratios.

5.2.2. Virus Carbon Nanotube Aerogel

The DSPH-CNT aerogel force-indentation depth curve in Figure 5.5 displays adhesion behavior during retraction, and also has a slight saw tooth shape at pull-off, which is expected from an adhesive crosslinked chain network. The indentation was performed in air using an AC160TS probe tip at a velocity of 10μm/s. Using the same JKR models as for the hydrogel analysis, the Gupta model yielded the highest reduced modulus of $E_r = 442.62 \pm 120.27$MPa. One caveat of this analysis is that the probe tip diameter of 9nm was relatively small given the porous nature of the aerogel. In general, the JKR model calls for a large probe radius. Confirmation of these results with a large probe radius is necessary in future work.

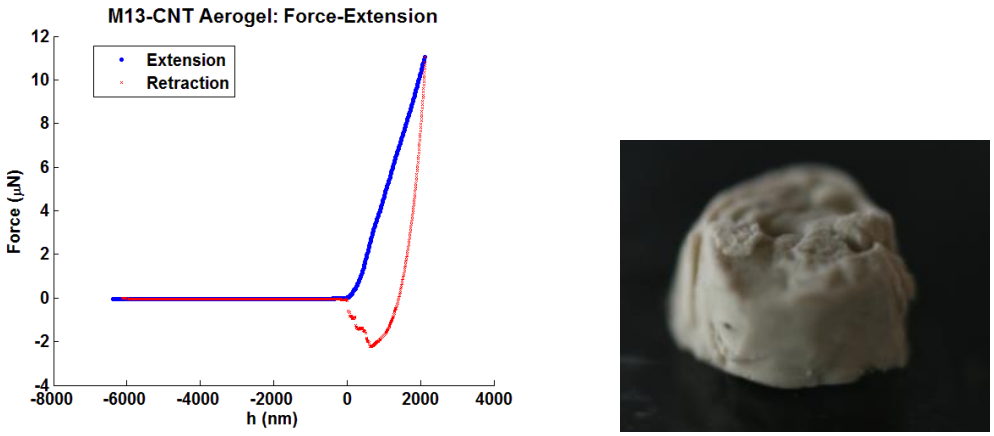

Figure 5.5. Representative virus-aerogel Force-Indentation curve (left). Photograph of virus aerogel with embedded single-walled carbon nanotube network, approximately 2mm wide (right).

Table 5.2. Virus carbon nanotube aerogel moduli based on four JKR models

Sample	Model Modulus (kPa)			
	Mid Fit	2-pt	Gupta	Carillo
Aerogel	148.68 ± 61.67	157.76 ± 65.41	442.62 ± 120.27	332.34 ± 97.18

5.2.3. Copper Nanowire Network

The copper nanowire network films were morphologically characterized using a scanning electron microscope (SEM). The representative force-indentation curve of copper nanowire films in Figure 5.6 indicates a nearly pure elastic response. Every indentation curve had the same curve shape (n=22). At the peak load force, a negative hysteresis is observed and this is regarded as an artifact. Based on the nearly 7μm indentation depth, the AFM z-piezo may have reached a non-linear region of its voltage response. Also, the copper force-indentation curves were manually truncated for the near vertical response when the probe reached the underlying silicon substrate. Based on the inorganic metal nature of the porous copper scaffold being commensurate with metal foam, a plastic component of the force-extension relationship was expected. Given that

the peak of the curve lies at the depth of the substrate, densification effects are also expected, but not evident.

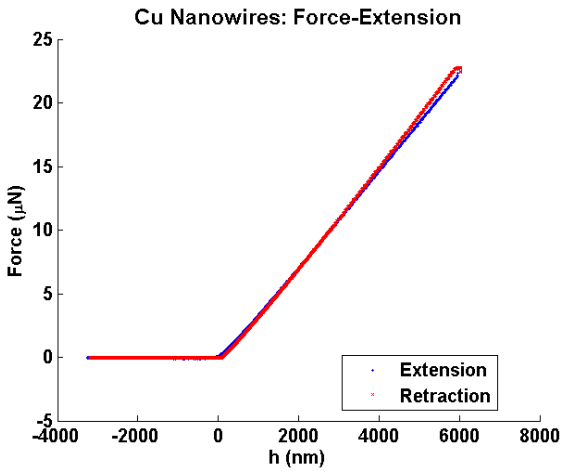

Figure 5.6. Representative copper nanowire network force-indentation curve showing nearly perfect elastic response.

A possible explanation for the elastic response of the copper nanowire network lies in the sample preparation. If the virus hydrogel did not completely mineralize, it is possible that the top layer of the network was mineralized, while the underlying gel network dried to a multi-micron thick elastic layer. This hypothesis is shown in the schematic in Figure 5.7. The cause of a differential layered film is likely due to mass transport of electroless deposition precursors being consumed at the outer gel layer before diffusing into the inner hydrogel layer proximal to the substrate. This layered structure would likely convolute the elasto-plastic response of the copper nanowires with the possible underlying virus organic layer. The Oliver-Pharr model was used to determine the copper nanowire film reduced modulus and hardness. These values are 1.24 ± 0.18MPa and 3.29 ± 0.98MPa respectively. These values are just below the range of elastic moduli for low density porous films.[8]

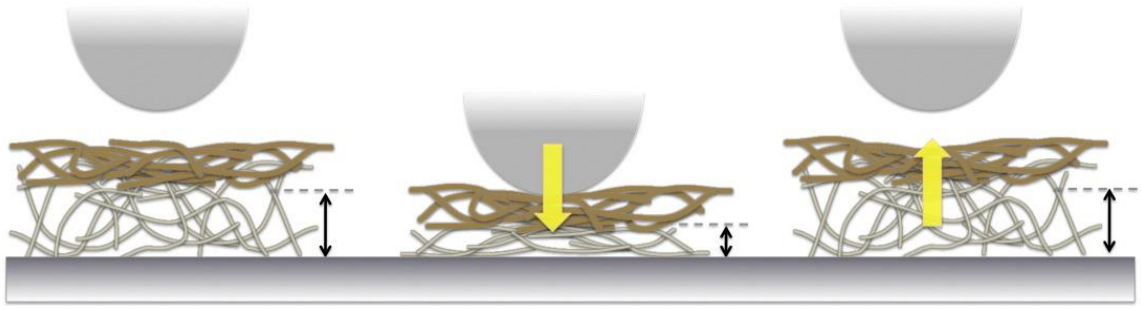

Figure 5.7. Possible mechanism for partially mineralized nanowire networks to exhibit completely elastic indentation behavior. Mineralized copper nanowires form the top layer of the film. Non-mineralized viruses form the highly flexible bottom level of the film closest to the substrate.

5.2.4. Nickel Nanowire Thick Film Network

A relatively thick nickel nanowire network was characterized with a scanning electron microscope as shown in Figure 5.8, revealing a 16.9μm thick contiguous network similar to that of the copper nanowires. The "thick" designation is in comparison to the 3μm "thin" films in the next section. See the Appendix for the protocol for producing nickel nanowires. The outer or top surface of the network has thicker nanowires, with the diameter decreasing as the underlying substrate is approached. The likely cause of this variable thickness morphology is due to the electroless deposition mass transport phenomenon previously discussed. The nickel film was indented with a diamond DNISP probe. The characteristic force indentation curve in Figure 5.9 depicts successive plastic fracture that appears to correspond to the differential nanowire diameter profile as seen in the SEM image in Figure 5.8. The force-indentation profile shows evidence of elastic, plastic and fracture load responses.

The fracture response of the nickel nanowires is seen in post-indentation SEM images in Figure 5.10. Little evidence is seen of plastic nanowire compaction within the

indentations. The Oliver-Pharr model was used to determine the sample reduced modulus and hardness. These values were 40.71 ± 6.41MPa and 9.15 ± 4.52MPa respectively. These values are at the low to mid- range of elastic moduli and hardness values for low density porous films.[8]

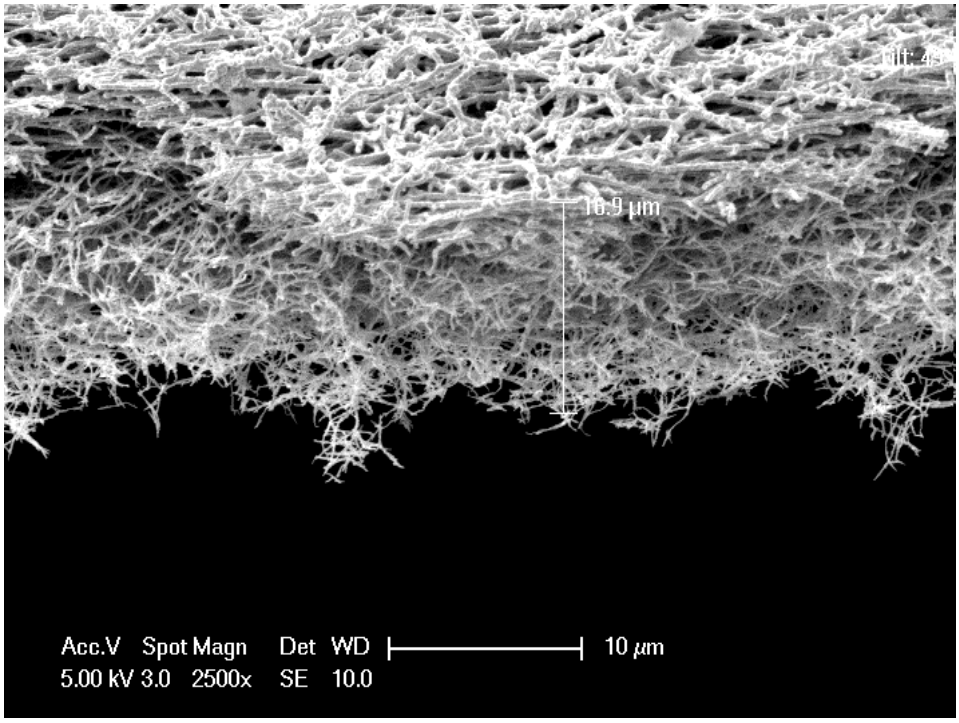

Figure 5.8. Scanning electron microscopy (SEM) cross section of nickel nanowire "thick" film. Vertical thickness bar is 16.9µm.

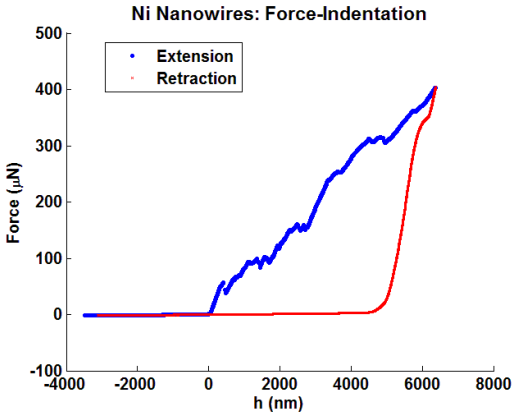

Figure 5.9. Representative "thick" nickel nanowire network force-indentation curve.

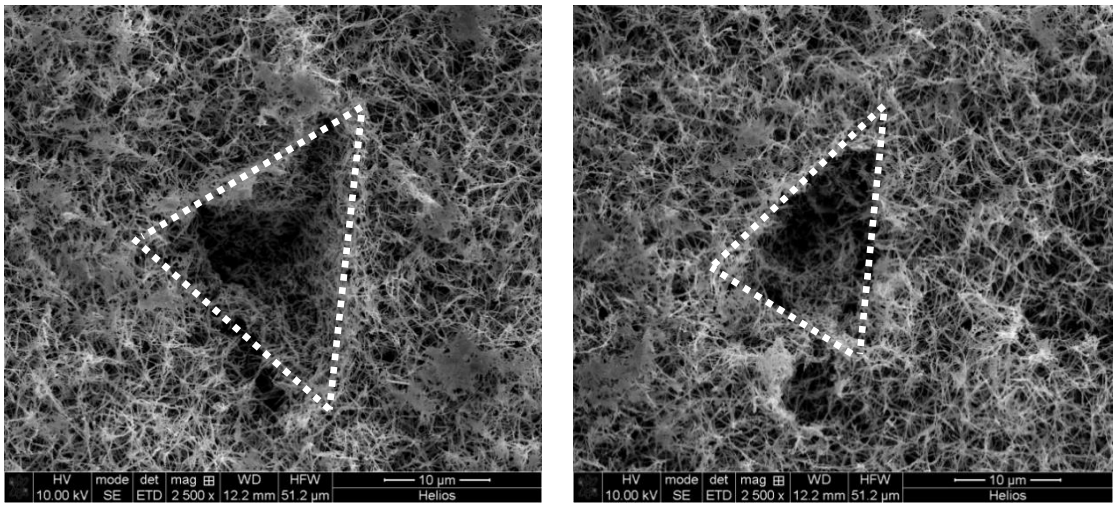

Figure 5.10. Scanning electron microscopy (SEM) view of DISPH diamond probe indentations into the nickel nanowire "thick" film. Scale bars are 10µm.

5.2.5. Nickel Nanowire Thin Film Network

Two nickel nanowire thin films (~3µm thick) were tested: One film immersed in a nickel electroless deposition bath for 14.5h and the other for 20.5h. As shown in Figure 5.11, the mineralized nanowires formed a crosslinked porous structure that resembles a nanoporous open cell foam structure. The mean diameter of the individual nanowires was 141nm, and the mean diameter of the open cells was 335nm based on the measurements using SEM images. The thin nickel nanowire film differs from the thick nanowire film in the previous section in the morphology of the nanowires themselves.

The nanowires in the thin film present a more rough and beaded appearance than those in the thick film. The difference likely results from the different ELD bath compositions and reduction times used for each batch. The film thickness of the two samples was approximately 3µm as determined by profilometry. The film thickness was

also measured using SEM observations of focused ion beam (FIB) milled cross-sections, as shown in Figure 5.11(b).

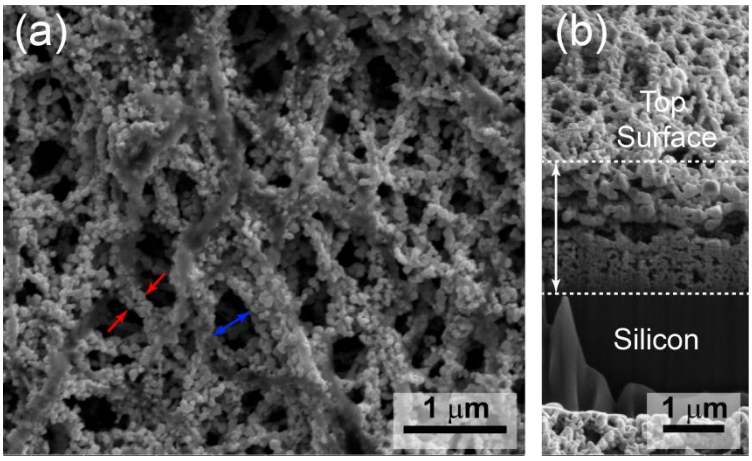

Figure 5.11. SEM image of thin nickel nanowire networks exposed to 14.5h of nickel electroless deposition. A) Top view. Red arrows indicate nanowire diameter, and blue arrows indicate pore diameter. B) Cross-sectional view.

Figure 5.12(a) shows seven overlapping representative individual nanoindentation curves for the 14.5h thin nickel film. Kinks on the loading curve (Figure 5.12(b)) suggest a collapse of the porous structure during the indentation process. Figure 5.13 shows the averaged load-depth curves of the 14.5h and 20.5h films corresponding to two maximum loads (n = 25 curves for each experiment condition). Although the initial portions of loading curves overlap with different maximum loads for both samples, there is a large spread among the individual curves, as indicated by the wide error bars in Figure 5.13. The maximum depth for all the experiments conducted is less than 1100nm, which corresponds to 37% of the total depth of the film. There is a slight change in slope for the loading portion at approximately 26nm, similar to the results of typical uniaxial compression tests of cellular materials.

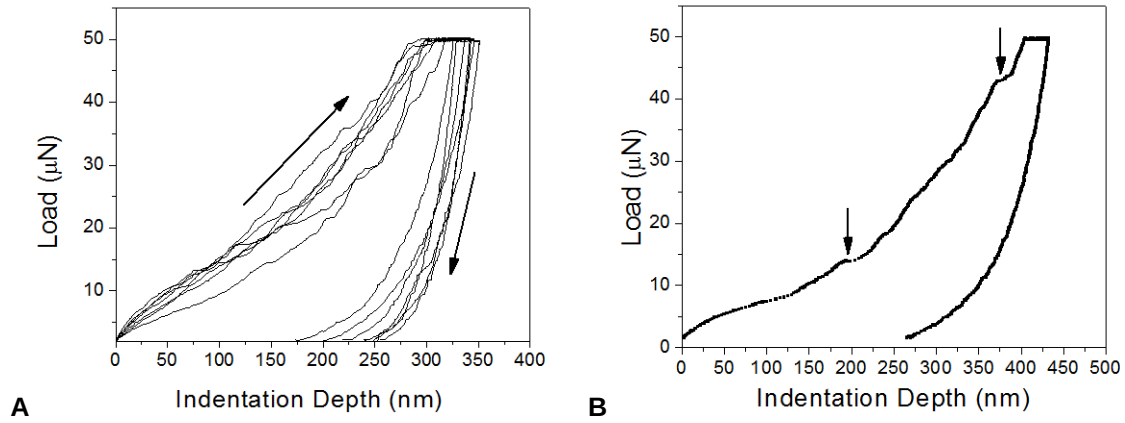

Figure 5.12. A): Nanoindentation curves obtained with the 14.5h nickel nanowire thin film networks using a 10μm diamond conical indenter. B) A single indentation curve showing kinks (marked by arrows) from collapse of porous structure.

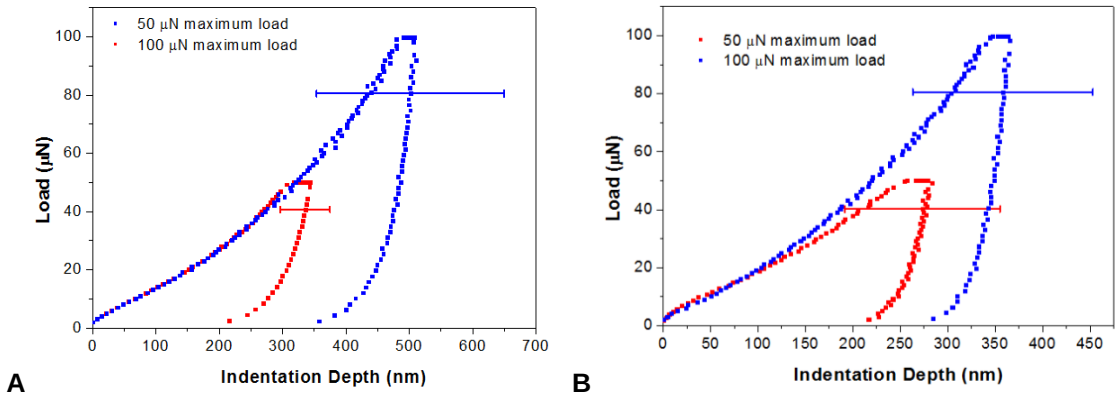

Figure 5.13. Averaged nanoindentation curves with error bars corresponding two maximum loads. A) 14.5h thin nickel film, and B) 20.5h thick nickel film. Red corresponds to a 50μN maximum load and blue to 100μN.

Using the standard Oliver-Pharr scheme as described, the as-calculated indentation modulus and hardness with a function of indentation depth is summarized in Figure 5.14. In this figure, both modulus and hardness first decrease with indentation depth, remain constant from 250-600nm, and then increase again when the maximum indentation depth is beyond 600nm. The indentation modulus and hardness within 250nm and 600nm indentation depth were 0.69 ± 0.48GPa and 13.18 ± 6.02MPa (14.5h film), and 0.79 ± 0.48GPa and 12.37 ± 5.29MPa (20.5h film), respectively.

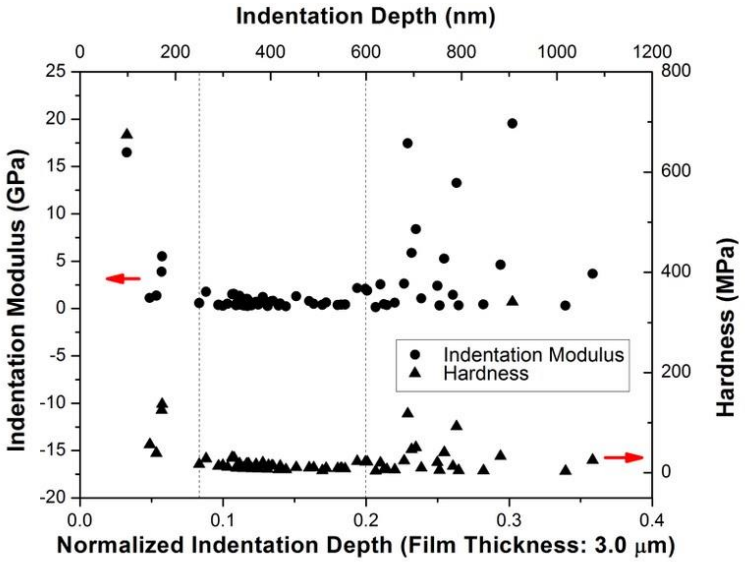

Figure 5.14. Indentation modulus and hardness as function of indentation depth for 14.5h thin nickel nanowire film.

Since the calculated modulus and hardness are strongly depth-dependent, a careful and complete interpretation of the data is critical. The first issue relates to the estimation of the contact area. SEM and FIB were used to accurately determine the indentation depth and remaining indent area, which reveal that the diameter of the remaining indent area is very close to the probe diameter. For example, a typical measurement reveals that the diameter of indent is 9.537μm, from which the indentation depth can be calculated as 1.21μm. The measured indentation depth was 1.13μm found by using FIB cross-sectioning. This measured value is very close to the difference between the calculated maximum indentation depth and the general elastic recovery of approximately 0.1μm. In this case, the contact depth is equal to the maximum indentation depth, h_{max}. This reasoning indicates that the contact area found using the standard Oliver-Pharr method is an underestimation, and hence both the modulus and hardness are overestimations.

Recently, it has been reported that nanoporous gold does not show elastic deformation adjacent to the indentation area, and that the contact depth h_c can be replaced by the maximum indentation depth h_{max}.[9] Using a new contact area model corresponding to our probe tip geometry, we obtained modulus *E* and hardness *H* estimates shown in Table 5.3 that are about 6-8% and 11-15% lower than those obtained from the standard Oliver-Pharr model.

Table 5.3. Modulus overestimation from standard Oliver-Pharr model due to different contact area approximation.

Nickel Film	-Δ*E*	-Δ*H*
14.5h	7.41%	14.24%
20.5h	6.00%	11.64%

We also considered the relative size between the contact area and average pore sizes of the film. As described above, the average diameter of the nanowires and open pores were 141 and 335nm, respectively. As shown in Figure 5.15, the nanowire network was simplified as a foam structure with square-shaped cells with the dimension of 476nm, the sum of the diameter of nanowires and size of pores. Using this scheme, the number of nanowires within the contact area during the indentation test increases with the indentation depth almost linearly. At the initial indentation contact, the number of nanowires under the indentation probe is limited and local deformation of individual nanowires might occur.

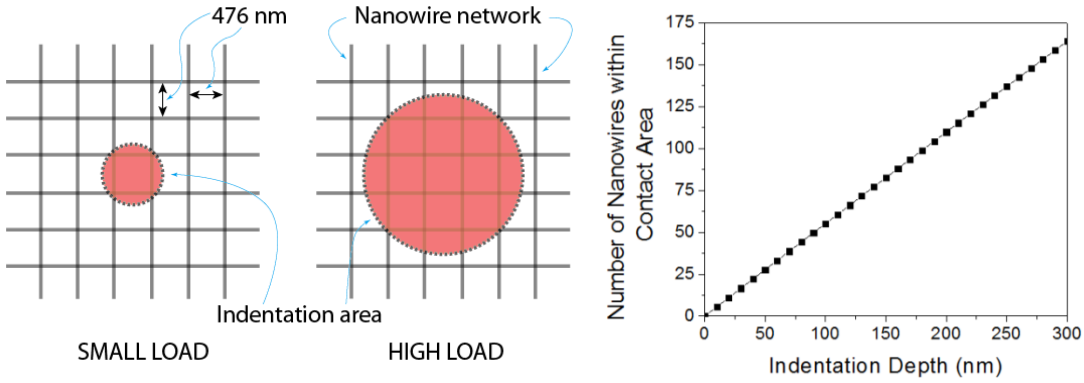

Figure 5.15. Indentation probe geometry comparison to nanowire network. A) Nanowire network simplified as square foam structure. B) Linear relationship between number of nanowires in contact and indentation depth.

Moreover, since the indenter first made contact with the sample surface with a set point load of 2μN in order to stabilize the piezo and monitor the drift, the indenter might just have been contacting several nanowires. In this case, it is possible to bend or fracture the nanowires during this stage since the load to require bend a single nickel nanowire is in the tens of μN range.[10] Therefore, at the initial loading stage, the indentation depth may not be very accurate, and it is also strongly dependent on the local distribution of nanowires because the film is not homogeneous at this scale.

For porous materials, both the elastic modulus and yield stress depend on the porosity. It was previously shown that the resistance to indentation increases with decreasing porosity.[11] Volinsky *et al.* found that both indentation modulus and hardness of porous low-k dielectric films increase with penetration depth as a result of densification of the material.[12] By using computation simulation and experiment results, Chen *et al.* also studied the effects of densification on the modulus and hardness.[13] These studies suggest that the indentation modulus and hardness calculated using the standard

Oliver-Pharr method cannot represent the intrinsic material properties of the original porous structure, because the material has densified.

The densification of these nanowire network films can be directly visualized by observing the indents using SEM. As shown in a typical top-view of the indent area in Figure 5.16, the deformation was localized under the indenter. In the magnified image, the pore size within the indentation area was greatly reduced, and in some cases, the pores were completely closed in the center of indentation area (arrow 1). In the area between the center and contact edge, the pores were reduced but not fully closed (arrow 2). In the area immediately beyond the indentation area, the pores had similar dimensions as compared to far-field pores (arrow 3). The structure adjacent the contact area was non-deformed, and no brittle fracture or crack emission was observed.

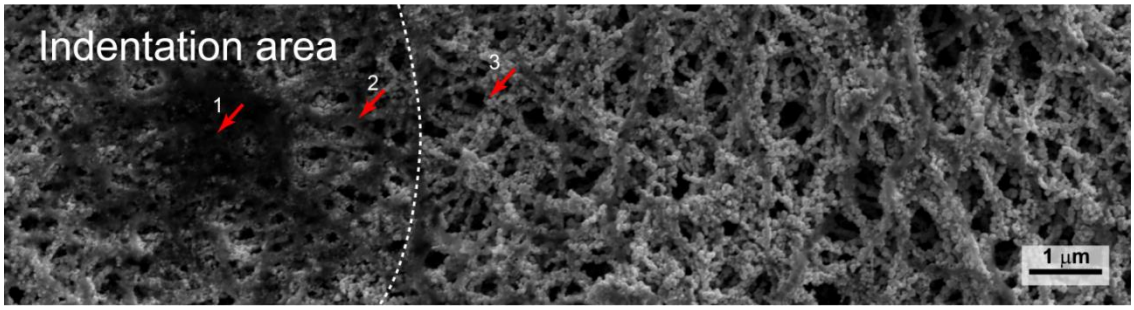

Figure 5.16. Densification of nickel nanowire networks. Indentation area marked by dotted line. 1) closed pores, 2) partially closed pores, and 3) open pores.

The densification beneath the surface was more clearly revealed by using FIB, as shown in a typical cross-section image of the indentation area seen in Figure 5.17. Under the indentation area, the pore dimensions and porosity were clearly reduced compared to the surrounding non-deformed area indicated by white arrows.

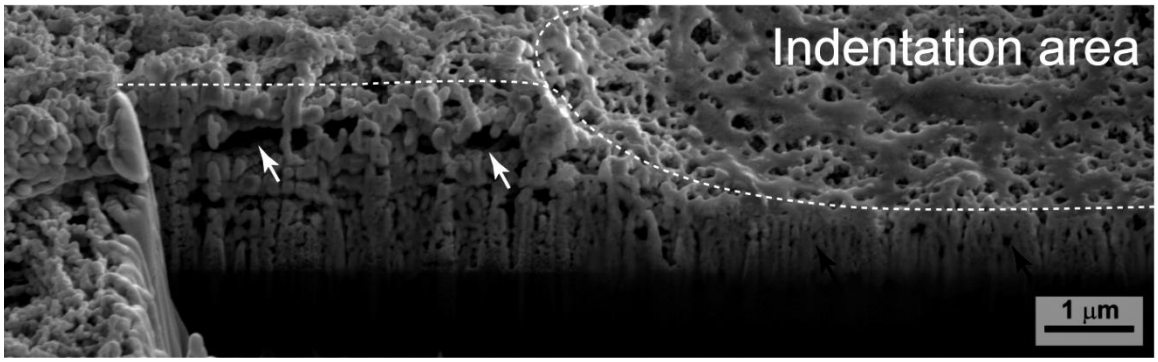

Figure 5.17. Focused ion beam (FIB) cross-section showing pore collapse profile at indentation area. The pore dimensions and porosity in the indentation area are clearly reduced compared to the surrounding non-deformed area indicated by white arrows.

Another issue of concern was the substrate effect. In order to avoid a substrate effect, it is known that generally indentations with maximum depths of less than 10-20% of the film thickness are required to obtain the intrinsic film properties (ASTM E384 – 10e2). However, the maximum depth for the thin nickel film measurements is about 35% of the total depth in order to obtain reliable data. Chen *et al.* performed a numerical study on the substrate effect of thin film for nanoindentation measurements.[13] According to the ratio of E_f/E_s and σ_f/σ_s (E_f and E_s are the moduli for the film and substrate, σ_f and σ_s are the yield stress for the film and substrate, respectively), the authors distinguished the cases between soft film on hard substrate and hard film on soft substrate. The Young's modulus and yield strength of silicon are 150 and 7GPa, respectively.[14] The yield stress of the film is related to the hardness from indentation measurement through: $H = c_b\sigma_f$, where c_b is a constraint factor that depends on the indenter shape and material properties.[13] A value of $c_b = 3$ is usually assumed for dense materials. However, it has been shown that the deformation of porous materials is not constrained by the surrounding material due to the densification beneath the indenter. In this case, the

indentation test is similar to a uniaxial test, and the yield stress equals to the hardness: $H = \sigma_f$.[9 15 16]

If we use the value of hardness in the indentation range of 250-600nm, the average yield strength was 13.18 ± 6.02MPa and 12.37 ± 5.29MPa for the 14.5h and 20.5h films, respectively. The Young's modulus is calculated using the following relation between the indentation modulus and Young's modulus: $E_r = E / (1-\nu^2)$. We assumed $\nu = 0$ as there is almost no lateral deformation upon indentation for this plastic deformation.

Using the values of E_f and σ_f obtained above, the ratios of E_f/E_s and σ_f/σ_s we obtained were 0.0047 and 0.0019, respectively. Therefore, this case of nanoporous film on silicon substrate falls into the soft film on hard substrate category. If we do not consider the densification effect (assuming the film is in dense form), the hardness measured is close to the true value of the film according to the numerical results reported by Chen *et al*.[17] The modulus estimate could not be judged since the ratios were out of the range of the simulation conditions in the report.

As discussed above, there are several issues that need to be considered when analyzing and reporting the data from this indentation experiment for the thin nickel nanowire network. These include estimation of contact area, initial statistical coverage of nanowires under the indentation probe, substrate effect, and densification. The relative influence of each mechanism with increasing indentation depth is summarized in Figure 5.18.

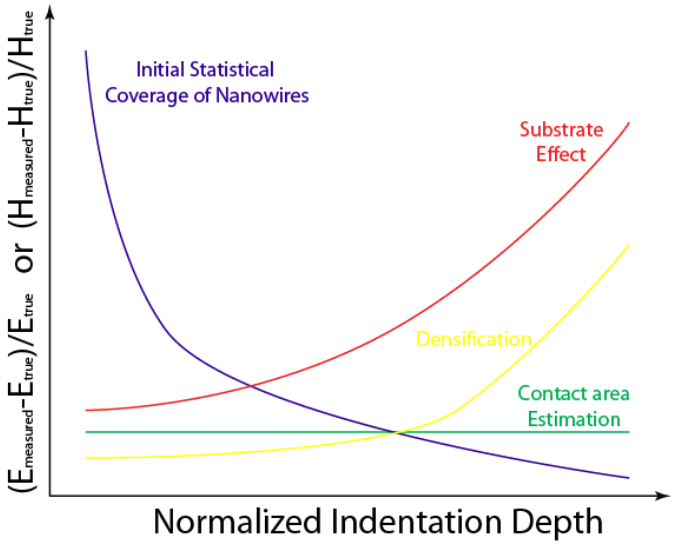

Figure 5.18. Relative influence of various effects on the measured mechanical properties as a function of indentation depth.

In this case, we know only the general trend for each effect and we are not be able to quantify the exact influence as a function of indentation depth, and therefore it is difficult to back-calculate the true materials properties from the current experimental results. In order to overcome this limitation, other mechanical testing (i.e. indentation with other indenter geometries and uniaxial compression) and relevant characterizations such as porosity measurement should be conducted, and the general mechanical constitutive law of the materials can be either established or adopted using other existing models. Then, by using computational simulation, the effects can be studied quantitatively. Fitting the experimental data will allow us to calculate the intrinsic material properties. Nevertheless, we can use the scaling law for open-cell foams to roughly test our estimations,

Equation 7

$$\sigma_p = C_1 \sigma_b \left(\frac{\rho_p}{\rho_b}\right)^n$$

where σ_b and ρ_b are respectively the yield strength and density of the bulk solid counterpart, and σ_p and ρ_p are respectively the yield strength and density of the porous film. Literature value of σ_b for nickel range from 278-930MPa.[18] [19] Using the higher end of this range, we estimated the relative porosity of the film to be 85%. This porosity estimate appeared consistent with the SEM images of the nickel films.

Figure 5.19 summarizes the indentation modulus and hardness the 14.5h and 20.5h nickel thin films using modified Oliver-Pharr method by modifying the contact area estimation with the scheme above. It can be seen that there is no statistical difference between the 14.5h and 20.5h films, despite the 6h difference in electroless deposition immersion time. This is not surprising as there was no significant morphological difference observed in SEM images between the two exposure times.

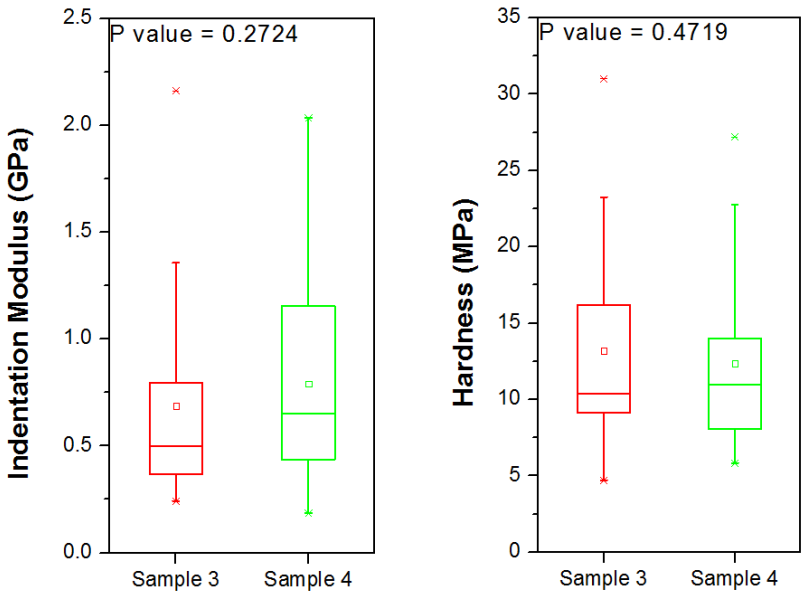

Figure 5.19. Statistical comparison of indentation modulus and hardness between thin nickel nanowire films. Sample 3 corresponds to 14.5h of electroless deposition immersion, and Sample 4 corresponds to 20.5h.

Lastly, the time-dependent mechanical response was studied, and the averaged indentation curves are summarized in

Figure 5.20. The curves do not overlap with one other for the loading portion due to non-uniformity in the film. The indentation modulus and hardness calculated using the standard Oliver-Pharr method did not show statistical significance among different unloading rates. No clear trend of these quantities with respect to the unloading rate was observed in the testing conditions.

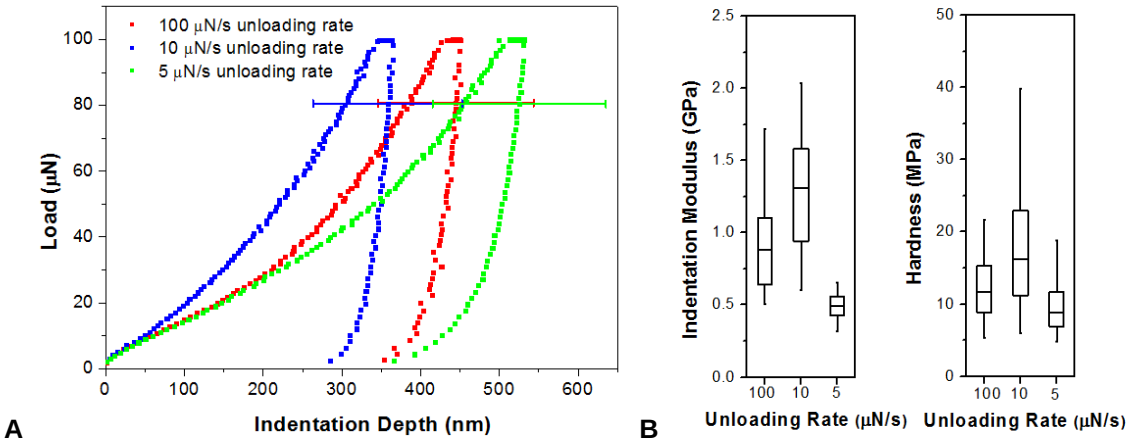

Figure 5.20. Effects of unloading rate on thin nickel nanowire film exposed to 20.5h of electroless deposition. A) Averaged indentation curves. Unloading rate colors correspond to: Red – 100μN/s, blue – 10μN/s, green – 5μN/s. B) Indentation modulus and hardness.

5.3. Conclusion

As summarized in Table 5.4, the virus-based hydrogels demonstrate elastic moduli at the low end of other polymer hydrogels such as poly(N,N-dimethylacrylamide) (PDMA), 2.8-89.5kPa;[20] PHEMA–co-EGDMA, 300kPa – 1.5MPa; and gelatin, 20kPa – 1MPa.[7] With a minimal volume decrease from the initial virus solution to resulting crosslinked hydrogel, there was ~99.7% water in the hydrogel. This water content is near

the upper range for hydrogels and the low observed elastic modulus is rationalized based on this parameter.[21]

Table 5.4. Comparison of mechanical properties of virus-assembled networks.

Sample	E_r (MPa)	H (MPa)	Probe	Medium	Tip Speed	Loading Rate	Model
E3 Hydrogel, Film	2.53±0.3	-	20μm sphere	Liquid	8 μm/s	-	JKR-Gupta
DSPH-CNT Hydrogel	4.27±6.06	-	20μm sphere	Liquid	8 μm/s	-	JKR-Gupta
DSPH-CNT Aerogel	442.62±120.27	-	AC160TS	Air	10 μm/s	-	JKR-Gupta
Copper Network	1.24±0.18	3.29±0.89	Diamond	Air	10 μm/s	-	O-P
Nickel "Thick" Film	40.71±6.41	9.15±4.52	Diamond	Air	10 μm/s	-	O-P
Nickel "Thin" Film, 14.5h	641.98±461.95	11.32±5.34	10μm conical	Air	-	10μN/s	Modified O-P
Nickel "Thin" Film, 20.5h	748.27±456.63	10.94±4.75	10 μm conical	Air	-	10μN/s	Modified O-P

Note: Tested samples and corresponding material parameters and testing conditions. JKR values correspond to the model with the highest moduli.

The copper and nickel nanowire networks formed open pore systems that are structurally and mechanically similar to open cell metal foams. Commercially available metal foams have elastic moduli that range from 20MPa to 10GPa.[8] The nickel nanowire assemblies tested had elastic moduli at the low to mid-range of commercial foams. The elastic modulus of the copper nanowire sample were an order of magnitude less than the lower range of commercial foams and at the upper range for hydrogels, resulting from possibly incomplete mineralization of the hydrogel. Based on these results, the two primary objectives of the mechanical evaluation have been met: 1) identifying

appropriate sample indentation conditions and analysis models for each sample type, and 2) initially characterizing the elastic moduli of virus-based porous hydrogel, aerogel, and inorganic nanowire samples.

Given the breadth of samples tested and indentation conditions optimized, the moduli values represent an initial material characterization. These initial results indicate that virus-based 3D materials are mechanically robust and suitable for further materials development and device integration. Further investigation of each sample type should examine creep compliance, stress relaxation, and oscillatory load testing. In particular, the hydrogels should be tested for a viscoelastic response, the virus CNT aerogels should be tested with various amounts of CNT loading, and the copper nanowire network should be tested with more even distribution of nanowire diameters.

5.4. References

[1] Burpo, F. J., Li, L., Liau, F., & Smith, D. (2011). Mechanical Properties of Virus Based 3-Dimensional Gels, Aerogels, and Metal Scaffolds. *Submitted to Course 3.901 at the Massachusetts Institute of Technology.*

[2] Oliver, W. C., & Pharr, G. M. (1992). Improved technique for determining hardness and elastic modulus using load and displacement sensing indentation experiments. *Journal of materials research, 7*(6), 1564-1583.

[3] Carrillo, F., Gupta, S., Balooch, M., Marshall, S. J., Marshall, G. W., Pruitt, L., & Puttlitz, C. M. (2005). Nanoindentation of polydimethylsiloxane elastomers: Effect of crosslinking, work of adhesion, and fluid environment on elastic modulus. *Journal of materials research, 20*(10), 2820-2830.

[4] Gupta, S., Carrillo, F., Li, C., Pruitt, L., & Puttlitz, C. (2007). Adhesive forces significantly affect elastic modulus determination of soft polymeric materials in nanoindentation. *Materials Letters, 61*(2), 448-451.

[5] Ebenstein, D. M. (2011). Nano-JKR force curve method overcomes challenges of surface detection and adhesion for nanoindentation of a compliant polymer in air and water. *Journal of Materials Research, 26*(08), 1026-1035.

[6] Kloxin, A. M., Kloxin, C. J., Bowman, C. N., & Anseth, K. S. (2010). Mechanical properties of cellularly responsive hydrogels and their experimental determination. *Advanced Materials, 22*(31), 3484-3494.

[7] Domke, J., & Radmacher, M. (1998). Measuring the elastic properties of thin polymer films with the atomic force microscope. *Langmuir, 14*(12), 3320-3325.

[8] Ashby, M. F., Evans, T., Fleck, N. A., Hutchinson, J. W., Wadley, H. N. G., & Gibson, L. J. (2000). *Metal Foams: A Design Guide: A Design Guide*. Butterworth-Heinemann.

[9] Biener, J., Hodge, A. M., Hamza, A. V., Hsiung, L. M., & Satcher, J. H. (2005). Nanoporous Au: A high yield strength material. *Journal of applied physics,97*(2), 024301-024301.

[10] Celik, E., Guven, I., & Madenci, E. (2011). Mechanical characterization of nickel nanowires by using a customized atomic force microscope.*Nanotechnology, 22*(15), 155702.

[11] Fleck, N. A., Otoyo, H., & Needleman, A. (1992). Indentation of porous solids.*International journal of solids and structures, 29*(13), 1613-1636.

[12] Volinsky, A. A., Vella, J. B., & Gerberich, W. W. (2003). Fracture toughness, adhesion and mechanical properties of low-< i> K</i> dielectric thin films measured by nanoindentation. *Thin Solid Films*, *429*(1), 201-210.

[13] Chen, X., & Vlassak, J. J. (2001). Numerical study on the measurement of thin film mechanical properties by means of nanoindentation. *Journal of Materials Research*, *16*(10), 2974-2982.

[14] Bhushan, B. (Ed.). (2004). *Springer handbook of nanotechnology*. Springer.

[15] Fischer-Cripps, A. C. (2011). *Nanoindentation* (Vol. 1). Springer.

[16] Gibson, L. J., & Ashby, M. F. (1999). *Cellular solids: structure and properties*. Cambridge university press.

[17] Chen, X., & Vlassak, J. J. (2001). Numerical study on the measurement of thin film mechanical properties by means of nanoindentation. *Journal of Materials Research*, *16*(10), 2974-2982.

[18] Namazu, T., & Inoue, S. (2007). Characterization of single crystal silicon and electroplated nickel films by uniaxial tensile test with in situ X-ray diffraction measurement. *Fatigue & Fracture of Engineering Materials & Structures*, *30*(1), 13-20.

[19] Ebrahimi, F., Bourne, G. R., Kelly, M. S., & Matthews, T. E. (1999). Mechanical properties of nanocrystalline nickel produced by electrodeposition.*Nanostructured Materials*, *11*(3), 343-350.

[20] Kurokawa, T., Gong, J. P., & Osada, Y. (2002). Substrate effect on topographical, elastic, and frictional properties of hydrogels. *Macromolecules*,*35*(21), 8161-8166.

[21] Matzelle, T., & Reichelt, R. (2008). Review: Hydro, micro-and nanogels studied by complementary measurements based on SEM and SFM. *Acta Microscopica*, *17*(1), 45-61.

Conclusion & Recommendations

6. Conclusion & Recommendations

This thesis demonstrates the versatility of virus-enabled nanowire synthesis and 2D/3D porous network assembly. The M13 virus toolkit was combined with a variety of nano/micro fabrication techniques to produce novel and potentially useful structures for lithium batteries and dye sensitized solar cells. Chapter 1 introduced the M13 virus platform, describing the virus structure and genetic engineering possibilities. In Chapter 2, virus-enabled titanium oxide nanowire synthesis was combined with polyelectrolyte multilayer assembly to create porous 3D networks to enhance electron diffusion in a dye sensitized solar cell. In Chapter 3, virus-enabled cobalt oxide nanowire synthesis was combined with polyelectrolyte multilayer assembly and soft lithography to realize ultrathin microbattery electrodes. In Chapter 4, virus-enabled copper nanowire synthesis was combined with hydrogel crosslinking to create a conductive battery electrode. Finally, in Chapter 5, we evaluated the mechanical robustness of various virus-assembled 3D networks including virus aerogels, virus carbon nanotube aerogels, and metal nanowires networks.

Further research is needed to realize high performance energy devices and fabrication methods suitable for high-volume, low-cost manufacturing. For example, to help position dye sensitized solar cells as a competitive choice in the global photovoltaics market, we must find ways to achieve the enhanced diffusion length described in Chapter 2 while simultaneously improving other figures of merit, facilitating low-cost production, and using more environmental materials. New device architectures and materials are likely needed for long-term viability in the highly competitive photovoltaics market. To fully leverage the thin microbattery electrodes described in Chapter 3, interdigitated or

3D battery architectures may be necessary. Finally, to create a lightweight battery as discussed in Chapter 4, all aspects of the battery—including the device packaging—must be further researched and optimized.

Readers looking for ideas for future research are encouraged to expand upon some of the virus assembly techniques described in this thesis. For example, it may be possible to combine the substrate geometry-driven virus alignment show in Chapter 4 (Figure 4.4) with the micro-contact printing technique shown in Chapter 3 (Figure 3.2) to create a scalable process for printing aligned nanowires. The virus carbon nanotube (CNT) aerogels mechanically tested in Chapter 5 (Figure 5.5) may also have interesting applications awaiting investigation. I recommend further research into polypeptide interactions with carbon nanotubes and graphene, as carbon-based materials will likely play an important role in multiple industries, just as iron and silicon had enabled tremendous technological progress in history. Computational studies modeling peptide interactions with carbon lattices will help inform future experiments and increase our scientific understanding of carbon nanostructure-biomolecule interactions.

Biological tools such as the M13 virus provide a means to quickly evaluate nano- and microstructures that are difficult to prototype with existing industrial methods, and produce sophisticated nanostructures with relatively few processing steps and scale-up constraints. As shown in Figure 1.2, we have relentlessly pushed the boundaries of what technical feats are considered possible using a simple virus particle, and will continue to enhance the virus toolkit and develop creative, multidisciplinary applications. Nevertheless, new biotemplating tools should be explored and developed to produce an even wider range of products that benefit society at large. I therefore recommend

pursuing genetic engineering (e.g., via synthetic biology) to create new biological devices specifically designed to facilitate organic-inorganic materials interfacing and nanomaterials templating. It is my hope that future researchers and sponsors pursue this nanobiotechnological avenue with audacity, as the invention of new tools is what ultimately enables great leaps in science and technology.

Appendix

7. Appendix

7.1. Virus Engineering and Amplification

7.1.1. Virus Clones

The M13 bacteriophage (virus) strains used in this work are termed E3, Y21M, and DSPH. The E3 strain has a genetically modified fusion protein on the 2,700 copies of the p8 coat protein that consists of a tetra-carboxylate moiety at the solvent exposed N-terminus. The coat protein charge density can then be controlled via pH.[1] The DSPH strain presents the aromatic proline and histidine amino acids on the terminal p8 fusion creating an affinity for hydrophobic carbon nanotubes.

The viruses were amplified using the ER2738 *E.coli* strain and purified using standard polyethylene glycol (PEG) precipitation protocols. Collected virus stocks were stored in 1 x phosphate buffered saline (1xPBS). Virus quantity was quantified using a Nanodrop 1000 UV/VIS spectrophotometer. The Nanodrop nucleic acids function was used to determine absorbance at 269nm and 320nm. Absorbance values were used in Equation 8 below to determine virus concentration in virions per milliliter (virions/ml). The numerator includes the difference between the peak DNA absorbance at 269nm and the absorbance of aromatic protein residues at 320nm multiplied by the extinction coefficient of 6×10^{16}. The denominator is the number of base pairs in the E3 clone.

Equation 8

$$\text{Virus concentration} = \frac{(A_{269}-A_{320})\times 6\epsilon 16}{7220}$$

The pVIII coat proteins on E3 and Y21M are identical. The E3 clone has an EEED protein fusion sequence on the N-terminus of pVIII. Note that there are four carboxylic acid functional groups at the p8 N-terminus with three glutamates and one aspartate. The E3 clone was derived from the E4 clone with an EEEE protein fusion, where a mutation resulted in a change from a glutamate to an aspartate residue. The Y21M clone substitutes methionine for tyrosine at the 21st amino acid residue on the pVIII coat protein.[2] The amino acid residue substitution is on the interior of the virus capsid and increases its persistence length,[3] but does not alter the binding properties of exterior coat protein.

7.1.2. Large Scale Amplification

A large scale virus amplification protocol is shown here.

DAY 1

Note: Need to have fresh ER2738 E.coli plate ready beforehand.

Step 1: LB Broth Preparation (pre-autoclave).

- Rinse 6 x 2L flasks to remove dust.
- Fill up with ~1L deionized water.
- Add Difaco LB Broth / LB Broth Base / LB Medium (follow package instructions for amount).
- Cover opening with aluminum foil.
- Place autoclave tape on top.

Step 2: PEG creation (pre-autoclave).

- In 1 x 2L Pyrex container, add 1500mL deionized water.
- Add 300g (200 g/L) PEG Glycol 8000.
- Add 220g (146.38 g/L) NaCl.
- Screw on cap and mix.
- Place autoclave tape on top.
- Unscrew cap slightly.

Step 3: Autoclaving Materials Preparation.

- 6 x 2L flasks (containing LB broth).

- 1 x 2L Pyrex container (with barely screwed cap, containing PEG).
- 10 x ~30 mL bottles (for use in high speed centrifugation; when autoclaving, place in 2L beaker).
- 18 x ~250 mL bottles (for use in high speed centrifugation).
- 2 x 150mL flasks (for use in TET preparation).
- Autoclave 30 min.

Step 4: Tetracycline (TET) Preparation.
- In 2 X 150mL flasks, add 75 mL LB Broth.
- Add 1:1000 TET (mixed w/ methanol, based on pg. 5 of Phage Display book).[4]
- Quantity: 20mg/mL LB.

Step 5: Overnight Cultures.
- Clean bio hood with water and ethanol.
- Take Petri dish w/ E. coli colonies, pick up one colony of E. coli with blue stick (with circle at end; be sure not to contaminate the stick upon removal from the bag).
- Place one colony in each TET flask.
- Place each flask w/ colony in shaker (37 Celsius; w/ Al foil loosely covering flask opening) overnight.

DAY 2

Step 6: Infection.
- Add 1/100 (volume) of overnight culture to LB broth (~ 20μL virus).
- Let sit for 4.5-6 hours in 37 Celsius incubation with heater and shaker.

Step 7: Slow centrifuge #1
- Pour flasks into conical tubes (grenade bottles), as many as needed but likely approximately 24 (4 per L).
- Pair bottles by mass, using water to balance each pair (to stabilize the centrifuge).
- Place in slow centrifuge (Settings: 10min, ω=3.5 rpm) four at a time.
- Following centrifugation, transfer from conical tubes to large high-speed centrifugation bottles by sucking out the remaining liquid (containing virus) and disposing of the bottles and the remaining bacteria (biohazard).
- Should be about 4 conical tubes per 3 high speed bottles (leave room to add 1/6 PEG).
- Add 1/6 (volume) PEG to each high speed bottle, shake, store in fridge overnight.

DAY 3

Step 8: High speed centrifuge #1.
- Remove high speed bottles from fridge storage.

- Tighten before centrifugation.
- Place in high speed centrifuge (Settings: JLA 10.500, 9500 rpm, Time 0:15, Accel-max, Decel-max, Temp 4 Celsius).
- Following centrifugation, dump out remaining liquid in bottles (preserving virus collected on side of bottle).
- Using GlassMaster, suck out remaining liquid.
- Use 30 mL deionized water to dissolve virus for each set of 3 bottles (using GlassMaster to rinse virus from walls), then put virus solution from each set into blue/orange capped bottles.

Step 9: Slow Centrifuge #2.
- With virus in blue-capped bottles, spin in slow centrifuge (after evening out with water).
- Settings: 10min, ω=3.5 rpm.
- After centrifugation, suck out fluid and transfer to white capped bottles for high speed centrifugation. Throw away blue capped bottles and remaining bacteria.
- Add 1/6 PEG to each white capped bottle (~5mL).
- Keep in fridge overnight.

DAY 4

Step 10: High speed centrifuge #2.
- Balance the white capped bottles with water (in pairs).
- Place in high speed centrifuge.
- Settings: JA 25.50, 12000 rpm, accel- max, decel- max, time 0:15, Temp 4 Celsius.
- Suck out and throw away liquid.
- Add ~2 mL deionized water to each bottle, and break up and dissolve the virus.
- Collect virus solution in sterile container.
- Put into 4 Celsius fridge.

Purposes of steps:
1. To provide an environment for the growth of virus (nutrients, etc.).
2. PEG help virus separate from liquid.
3. To sterilize the containers used for Large Scale Amplification.
4. TET is an antibiotic, and the E. coli we use is resistant to TET so it will kill any unwanted bacteria.
5. Provides a source of bacteria to add to the LB Broth for virus to infect.
6. Gives the virus time to infect the *E. coli* and reproduce.
7. Centrifuge to remove the bacteria in solution as to isolate the virus.
8. Centrifuge to remove the virus from the solution.
9. Centrifuge to remove the bacteria still clumped with the virus

10. Centrifuge again to remove the virus from the solution.

7.2. Virus Layer-by-Layer Solid-State Dye Sensitized Solar Cell

A cleaned TCO substrate (TCO10-10, Solaronix) with TiO_2 separation layer (60nm thickness, prepared by e-beam evaporation) was repetitively immersed into the following sequence of aqueous solutions: E3 bacteriophage (0.3ng ml^{-1}), LPEI (250,000 Mw, 0.02M, pH 4.75), PAA (90,000 Mw, 0.02M), LPEI (250,000 Mw, 0.02M). LPEI (25,000 Mw, 0.02M) was used as base-layer. Each immersion step (15min) was followed by two rinsing steps (5min each) in Milli-Q water. The pH-value of the solutions and of the rinsing bathes was adjusted to pH 4.75 by adding 0.01M HCl or 0.01M NaOH in appropriate amounts. The immersion and rinsing steps were performed using a programmable slide-stainer (Zeiss).

The LbL-assembled multistack was exposed to $(NH_4)_2TiF_6$(aq) (10 mM, pH 2.25) for 30 min, and then an equivalent volume of H_3BO_3 (100 mM, pH 2.25) was added. The sample was removed from the solutions after 10h, quickly rinsed in Milli-Q water, dried and calcined at 450°C for 30min. Next, the sample was immersed into a $3 \cdot 10^{-4}$M solution of tris(isothiocyanato)-ruthenium(II)-2,2':6',2''-terpyridine-4,4',4''- tricarboxylic acid, tris-tertrabutylammonium salt ("black dye") (Solaronix) in ethanol for 24h.

A formulation consisting of 0.3g poly(ethylene oxide-co-epychlorohydrin), 0.075g ethylenecarbonate, 0.075g propylenecarbonate, 0.03g NaI and 0.003g I_2 in 25mL acetone was drop-casted at 60°C on to the sample and sandwiched by a Pt-coated counter-electrode (40nm Pt on ITO from Delta Technologies, prepared by e-beam evaporation). Construction of the DSSC is done such that uncovered areas of the TCO-anode and the Pt-cathode are available to apply electrical contacts.

Current-voltage characteristics of the solar cells were tested using an EG&G 263A potentiostat. An Oriel 150W Xenon lamp served as a light source in combination with an AM 0 and AM 1.5 global filter. Light intensity was measured by a Newport multi-function optical meter with a thermopile detector. The tested sample areas were $0.5cm^2$.

7.3. Virus Hydrogel and Aerogel

Glutaraldehyde is a five carbon chain with aldehyde groups at either end and is a commonly employed protein crosslinking agent.[5] While the exact mechanism of glutaraldehyde crosslinking remains uncertain, the conventional concept is that one of the aldehyde groups on glutaraldehyde forms a covalent bond with a lysine residue on one protein target, while the second aldehyde group binds a second protein, effectively crosslinking them. The covalent bonding mechanism is believed to be either an aldol condensation[6] or Michael reaction.[7]

Stock 50% Glutaraldehyde Solution (Sigma Aldrich, CAS# 111-30-8) was placed in a reservoir. The specific gravity of the glutaraldehyde solution is 1.106. Virus solutions (either E3 or Y21M) in 1xPBS were pipetted onto a substrate. The loading factor for test samples was 10μl on an approximately $1cm^2$ single crystalline silicon substrate. Substrates with virus solution were inverted and placed onto the glutaraldehyde solution surface. The virus solution was allowed to remain in contact with glutaraldehyde for 30min. Crosslinked virus solutions were removed from the glutaraldehyde solution and transferred to 1L, 1xPhosphate Buffered Saline (PBS) for 12-24h to remove excess glutaraldehyde from the resulting hydrogel.

Film-like hydrogels were prepared with 0.1ml E3 virus at $1x10^{14}$viruses/mL, buffered in 1x phosphate buffered saline (PBS) on a $1cm^2$ silicon substrate. Substrate sidewalls were formed with parafilm. The silicon-virus assembly was placed upside-down in a stock solution of 50% glutaraldehyde. A virus-glutaraldehyde phase boundary occurs due to the differential specific gravities of the two solutions such that the resulting hydrogel is approximately the same volume as the starting virus solution. After 1.5h of virus crosslinking, the film hydrogel was dialyzed in DI water (18.2Ω) to remove excess glutaraldehyde. The film hydrogel sample was approximately 100μm thick. The DSPH-SWCNT hydrogel was prepared with 0.1mL DSPH M13 bacteriophage at $1x10^{14}$viruses/mL in DI water. DSPH virus was incubated with a 20-fold stoichiometric excess of single wall carbon nanotubes approximately 500nm in length and 0.8nm in diameter in DIW and 2% (w/w) sodium cholate for 48h. The CNT bound virus was then dialyzed against DI water and crosslinked as above.

To form aerogels, DSPH virus at $1 \cdot 10^{14}$ viruses/mL was incubated with a 20-fold excess of single wall carbon nanotubes approximately 500nm in length and 0.8nm in diameter in DI water and 2% (w/w) sodium cholate, for 48h. The resulting virus suspension was gray in color. 0.1ml of the virus solution was placed in a microfuge tube and 0.1ml of stock 50% glutaraldehyde was pipette below the virus solution. A distinct phase boundary was observed between the glutaraldehyde and the virus solution with the virus remaining above based on differences in specific gravity. The crosslinking proceeded for 2h before dialysis with DI water to remove excess glutaraldehyde. The resulting virus-SWCNT aerogel was then supercritically dried to form an aerogel. Some

volume decrease was observed. A significant volume decrease (> 50%) was observed in previous experiments using critical point drying of the virus hydrogels.

7.3.1. Aerogel Drying

Supercritical drying was performed on a Tousimis Autosamdri Model 815 critical point dryer. Samples were immersed in 50%, 75%, then 100% ethanol to displace water. CO_2 has critical point temperature 31.1ºC and pressure 1072psi. Samples were placed in isopropyl alcohol in machine and dried in six steps:

1. Cool to below 10ºC at less than 500psi.
2. Fill with liquid CO_2.
3. Purge alcohol from sample chamber.
4. Heat to greater than 31.1ºC, greater than 1071psi.
5. Bleed CO_2 at 32-40ºC.
6. Vent chamber to less than 400psi but still above 31.1ºC.

Freeze drying was performed on Labconco Model 7934000 lyophilizer. The process removes water from materials quickly frozen by liquid nitrogen by converting the frozen water directly into its vapor without the intermediate formation of liquid water (i.e. sublimation). In contrast, drying at ambient temperatures from the liquid phase usually results in structural changes in the product.

The basis for this sublimation process involves the absorption of heat by the frozen sample in order to vaporize the ice; the use of a vacuum pump to enhance the removal of water vapor from the surface of the sample; the transfer of water vapor to a collector; and the removal of heat by the collector in order to condense the water vapor. In essence, the freeze dry process is a balance between the heat absorbed by the sample to

vaporize the ice and the heat removed from the collector to convert the water vapor into ice.

The freeze drying process consists of three stages: prefreezing, primary drying, and secondary drying.[8] Since freeze drying is a change in state from the solid phase to the gaseous phase, material to be freeze dried must first be adequately prefrozen. Rapid cooling results in small ice crystals, useful in preserving structures to be examined microscopically. Slower cooling results in larger ice crystals and less restrictive channels in the matrix during the drying process, but the sample is less likely to crack.

During primary drying, the rate of sublimation of ice from a frozen product depends upon the difference in vapor pressure of the product compared to the vapor pressure of the ice collector. Molecules migrate from the higher pressure sample to a lower pressure area. Since vapor pressure is related to temperature, it is necessary that the product temperature is warmer than the cold trap (ice collector) temperature. It is very important that the temperature at which a product is freeze dried is balanced between the temperature that maintains the frozen integrity of the product and the temperature that maximizes the vapor pressure of the product. This balance is needed for optimum drying.

Heat must be applied to the product to encourage the removal of water in the form of vapor from the frozen product. The heat must be very carefully controlled, as applying more heat than the evaporative cooling in the system can remove warms the product above its eutectic or collapse temperature.

Secondary drying is needed because, after primary freeze drying is complete, and all ice has sublimed, bound moisture is still present in the product. The product appears dry, but the residual moisture content may be as high as 7-8%. Continued drying is

necessary at the warmer temperature to reduce the residual moisture content to optimum values. Because the process is desorptive, the vacuum should be as low as possible (no elevated pressure) and the collector temperature as cold as can be attained.[9]

7.3.2. Nanotube Integration

A single wall carbon nanotube (SWCNT) preparation protocol is shown below. The protocol was edited from a protocol by Hyunjung Yi based on documented procedures by the MIT Strano Lab.

1. Prepare 200mL of 2wt% sodium cholate (SC) aqueous solution in 400mL beaker
   Make 50mL extra and save it for UV-Vis blanking
   For 500mL, assume 500g water -- 2 wt% SC = 10g SC
2. Dissolve 400mg* of Hipco (Unidyme) SWCNT onto solution from 1.
3. Use homogenizer** (small one) for 1hr at level 2 or 3. Dip the tip until the 1/3 height from the bottom of the solution is immersed.
4. Do cup-horn sonication*** for 10min. In order to get a higher concentration-solution (higher than 70µg/ml) of Unidyme Hipco SWCNT, use probe tip instead of cup-horn. For probe tip case, use 6mm tip and power amplitude is 40% and sonicate for 1h. Use ice bath and use 50mL falcon tube in a beaker. Dip tip in water and let it run at least 10min to clean first.
5. Do ultracentrifuge (aliquot 35~40mL onto 5 centrifuge tubes and prepare 1 tube for balance) the ultrasonicated solution at 30,000 rpm (SW-Ti32 bucket) for 4h. If using SW28 at 25,000rpm, 318min. To calculate the rotor conversion, go to Rotor Calculator: <http://www.beckmancoulter.com/products/discipline/life_science_research/pr_disc_gen_centrif.asp>
   Turn on vacuum, set temp to 4ºC, wait to cool until vacuum 250 flashes (~10min)
   Balance tubes to within .01g (about 29.70g liquid per tube)
   Match the containers, caps, and hanging locations according to #
   Dimples on side of rotor 90 degrees off relative to spin shaft pins
   Press vacuum (wait until vacuum 200 is lit solidly)
   Speed: 25000, Time: 5:18, Accel: Max

Hit Enter, then hit Start

Supervise machine until it reaches top speed (watch out for leak, imbalance)

6. Decant and take the top half (20mL from each tube) of the centrifuged solution.

From 200mL original volume, we obtain 100 mL of product and the concentration is ~20µg/ml.

* For powder type, some used 40mg, but for mud-type, use 80mg since the yield is much lower for mud type. 400mg gives a concentration of about 20mg/L .

** Homogenizer: IKA T10 basic ultra turrax (small one) cf. big one: ultra turrax IKA werke T25 basic power.

*** Ultrasonicator: Cole Parmer Ultrasonic Processor: Full power is 750W but actual power to be used is ~100W.

For separation, perform ultrasonic session with probe tip (power is about 150W but actually power is about 15 (10%). 30 ml for 1h) do centrifuge at 32,000rpm (SW-Ti32.1 bucket) for 12h.

Getting concentration of SWCNT solution:

1. Warm UV lamp about 30min before your measurement.
2. Prepare blank solution (2wt% sodium cholate solution)
3. Open the software DU800 and use “wavelength scan II”.
4. Open “edit method” and set up your application with scan mode “Abs”, Start wavelength “200”, end wavelength “1100”, scan speed “240nm/min, and press OK.
5. Wash the micro cell with DI water and blow it to get rid of any water droplet.
6. Place 100µl of blank sample into the micro cell without forming any bubble inside and press “BLK”.
7. Place 100µl of your sample into the micro cell and press “GO”.
8. Save your data and export to txt file to look at the abs value at wavelength 632nm.
9. Multiply 27 to this abs value (this is for 1cm micro cell) and result gives the concentration in µg/ml (e.g. Abs is 0.889 at 632nm, the concentration is 0.889 * 27=24.003 µg/ml).

7.4. Electroless Deposition

Copper nanowire networks were synthesized by starting with a film bound hydrogel. After dialyzing the gel against DI water, the gel was exposed to 10mM Na_2PdCl_4 (Strem Chemicals, CAS# 13820-53-6) for 2h. Palladium exposure changed the gel color from translucent white to pale brown. The palladium sensitized gel was dialyzed against DI water to remove excess palladium ions. The gel was then exposed to 10mM dimethylamine borane (DMAB) (Alfa Aesar, CAS#74-94-2) buffered in 25mM 2-(N-morpholino)ethanesulfonic acid (MES) (Research Organics, CAS#: 145224-94-8) at pH 7. Reduction of palladium bound the virus gel was evidenced by the gel changing color from pale brown to black. The gel was then immersed in 10ml of a copper electroless deposition (ELD) solution consisting of: 0.032M $CuSO_4$•$5H_2O$ (Mallinckrodt, CAS#4844-02), 0.04M ethylenediaminetetraacetic acid (EDTA) (Mallinckrodt, CAS#6381-92-6), 0.067M DMAB, and 0.1M tris buffered saline (TBS) at pH 7.

Nickel nanowire "thick" film networks were prepared as for copper nanowire networks with a change of ELD solutions. The nickel ELD used was: 0.032M $NiSO_4$•$6H_2O$ (Aldrich, CAS#22767-6); 0.04M Glycine (Mallinckrodt, CAS#56-40-6); 0.004M EDTA; 0.067M DMAB; 0.1M MES buffer at pH~7. Films were detached from the underlying substrate with a razor blade and mounted with conductive carbon tape on a SEM stub for cross-sectional imaging. The free standing nickel film was then placed in 0.1ml DI water and dried at 50˚C on a silicon chip. The capillary action of drying flattened the nickel film onto the silicon substrate for nanoindentation.

For nickel nanowire "thin" film networks, hydrogel films were prepared on silicon substrates with E3 virus with a concentration of 8.23e13viruses/mL as described

above. Gels were sensitized in10mM $(NH_3)_4PdCl_2$ (Aldrich, CAS#323438-5G) for 1h and then reduced in 0.1M DMAB, 0.25M MES at pH 6.5 for 1h. The nickel ELD consisted of: 0.0032M NiSO4, 0.002M glycine, 0.002M EDTA, 0.004M MES buffer, 0.0067M DMAB with a pH of 7. Deposition proceeded for 14.5h for Sample 3 and 20.5h for Sample 4.

For contact immersion plating in the battery electrode study, 0.02M tin (II) chloride dihydrate (Alfa Aesar, CAS # 10025-69-1) and 0.12M ethylenediamino tetraacetic acid, disodium, dehydrate (EDTA) (Mallinckrodt 78 Chemicals, CAS# 6381-92-6) were dissolved in 0.1M sodium hydroxide. Copper nanowire films were wetted with the tin solution. Commercial aluminum foil was placed in contact with the wetted copper film for 2-3 minutes. The copper-tin film was rinsed in deionized water for 30 minutes and then dried at room temperature.

Tin immersion solutions consisted of: 0.129M tin (II) methansulfonate, 50% (Aldrich, CAS # 53408-94-9) ; 0.756M sodium hypophosphite monohydrate (Sigma-Aldrich, CAS # 10039-56-2) ; 1.05M thiourea (GE Healthcare, 62-56-6); and 0.789M methane sulfonic acid (Sigma-Aldrich, CAS # 75-75-2). Dry copper nanowire films were immersed in 10ml of the tin plating solution for 5, 10, 15, 30, and 45min. Films were then placed in deionized water for 1h to quench the plating process and then dried with nitrogen gas. Additional samples were prepared using the same tin immersion solution, but samples were placed on a VWR mini-shaker at 140rpm for 5min during the plating process and then quenched and dried as above.

The detailed step-by-step protocol for virus nanowire network formation written by Dr. John Burpo is shown here:

Materials needed:

1. E3 virus stored in PBS. Y21M "stiff virus" may also be used.
2. Silicon wafer substrate. Other materials such as glass, ITO, FTO and metal foils will work.
3. Glutaraldehyde. 50% stock. Sigma-Aldrich.
4. Copper sulfate, pentahydrate. Mallinckrodt Chemicals.
5. EDTA, ethylenediamino tetraacetic acid, disodium, dehydrate. Mallinckrodt Chemicals.
6. Borane dimethylamine complex, DMAB. Aldrich.
7. Tetraaminepalladium(II) chloride monohydrate, $(NH_3)_4PdCl_2 \bullet H_2O$. Aldrich.
8. Nickel (II) sulfate hexahydrate, Aldrich 10101-97-0.
9. Sodium DL-Lactate (Lactic Acid), Sigma-Aldrich, 72-17-3.

Step 1: Hydrogel Formation

1. Concentrate stock virus solution by pipetting 1ml aliquots into microfuge tubes.
2. "Pre-spin" virus at 10k rpm for 5min to remove residual *E.coli*. If faint pellets form at the bottom of the tubes, transfer supernatant to new microfuge tubes.
3. Add 1/6 (v/v) PEG to microfuge tubes and put on ice for at least one hour, or leave in 4C refrigerator overnight. This is the same as a PEG precipitation step in virus amplification.
4. Spin microfuge tubes at 14k rpm for 10min. A white pellet should form at the bottom of the tubes.

5. Remove and discard supernatant. Ensure as much of the liquid phase is removed as possible without disrupting the virus pellet.
6. Resuspend the pellets in 35-50μL of 1xPBS. The number of virus particles in the pellets can be calculated from the initial stock concentration. The required volume for the desired final concentration can be determined from the dilution equation.
7. Heat the microfuge tubes at 50˚C for 20min. This step helps to thermally disaggregate the pellets.
8. Tap and vortex tubes to disrupt the virus pellet. The pellet should start to dislodge from the tube walls.
9. Heat again at 50˚C for 15min. Tap and shake tubes. DO NOT VORTEX any further. Vortexing is avoided in all subsequent steps based on the observation of virus aggregation previously seen on polymer electrolyte films with AFM imaging.
10. Determine the final concentration of the virus solution using Nanodrop/Nucleic Acids. Virus films have been successfully prepared at concentrations ranging from $1e^{13}$-$2e^{14}$ viruses/mL.
11. Cut ~1cm^2 silicon wafer chips.
12. Pipette 10μL of virus solution onto silicon. Plasma treatment of the silicon will result in better wetting of the substrate and more even film surface. Virus volume can be varied to control the thickness of the resulting virus hydrogel.
13. In a fume hood, pour enough 50% stock glutaraldehyde to cover the bottom of a culture dish. Note: Glutaraldehyde is the leading cause of occupational asthma in America due to its use as an antiseptic in hospitals.

14. Invert the silicon/virus and place upside down onto the glutaraldehyde in the fume hood. The silicon chip with virus solution will float on the glutaraldehyde surface due to 1) the surface tension of glutaraldehyde and 2) the lower specific gravity of the virus solution compared to glutaraldehyde.
15. Allow the cross-linking to proceed for 30min. Cross-linking times as short as one minute have also been used. Minimum cross-linking time is likely a function of the diffusion time of glutaraldehyde through the thickness of the virus solution. Cross-linking times up to 2h have been used for thick (> 1mm) gels.
16. Remove the silicon/virus gels from the glutaraldehyde and blot the excess glutaraldehyde from the edges of the silicon. Ensure that the virus gel does not come in contact any surface/object.
17. Hold the silicon/virus gel vertically in 1L 1xPBS to allow residual glutaraldehyde to sediment off of the gel.
18. Place the gel right side up in 1xPBS overnight to dialyze the excess glutaraldehyde from within the gel. No dialysis membrane is required as the virus hydrogel acts as its own dialysis membrane.

Step 2: Palladium Sensitization

1. Prepare 10mM Tetraaminepalladium(II) chloride monohydrate, $(NH_3)_4PdCl_2 \bullet H_2O$. Concentrations as low as 1mM have been successfully used.
2. Prepare 0.1M MOPS buffer and adjust pH to 7.
3. Transfer the silicon/virus gels to 0.5L of 0.1M MOPS and conduct a buffer exchange for at least 4h. Blot excess PBS from gels prior to insertion into MOPS. This step is conducted to eliminate the possibility of a palladium phosphate precipitation reaction.

4. Remove the gels from MOPS, blot away excess buffer, and place in a culture dish.
5. Pipette sufficient volume of palladium solution to cover the chip/gel. This will be ~100-200µl.
6. Incubate the gels for at least 6h.
7. Blot away excess palladium solution and transfer gels to 0.5-1L, 0.1M MOPS overnight to remove excess palladium ions from the gels.

Step 3: Copper Electroless Deposition

1. Prepare the copper electroless deposition (ELD) solution with the following concentrations: [$CuSO_4$] = 0.032M; [EDTA] = 0.040M; [MOPS] = 0.1M; [DMAB] = 0.067M. pH adjusted to 7.
2. Immerse samples in Cu ELD for the amount of time required to achieve the desired nanowire diameter (see Cu NW growth curve in Results below). 6h is a good duration to achieve an integral film. Heat treatment in a tube furnace at 350˚C for 30min results in copper nanowire film detachment from the silicon substrate, likely due to thermal expansion mismatch between silicon and copper.
3. Remove samples and rinse in DI water for at least 30-60min to allow excess ELD to diffuse out of the film. Prolonged exposure may result in oxidation of nanowires.
4. Remove samples from water and blot excess water taking care not to directly touch the nanowire film.
5. Nitrogen gas can be applied to help remove excess water and accelerate drying. Avoid high pressure gas as it may tear the nanowire film.

Step 3 (alternate): Nickel Electroless Deposition

1. Prepare the nickel electroless deposition (ELD) solution with the following concentrations: [$NiSO_4$] = 0.032M; [Lactate] = 0.064M; [MOPS] = 0.1M; [DMAB] = 0.067M. pH adjusted to 7.
2. Immerse samples in Ni ELD for the amount of time required to achieve the desired nanowire diameter (see Ni NW growth curve in Results below). 60min is a good duration to achieve an integral film. Nickel films have maintained porous morphology in temperatures up to 650˚C for 30min.
3. Remove samples and rinse in DI water for at least 30-60min to allow excess ELD to diffuse out of the film. Prolonged exposure may result in oxidation of nanowires.
4. Remove samples from water and blot excess water taking care not to directly touch the nanowire film.
5. Nitrogen gas can be applied to help remove excess water and accelerate drying. Avoid high pressure gas as it may tear the nanowire film.

7.5. Scanning Electron Microscopy / Focused Ion Beam

In Chapter 3, SEM images were obtained using JEOL instruments (JSM-6060 and 6700F) and sputtered with approximately 4nm of Pd and Au before imaging. In Chapter 4, a FFEI Company Helios 600i Nanolab Dual Beam SEM/FIB was used for high resolution imaging and for cross-sectional FIB etching samples and energy X-ray dispersive spectroscopy (EDS). The FEI XL-30 ESEM (Environmental Scanning Electron Microscope) was used for general purpose imaging.

7.6. Energy Dispersive X-Ray Spectroscopy

Energy dispersive x-ray spectroscopy (EDS) was performed using the FEI Company Helios 600i Nanolab Dual Beam SEM/FIB. Samples were placed at a working distance of 10.5mm and an accelerating voltage of 10kV was used. Spectra were collected and initially analyzed for peak identification and mass composition using INCA software. Spectra files were then exported as text files and plotted using Microsoft Excel.

7.7. Optical Microscopy

An Olympus microscope (IX51) was used for optical imaging.

7.8. X-Ray Diffraction

In x-ray diffraction (XRD), x-rays travel through a specimen and are scattered by the regularly spaced atoms in the specimen material. The crystal structure(s) of the powdered specimen are then determined by matching the characteristic diffraction peaks with those in a database. XRD data was generally collected on a Rigaku Rotaflex RU 300. In Chapter 4, we used PANalytical X'Pert Pro X-ray diffractometer with Cu K_α radiation (λ = 1.54060Å), a 2Theta-Omega scan axis, and a scan step size of 80.0100s. A 1˚ offset was used for copper and nickel film samples on single crystalline silicon wafers to minimize silicon (100) peaks. Sample irradiation lengths varied between 0.4 and 0.6cm.

7.9. Four-Point Probe Conductivity Testing

A Keithley 4200-SCS Semiconductor Characterization System was used as a four-point probe to determine resistivity and conductivity of film samples in conjunction with film thicknesses determined from profilometry. The probe head consisted of four

tungsten carbide probes 62.5mil (1.5875mm) apart for a total width of 4.7625mm between the outer probes. Current, I, sweeps of 0.1-100mV with 20 steps were sourced between the outer probes. The voltage difference, V_{diff}, was measured between the high impedance middle probes. Resistance was calculated as $R = V_{diff} / I$. Resistance was verified to obey a linear, ohmic relationship. Sheet resistance was calculated as $R_{sq} = 4.53 \times R$. Using film thickness, t, determined with profilometry, film sample resistivity, ρ, was calculated as:

Equation 9

$$\rho = \frac{\pi}{ln2} \frac{V_{diff}}{I} t$$

7.10. Image Analysis

ImageJ 1.45p software (U. S. National Institutes of Health) was used for pore size analysis of scanning electron microscope focused ion beam cross-section images.[10] SEM images were first optimized for maximum brightness/contrast and then converted to a binary black and white image, segmenting the image into pores and solids. Based on the image contrast of SEM images, void spaces are darker than the nanowires which scatter electrons. Thus, void spaces are converted to black particles during the binary image conversion. Set scale was used to calibrate the image scale to the software scale. The Analyze particles function was used to determine the area fraction, perimeter. The "include holes" option was left unchecked to ensure that nanowire area was not included in the pore space area fraction. A 102 pixel size was used as a particle size cut-off to eliminate noise of non-physical pores. The area fraction value was used as the cross-section porosity. The feret diameter statistic was used as an estimate of pore diameter.

Total contour length of pores in the 2-dimensional cross-section was determined by selecting all particles and using the Measure/Perimeter function.

7.11. Galvanostatic Cell Testing

In Chapter 4, copper-tin electrodes were dried in a vacuum chamber for 6h before transfer to an argon glove box. Test cells were assembled using lithium foil as the counter electrode in a coin cell. 1M $LiPF_6$ in ethylene carbonate: dimethyl carbonate (EC: DMC, 1:1 ratio) (Ferro Corporation) was used as the electrolyte with Celgard 3501 polypropylene separators. Cells were galvanostatically tested using a Solatron Analytical 1470E potentiostat.

Currents are reported using the C-rate convention C/n, where C is the capacity per gram of electrode active material corresponding to the theoretical capacity, and n is the number of hours for charge or discharge. The mass of active material was determined from averaged compositional energy dispersive X-ray analysis. Resulting cell capacities are normalized to both the active material mass with units of mAh/g, and normalized to the electrode area with units of mAh/cm^2. Electrode area was calculated from optical photographs using the Analyze Particles function in ImageJ software.

7.12. Atomic Force Microscopy

In Chapter 2, AFM investigations were performed with a Dimension 3100 AFM (Digital Instruments) in tapping mode.

In Chapter 3, the phase or height image of the assembled and transferred microbatteries was analyzed using AFM in tapping mode (Dimension 3000, Veeco

Instruments). In Chapter 3, the surface morphologies after the deposition of virus within the film were monitored using AFM (Dimension 3100 Nanoman, Veeco Metrology).

In Chapter 4, an Asylum Research MFP 3D was used to perform nanoindentation on all samples other than the nickel nanowire thin film networks. A silicon nitride cantilever with a Novascan 20μm borosilicate glass sphere (k_{nom} = ~0.03N/m) was used to indent hydrogel samples. An Asylum AC160TS cantilever, k_{nom} = ~42N/m, tip radius = 9 nm, was used to indent the virus-SWCNT aerogel. A Veeco/Bruker DNISP diamond probe, k = 314N/m, tip radius = 40nm, was used to copper and thick nickel samples. Deflection sensitivities and spring constants of the each indentation probes were calibrated prior to data acquisition.

7.13. Profilometery

A Veeco DEKTAK 150 Profilometer was used to determine sample thicknesses. A step height calibrated 2.5μm stylus was drawn over the sample with a 2.0-3.0mg force setting with ~200μm/s scan rate. Average step heights were determined by calculating the difference between average profile height values of the substrate and top of the film surface. Surface roughness, R_q, values were determined over length scales of greater than 1000μm. A Tencor P-10 profilometer was also used in Chapter 2.

7.14. Transmission Electron Microscopy

In transmission electron microscopy (TEM), an electron beam is focused onto a specimen. And as the electrons pass through the specimen, interactions with the specimen create beam distortions that are visible in a magnified projection on a phosphor screen.[11] In Chapter 2, TEM images were taken with a JEOL 200CX and cross-sectional cuts were

performed with a Leica Ultramicrotome. In Chapter 4 TEM images were generally captured on a JOEL JEM-2001XIA1 or JEOL 200CX TEM.

7.15. Instrumented Nanoindentation

Nanoindentation experiments were conducted in ambient conditions using a Hysitron, Inc. Triboindenter. Load-controlled nanoindentations were performed using a 10 μm diamond conical indenter. The maximum loads were set to be 50 and 100μN and the loading and unloading rate was kept constant, i.e. 10μN/s. To investigate the time-independent mechanical properties, the unloading rate was varied, i.e., 5, 10, and 20μN/s. 25 experiments per setting were performed in a square grid arrangement with each indent spaced 60μm apart. The probe tip area function, $A_c(h_c)$, was fitted with a 6^{th} order polynomial using the known properties of fused silica. The frame compliance of the instrument was calibrated separately using the indentation data of fused silica with a Berkovich indentation probe.

7.16. Copper Nanowire Network Thermal Annealing

A Thermolyne 79300 tube furnace was used to anneal copper and film samples synthesized on silicon wafers. Argon gas with 4% hydrogen gas was used during annealing. Annealing temperatures ranged from 400-600˚C with 30-45min ramp times. Copper nanomesh delaminated from Si substrate by annealing at 400ºC for 5min, ramping up at 50ºC/min, in forming gas with a glass slide with titania paste as sacrificial oxygen consumer.

7.17. Copper Mesh Thinning and Flattening

Commercially available copper mesh can be etched by nitric acid. Figure 6.4 shows 35% nitric acid etching copper mesh (200 mesh.002" wire diameter) at room temperature at ~0.5µm/s.

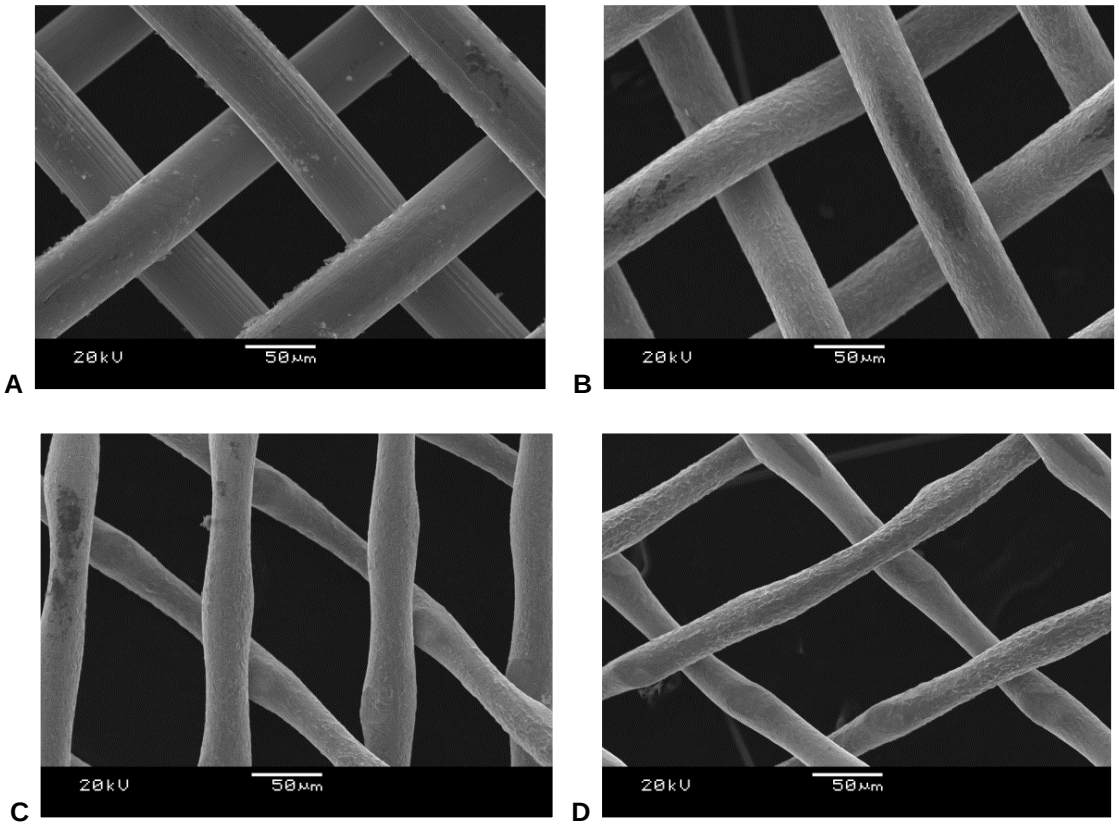

Figure 7.1. Gradual thinning of woven copper mesh by nitric acid etching. Scale bars are 50µm. Etch rate of 0.5µm/s determined by linear fitting.

Various etched and cold-rolled copper meshes can be mechanically or thermally bonded together, as shown in Figure 6.5. Cold-rolling was performed by first rolling a steel substrate to zero the rolling height, then rolling copper mesh once to flatten mesh. Rolled mesh and delaminated copper nanowire film bonded together by sandwiching between glass plates, with flat shiny side of nanowire film facing away from rolled mesh.

Glass plates held together by two binder clips with paint previously stripped. Bonding occurred at 400ºC for 15min, 50ºC/min ramp up, in forming gas with same titania surficial oxygen consumer. Images were taken with a JSM-6700F HR-FESEM.

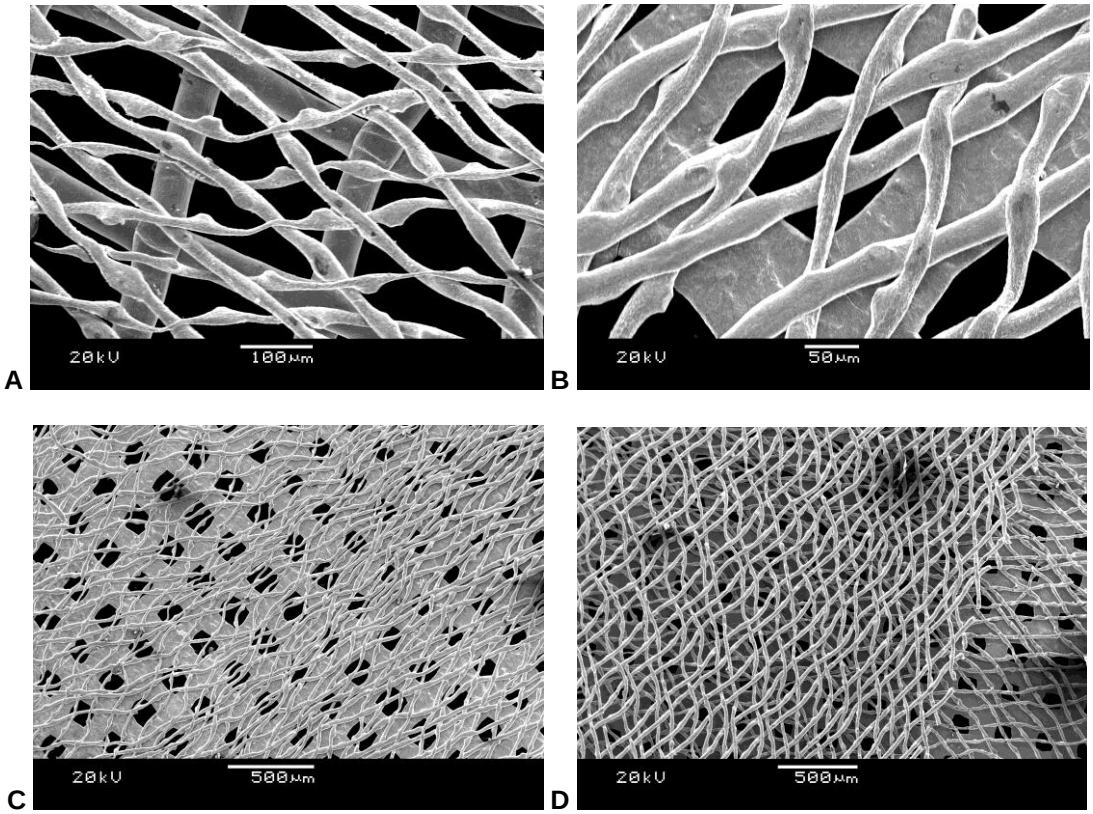

Figure 7.2. Thermally bonded copper meshes. A) Higher density acid etched copper mesh (200 mesh, 0.002" wire diameter, etched in 35% nitric acid for 60s) stretched then pressed onto unmodified, lower density copper mesh (145 mesh .0022" wire diameter) using hydraulic press with 20kN/cm^2 force. B) Higher density acid etched copper mesh (200 mesh, 0.002" wire diameter, etched in 35% nitric acid for 60s) stretched then pressed onto previously cold-rolled lower density copper mesh (145 mesh .0022" wire diameter) using hydraulic press with 20kN/cm^2 force. C) Same merged mesh at lower magnification. D) Two stacks of higher density acid etched copper mesh (200 mesh, 0.002" wire diameter, etched in 35% nitric acid for 60s) at different stretched orientations pressed onto previously cold-rolled lower density copper mesh (145 mesh, 0.0022" wire diameter) using hydraulic press with 20kN/cm^2 force. Scale bars are (a) 100µm, (b) 50µm, (c) and (d) 500µm.

7.18. Titanium Oxide Deposition

To synthesize TiO_2 free floating nanowire in aqueous solution, add 250µL E3 virus (~3e7viruses/mL) to 5mL 5mM $(NH_4)_2TiF_6$ (less than 1 week old; adjusted to pH 2 by adding ~10µL HCl). Let sit 0.5-3h. Add 5mL 50mM H3BO3 (adjusted to pH 2 by adding HCl). Let sit one day. Prepare TEM sample by dropping < 6µL onto non-carbon side of TEM grid. Note: This protocol does not scale. When using the same 1:20 virus:Ti ratio for 200mL total volume (instead of 10mL total volume), nanowires are not observed. TiO_2 was deposited on Y21M "Stiff Virus" by mixing 1mL 10mM $(NH_4)_2TiF_6$ with 1mL 100mM H_3BO_3, and by mixing 5mL 50mM $(NH_4)_2TiF_6$, with 1.5mL 150mM H_3BO_3.To embed gold nanoparticles in TiO_2 nanowires, "#9" gold-binding virus was mixed with 5nm gold colloidal suspension to bind nanoparticles onto the viruses. Then various proportions of 1mM $(NH_4)_2TiF_6$ and 3mM H_3BO_3 (pH 2.8) were added to deposit TiO_2.

To create virus-LbL TiO_2 photoanodes, LbL films were air dried and then exposed to 5 mM $(NH_4)_2TiF_6$ (Alfa Aesar) aqueous solution at pH 2.25 for 30 minutes to achieve a porous microstructure. The top skin on the porous polymer films was removed using a 5min oxygen plasma treatment, 10min soak in 2M NaCl solution at pH 2.25 (followed by a thorough Milli-Q water rinse), and a further 15min oxygen plasma treatment. The TiO_2 thin films were then nucleated on the templates by immersion in equal volumes of 100mM $(NH_4)_2TiF_6$ and 200mM H_3BO_3 (Alfa Aesar) for 8h at 35ºC and then at 50 ºC for at least 10h. To burn off the polymer and to anneal the TiO_2, the films were sintered in a furnace under the following conditions: 300ºC for 6h and 450ºC

for 1h. The dip LbL procedure was repeated twice to achieve an appropriate pore size and thickness for the photoanodes.

To synthesize cobalt oxide virus-LbL films for Chapter 2, viruses were diluted in a water to have a concentration of 10^{10} viruses/mL and the pH was adjusted to 5.0 by adding 0.01 M HCl. Then, 1mL of the virus solution was dropped on LPEI/PAA film (2cm×4 cm). After incubation for 30min, the virus assembled film was rinsed with Milli-Q water and dried by blowing with nitrogen. The virus assembled LPEI/PAA film on PDMS pattern was incubated in 15mL aqueous solution of cobalt chloride (1mM) for 15min. Then 15mL $NaBH_4$ (5mM) was added to nucleate cobalt on the M13 virus templates. The incubation of virus templated cobalt in aqueous solution resulted in the spontaneous oxidation into cobalt oxide.

7.19. References

[1] Yoo, P. J., Nam, K. T., Qi, J., Lee, S. K., Park, J., Belcher, A. M., & Hammond, P. T. (2006). Spontaneous assembly of viruses on multilayered polymer surfaces. *Nature materials*, *5*(3), 234-240.

[2] Tan, W. M., Jelinek, R., Opella, S. J., Malik, P., Terry, T. D., & Perham, R. N. (1999). Effects of temperature and Y21M mutation on conformational heterogeneity of the major coat protein (pVIII) of filamentous bacteriophage fd.*Journal of molecular biology*, *286*(3), 787-796.

[3] Blanco, P., Kriegs, H., Lettinga, M. P., Holmqvist, P., & Wiegand, S. (2011). Thermal diffusion of a stiff rod-like mutant y21m fd-virus. *Biomacromolecules*,*12*(5), 1602-1609.

[4] Kay, B. K., Winter, J., & McCafferty, J. (Eds.). (1996). *Phage display of peptides and proteins: a laboratory manual*. Academic Press.

[5] Migneault, I., Dartiguenave, C., Bertrand, M. J., & Waldron, K. C. (2004). Glutaraldehyde: behavior in aqueous solution, reaction with proteins, and application to enzyme crosslinking. *BioTechniques*, *37*(5), 790-806.

[6] Mahrwald, R., & Evans, D. (2004). *Modern aldol reactions*. Weinheim: Wiley-VCH.

[7] Little, R. D., Masjedizadeh, M. R., Wallquist, O., & Mcloughlin, J. I. (2004). The intramolecular Michael reaction. *Organic Reactions*.

[8] Labconco Corporation. (2004). A Guide To Freeze Drying for the Laboratory. In *Labconco Industry Service Publication.*

[9] Day, J. G., & Pennington, M. W. (Eds.). (1995). *Cryopreservation and freeze-drying protocols*. Springer.

[10] Rasband, W.S., *ImageJ*, U. S. National Institutes of Health, Bethesda, Maryland, USA. (1997-2005).

[11] Williams, D. B., & Carter, C. B. (2009). *Transmission electron microscopy: a textbook for materials science*. Springer.